Phenomenology of Dark Matter from Radio to Gamma Ray Frequencies

Dissertation

zur Erlangung des Doktorgrades

an der Fakultät für Mathematik, Informatik und Naturwissenschaften

Fachbereich Physik

der Universität Hamburg

vorgelegt von

Martin Vollmann

Gutachter der Dissertation:	Prof. Dr. Torsten Bringmann
	Prof. Dr. Günter Sigl
Gutachter der Disputation:	Prof. Dr. Torsten Bringmann
	Prof. Dr. Günter Sigl
Datum der Disputation:	17. Juni 2015
Vorsitzender des Prüfungsausschusses:	Prof. Dr. Günter Wiedemann
Vorsitzender des Promotionsausschusses:	Prof. Dr. Jan Louis
Dekan der Fakultät für Mathematik, Informatik und Naturwissenschaften:	Prof. Dr. Heinrich Graener

Zusammenfassung

Astronomische Beobachtungen bei verschiedenen Wellenlängen haben sich als essentiell für das Verständnis der grundlegendsten Fragen der Physik erwiesen. Eines der größten Mysterien der Natur ist die Existenz der (bisher) unbestimmten Art der Materie welche den Großteil des materiellen Universums ausmacht. Auch wenn nur wenig über deren Natur bekannt ist, ist es sehr wahrscheinlich, dass es sich bei dieser exotischen *Dunklen Materie* (DM) um sogenannte Weakly Interacting Massive Particles (WIMPs) handelt.

In der vorliegenden Arbeit untersuchen wir, welche Strategien am besten dazu geeignet sind, die Frage *Was ist Dunkle Materie?* anzugehen. Konkret wählen wir das WIMP-Paradigma als unser Leitprinzip und diskutieren anschließend umfassend die Phänomenologie der aussichtsreichen Szenarien der indirekten Detektion solcher WIMPs. Insbesondere werden dabei die um das Zentrum der Milchstraße herum erzeugten außerirdischen Gammastrahlen und Radiowellen betrachtet.

Angesichts der zwei kürzlich vieldiskutierten Behauptungen einer WIMP-Entdeckung, nämlich der 130-GeV-Linie und des GeV-Exzesses der Gammastrahlung, benutzen wir unsere Methoden, um diese Hypothesen zu überprüfen. Außerdem enthält unsere Untersuchung Datenanalysen der Antiteilchen der Kosmischen Strahlung (Antiprotonen und Positronen). Die Phänomenologie der indirekten DM-Detektierung mithilfe dieser "Messenger" wird ebenfalls kurz diskutiert.

Durch die Ausnutzung des hohen Grades an Symmetrie bei typischen annihilierenden 2-WIMP-Anfangszuständen sind wir in der Lage, ein sehr mächtiges Instrument der theoretischen Teilchenphysik einzusetzen: Das verallgemeinerte optische Theorem. Dieses Theorem verknüpft die Amplitude von schleifenunterdrückten Prozessen, wie zum Beispiel der 130-GeV-Linie für den Fall, dass diese als Produkt von WIMP-Annihilationen interpretiert wird, mit deren Tree-Level-Prozessen, die auf dieselbe Weise eingeschränkt sind wie es beim GeV-Exzess der Fall ist. Neuartige analytische Verfahren zur allgemeinen Berechnung von Partialwellen-(und Helizitäts-)Wirkungsquerschnitten werden durchgeführt und anschließend entsprechend angewendet.

Ferner wird die Möglichkeit untersucht, dass ein nichttrivialer Effekt im Teilchenmodell der DM ein in Form einer Linie der Gammastrahlung auftretendes Signal verstärkt. Wir konzentrieren uns dabei auf das fünfdimensionale Modell mit "Universal Extra Dimensions" (UED), welches einen passenden Kandidaten für die DM liefert. Wir zeigen, dass die intrinsischen resonanten Eigenschaften des Modells zu Verstärkungen in den Streuquerschnitten der Annihilation führen. Alle notwendigen Kopplungen der die KK-Nummer verletzenden und in den Fixpunkten der Orbifaltigkeit lokalisierten Vertices werden ebenfalls erstmalig berechnet.

Motiviert durch die Möglichkeit einer Beschleunigung von DM-Teilchen auf beliebig große Energien durch Schwarze Löcher untersuchen wir die WIMP-Annihilation bei großen Schwerpunktenergien im UED-Kontext.

Abstract

Multiwavelength astronomical observations have been proven to be of crucial relevance in understanding the most fundamental questions in physics. One of the biggest mysteries of nature is the existence of a (still) unidentified type of matter that makes up most of the material universe. Although little is known about its nature, it is very likely that this exotic *Dark Matter* (DM) is made of so-called Weakly Interacting Massive Particles (WIMPs).

In this thesis we investigate which strategies can best address the fundamental question: *What is Dark Matter?* Specifically, by following the "WIMP" paradigm as our guiding principle, we comprehensively discuss the phenomenology of prospective "indirect" detection scenarios of such WIMPs. Special consideration is given to extraterrestrial gamma rays and radio waves produced around the center of the Milky Way.

In light of two recently highly debated claims of WIMP Dark Matter discovery, namely the 130 GeV *gamma-ray line* and the GeV *gamma-ray excess*, we invoke our methods to confront those hypotheses. In addition our study contains antiparticle cosmic-ray (antiproton and positron) data analyses. The phenomenology for indirect DM detection with these "messengers" is briefly discussed as well.

By exploiting the high degree of symmetry of typical annihilating 2-WIMP initial states, we are able to employ a very powerful tool in theoretical particle physics: the *generalized* optical theorem. This theorem relates the amplitude of loop-suppressed processes, such as the 130 GeV line if interpreted as product of WIMP annihilations, with tree-level process which are constrained in the same way as with the GeV excess. Unprecedentedly reported analytical computations of partial-wave (and helicity) cross sections with general applicability are calculated and applied.

The possibility that a non-trivial effect in the particle model for DM might enhance the strength of a gamma-ray line signal is also explored. We focus on the five-dimensional model with "Universal Extra Dimensions" (UED) which offers a suitable DM candidate. We show that the intrinsic resonant properties of the model give rise to enhancements in the annihilation cross sections. All the necessary couplings of KK-number violating vertices localized in the *orbifold* fixed points are also computed for the first time.

Motivated by the possibility that black holes can accelerate DM particles up to, in principle, arbitrarily large energies, we investigate WIMP annihilations with larger center-of-mass energies in the UED context.

Contents

List of Publications

[I] **Enhanced line signals from annihilating Kaluza-Klein Dark Matter.** C. Arina, T. Bringmann, J. Silk, M. Vollmann, Phys. Rev. D **90** (2014) 083506 [arXiv:1409.0007 [hep-ph]].

[II] **Updated cosmic-ray and radio constraints on light Dark Matter: Implications for the GeV gamma-ray excess at the Galactic center.** T. Bringmann, M. Vollmann and C. Weniger, Phys. Rev. D **90** (2014), 123001 [arXiv:1406.6027 [astro-ph.HE]].

[III] **130 GeV gamma-ray line and generic Dark Matter model building constraints from continuum gamma rays, radio, and antiproton data.** M. Asano, T. Bringmann, G. Sigl and M. Vollmann, Phys. Rev. D **87** (2013) 10, 103509 [arXiv:1211.6739 [hep-ph]].

List of Figures

List of Tables

Introduction

After CERN's recent discovery of a boson that seems to possess all the properties of the long-sought Higgs boson, all the pieces of the Standard Model of Particle Physics have fallen into place. One of the next frontiers in physics is understanding the nature of the dominant components of the Universe, namely *Dark Energy* and *Dark Matter*. While the former still lacks a fully satisfactory theoretical elucidation, very well motivated theories of the latter do exist. In this thesis we shall limit ourselves to exploring the mysteries associated with the Dark Matter component –henceforth referred to as DM– by making predictions of phenomenological relevance.

Our best handle on the physics of the early Universe, the *Cosmic Microwave Background* (CMB), provides us with compelling information that paves the way for hunting for DM. Measurements of the CMB anisotropies agree with the hypothesis that most of the (dark) matter in the Universe consists of **W***eakly* **I***nteracting* **M***assive* **P***articles* (WIMPs). Curiously, particles with exactly the same properties are anticipated by theories beyond the Standard Model of Particle Physics such as Supersymmetry (SUSY) or models with Universal Extra Dimensions (UED). This coincidence, commonly referred to as the *WIMP miracle*, makes the search for DM particularly interesting for the communities of cosmology, astroparticle and particle physics.

Complementary evidence in favour of the DM hypothesis is provided by modern observations of galaxies and galaxy-clusters. In fact, the gravitational pull of DM on the motion of such massive astrophysical objects was observed in the 1930's. Nevertheless, no definite positive signal of any DM interaction has yet been found at the microscopic level.

As we argue in this thesis, signatures of DM interactions other than gravity could potentially be probed by next-generation astronomical instruments. We will mainly focus on radio and gamma rays as eventual signals of *indirect detection* of DM are expected to peak in those frequency ranges. Relevant experiments include the *Low Frequency Array* (LOFAR) and the *Square Kilometre Array* (SKA) radio interferometers. The gamma ray satellite *Fermi Large Area Telescope* (FERMI-LAT) and the *Cherenkov Telescope Array* (CTA) are also expected to shed light on the nature of DM.

In the first part of this work, we provide a thorough review on the possible imprints in the gamma ray and radio skies of prospective WIMP DM annihilation. We also toch upon the signatures of DM in cosmic-ray antiparticle observations and two recent claims of DM discovery, namely the "130 GeV gamma-ray line" and the "Gamma-ray GeV excess".

The rest of the thesis is dedicated to my original contributions to the field which led to the three publications [I-III]. Specifically, we employ a generalized variant of the *optical theorem* to constrain the model building for the 130 GeV excess. In our comprehensive overview, we demonstrate that this theorem has a wide range of applicability in the context of DM phenomenology.

In addition, by using the methods for indirect DM detection reviewed here, we confront the DM interpretation of the GeV gamma-ray excess with radio and antiparticle cosmic-ray data.

In the last part we revisit one of the central assumptions in DM phenomenology: the approximation of vanishing relative speed of the two annihilating WIMPs. We argue that non-trivial effects such as resonances can play a dominant role once this approximation is relaxed. For clarity, we focus on the five-dimensional model with Universal Extra Dimensions (UED). Due to its mass-spectrum ladder structure such resonant effects arise quite naturally in annihilation processes.

We also briefly discuss the so-called Bañados-Silk-West effect. According to this effect, DM particles that are close to a Black Hole will be accelerated by the strong gravitational field. Depending on the angular momentum of the Black Hole, DM collisions could attain arbitrarily large center-of-mass energies.

This thesis is structured as follows: we begin with an overview of the theoretical foundations of the WIMP DM, where we pay particular attention to the UED models. In the second chapter, we introduce the relevant methodology used to search for DM and focus on the methods of indirect detection. Then we discuss the prompt emission of gamma rays from DM annihilation in chapter 3. In chapter 4 we comprehensively describe the synchrotron emission of electrons and positrons interacting with the Galactic magnetic field and focus on the DM signal.

In chapter 5, we discuss the optical theorem and then we report the 130 GeV line model building constraints that result from its application. We also discuss our limits on the GeV excess. The last chapter discusses the DM-induced gamma ray line enhancement that results from taking into account the effects of the velocity distribution of Kaluza-Klein DM. Finally, we state our conclusions and include four appendices where we derive some relevant formulas used in this thesis and our original results.

Chapter 1

Preliminaries

1.1 Observational evidence of Dark Matter

Although the most compelling piece of evidence that there is a dark matter component in the Universe is cosmological, the first indication of its existence dates back to the 1930's. In year 1932 (1933) astronomers [31, 32] noticed that the total amount of mass, as inferred from their observations of the Milky Way [31] (Coma Cluster [32]), did not correspond to the mass needed to explain how stars (galaxies) rotate around the Milky Way's (Coma Cluster's) halo.

Both authors attributed such discrepancies to some mysterious massive component which they coined Dark Matter. More modern measurement techniques [1, 33] of *rotation curves* as the ones performed in [31, 32] not only confirm the existence of Dark Matter, as apparent in the left panel of figure 1.1, but also have become observational probes of the DM. In such curves, the velocity (assuming circular orbits) of an observed emitter is reported as a function of its position respect to the center of the observed galaxy. Intriguingly, astronomers noticed that in contrast to their theoretical expectations rotation curves show a behaviour that can not be reconciled with the assumption that the motion of the emitters is explained by the gravitational pull of the *observed* matter. This anomaly is of course a manifestation that there might exist unidentified **dark** objects responsible for the "odd" features in the rotation curves.

At larger scales, the evidence is more robust as larger astrophysical objects such as galaxy clusters prove to be excellent probes of DM. In this case different measurement strategies provide complementary information about the dynamics of the DM. The most notorious example supporting the DM case in these scales is the Cluster 1E 0657-558, usually referred-to as the *Bullet Cluster*: the collision of two galaxy clusters –see figure right panel of fig. 1.1–. By combining information on the cluster's gravity field as inferred from gravitational lensing (bending of the light due to the cluster's enormous mass) and X-ray images of the same object, one actually observes that there should be invisible almost non-interacting DM components that during the collision decouple from the stronger interacting visible part that sits in the middle of the cluster.

In the next section we will briefly introduce the basic notions of Cosmology and discuss the evidence of DM in that context.

1.2 The Lambda CDM paradigm

The probably most solid evidence of the presence of a non-baryonic dark matter component in the Universe is cosmological, i. e. when observing the Universe at its largest

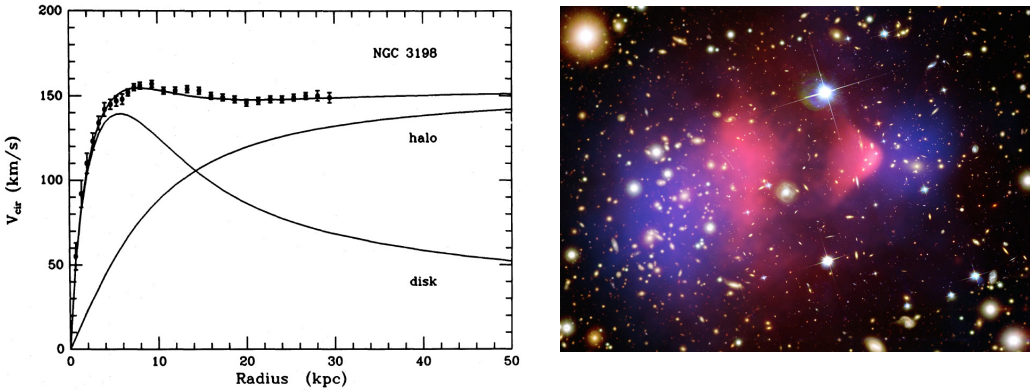

Figure 1.1: Left: rotation curve of NGC 3198 galaxy and the two-component (Dark Matter halo + exponential disk) mass model fit considered by the authors reference [1] from which the figure was extracted. Right: superimposed to the "Bullet cluster" 1E0657-56 optical image are in fake colors X-ray image from Chandra (pink) and the gravitational lensing map (blue) [2].

accesible scales ($\sim 10\,\mathrm{Gpc}$). Most of the physics at such scales is successfully described by the standard model of cosmology: the Λ cold dark matter (ΛCDM) model. In the following we will briefly introduce the most basic features of this theory focusing on the dark sector.

At its largest scales the Universe is rather simple as to a great extent it looks the same in every direction. Notice that at cosmological scales "small" discrete sources such as galaxies will only represent $\lesssim 10\%$ anisotropies of the full picture of the Universe, in pretty much the same way as the discreteness of water molecules in a glass of water are not resolvable by the naked eye. Technically speaking, the property that our view of the Universe does not depend on the direction at which we look is called *isotropy*.

This property together with the *homogeinity* assumption, i.e. our position in the Universe is not special and the Universe is isotropic in all possible reference points –Copernican principle– are the foundations of modern cosmological theories. The most compelling evidence of this is the existence of an almost (to a degree of accuracy of the order of 10^{-5}) perfectly isotropic *cosmic microwave background* (CMB) in nature. This radiation is the footprint of the so-called *recombination* epoch where –according to the ΛCDM model– bound states formed and all matter became predominantly neutral.

In a general relativistic setup, the Copernican principle makes it straightforward to construct a general theory for the Universe. In the General Relativity (GR) jargon we do this in terms of a two-parameter space-time metric: the *Robertson-Walker* (RW) metric

$$\mathrm{d}s^2 = \mathrm{d}t^2 - a^2(t)\left[\frac{\mathrm{d}r^2}{1-\kappa r^2} + r^2\,\mathrm{d}\Omega^2\right] , \tag{1.1}$$

where the scale factor $a(t)$ and the curvature parameter κ are the only quantities needed to describe the geometry of a perfectly isotropic and homogeneous Universe. Physically, the evolution of $a(t)$ respect to the time coordinate t determines whether the Universe is expanding or contracting. The sign of the second parameter κ defines the topological properties of the RW space: $\mathrm{sgn}(\kappa) = -1, 0, 1$ correspond to open (negative curvature), flat (no curvature) and closed (positive curvature) spatial slices of the RW space-time.

The dynamics of the cosmological parameters is given by Einstein GR equations $R_{ab} - \frac{1}{2}g_{ab}R = 8\pi G T_{ab}$. Assuming that the Universe is a perfect fluid: $T^a_{\ b} = \mathrm{diag}(\rho, -p, -p, -p)$, where ρ and p are the fluid's total energy density and pressure respectively, we can –after

some algebra– arrive to the so-called *Friedmann* equations

$$\left(\frac{\dot{a}}{a}\right)^2 = \frac{8\pi G}{3}\rho - \frac{\kappa}{a^2} \quad , \quad \frac{\ddot{a}}{a} = -\frac{4\pi G}{3}(\rho + 3p) \ , \tag{1.2}$$

that together with a *state equation* (typically $p = w\rho$) fully describe a Copernican Universe within the GR framework. Notice that ρ and p are regarded as dynamical variables in the Friedmann equations. With the exception of the case where $w = -1$ that we discuss below, the solutions of eqs. (1.2) are powers of the time coordinate $a(t) \propto t^{\alpha}$. In particular, when $a(t) = 0$ –e. g. at $t = 0$– the metric becomes singular, defining in this way a beginning of time or the *Big Bang*.

Usually when refering to the dynamics of the cosmological parameters people introduce the *Hubble parameter*

$$H \equiv \frac{\dot{a}}{a} \ ,$$

which essentially gives a measure of how quickly the Universe expands or contracts. The Hubble parameter evaluated at present time is the familiar *Hubble constant* $H_0 = 100h\text{kms}^{-1}\text{Mpc}^{-1}$, with $h = 0.673 \pm 0.012$ cf. [34, 35]. We then define the critical density

$$\rho_{\text{crit}} \equiv \frac{3H^2}{8\pi G} \ ,$$

so that the first Friedmann equation (1.2) can be rewritten as

$$1 - \Omega = -\frac{\kappa}{H^2 a^2} \equiv \Omega_{\text{curv}} \ ,$$

where we, in passing, defined the cosmological *density parameters* $\Omega = \rho/\rho_{\text{crit}}$ and $\Omega_{\text{curv}} = \rho_{\text{curv}}/\rho_{\text{crit}}$ with $\rho_{\text{curv}} = -3\kappa a^{-2}/8\pi G$ so that if $\rho = \rho_{\text{crit}}$ then $\Omega_{\text{curv}} = 0$ and the Universe is flat. Notice that ρ_{curv} is not a physical density but just a convenient mathematical artifact such that we can put the geometry and energy components of eq. (1.2) in the same footage. For future convenience we notice that ρ_{curv} is proportional to a^{-2}.

After some manipulations of eq. (1.2) and the equation of state $p = w\rho$ one can show that analogously $\rho \propto a^{-3(1+w)}$. If the Universe is mainly compossed by non-relativistic collisionless matter we can use the equation of state of an ideal gas $w \propto kT/m_p$ where m_p is the mass of the particles (kT is the thermal energy of the particles). Since these are nonrelativistic $kT \ll m_p$ and $w \simeq 0$ and $\rho_{\text{matter}} \propto a^{-3}$. If radiation is the leading component, then the energy-momentum tensor is given by an incoherent sum of **traceless** Maxwell stress tensors. The fact that it is traceless implies that $w = 1/3$ and $\rho_{\text{rad}} \propto a^{-4}$. In the next section we will discuss another interesting equation of state, namely the one that results from an energy-momentum tensor that is proportional to the metric.

1.2.1 Dark Sector

In our cosmological discussion above we did not make any assumption as to the physical energy density ρ. In principle, ρ could stand for the energy density of invisible matter or radiation or even something more exotic we shall call dark energy. In this section we will introduce the concept of dark energy and discuss the necesity of introducing a dark matter component in the cosmological model introduced above.

1.2.1.1 Dark Energy

As already disclosed before, apart from radiation and matter an exotic component such that its energy-momentum tensor is proportional to the metric is physical and actually existing in nature. This component is defined by the equation of state $p = -\rho$ ($w = -1$) such that $\rho_\Lambda \propto a^0$. In a flat space ($\kappa = 0$) such as ours (cf. [35]) the Hubble parameter is constant and the scale factor grows exponentially $a(t) \propto \mathrm{e}^{Ht}$.

To a big extent, the accelerated expansion defined by $a(t) \propto \mathrm{e}^{Ht}$ provides the correct description of the present-time Universe as recently confirmed by measurements of the CMB anisotropies by the PLANCK experiment [35]. This phenomenon was already noticed in 1998 by observations of distant Type Ia supernovae [36, 37] leading the authors to be awarded with the 2011 Nobel prize award.

The state-of-the-art measurement of the dark energy density parameter in a flat Universe is $\Omega_\Lambda = 0.686 \pm 0.020$ [35]. This means that ∼70% of the Universe's energy budget is composed by this exotic dark energy component.

A completely equivalent interpretation of dark energy can be done in terms of the geometrical concept of Λ: the *cosmological constant*. Had we introduced instead of the dark energy term $T_{ab} = 8\pi G \rho_\Lambda g_{ab}$ a cosmological-constant term Λg_{ab} in the GR equations, the physics would have remained the same despite the change in the nomenclature.

From a theoretical point of view, the cosmological constant problem poses one the strongest challenges in modern physics as no mechanism has been proposed that satisfactorily explains the origin of Λ from first principles. The biggest limitation comes from the fact that dimensional analysis arguments based on the hope that quantum gravity would provide a solution to this problem (Λ has units of [mass]^4 in natural units), fail by ∼100 orders of magnitude in estimating the actual magnitude of Λ [38].

1.2.1.2 Dark Matter

In the dark-energy-dominated Universe in which we live, only ∼30% of its energy content is composed by matter and radiation. However, by estimating the amount of energy in form of radiation that there is in the Universe by the photon density $\rho_{\mathrm{CMB}} = 0.25\,\mathrm{eV/cm^3}$ we find that[1] $\Omega_{\mathrm{rad}} \simeq 10^{-4}$. Therefore, the missing 30% of the total energy density that is not associated to the dark energy introduced above, is composed by massive objects.

The amount of baryonic matter can however be estimated by several methods. The most powerful are through the constraints that result from analyzing the power spectrum of the CMB anisotropies. However, a probably more instructive, if less accurate, method is by measuring the abundance of nuclei synthetized a few seconds after the Big Bang in a cosmological era called the *Big Bang Nucleosynthesis* and noticing that the baryon-per-photon ratio has to be of the order of 5×10^{-10} [38] for the analysis to be consistent. This puts the baryonic density parameter to be as low as $\Omega_{\mathrm{bar}} = .05$, result that is consistent with the latest results of the PLANCK mission. Consequently there is five times as much *non-baryonic dark matter* as regular matter.

It is customary to report the amount of matter in the Universe in terms of its corresponding density parameter times the dimensionless Hubble constant squared (as $\rho_{\mathrm{crit}} \propto H^2$). The most precise measurements of the DM and baryon density in the Universe are respectively (cf. [34, 35]) $\Omega_{\mathrm{b}} h^2 = 0.022\,07 \pm 0.000\,33$ and $\Omega_{\mathrm{DM}} h^2 = 0.1196 \pm$

[1] Other radiation degrees or freedom are neutrino and further possible dark radiation species. CMB analyses are however able to constrain their associated density parameters.

0.0031. In the next section we shall expand our discussion on the cosmological dark matter.

1.2.2 The WIMP Miracle

Shortly after the Big Bang the Universe was supposed to by a very dense "soup of relativistic particles" in thermal equilibrium. Inasmuch as the interaction rates of the particles $n(t)\langle\sigma v\rangle$ remained larger than the expansion rate $\sim H(t)$, such an equilibrium existed ($n(t)$ is the particle-number density at time t, σ is the interaction cross section and v is the relative speed). However, as the Universe cooled down, expansion started to dominate and the processes DM DM$\rightarrow$ X Y (X and Y represent particles different than a theorized self-interacting DM particle) happened more frequently than the typically kinematically forbidden reverse process X Y$\rightarrow$DM DM. As a consequence, the DM particles decouple from the cosmic thermal bath and most of their dynamics is progressively given by the expansion and their possible decay. After this freeze-out mechanism, the abundance of such DM particles left in the present time could therefore explain why most of the matter in the Universe is dark in a rather refined way.

Quantitatively, this phenomenon is described by a Boltzmann equation which, after including the effects of expansion and assuming that the annihilation products follow thermal distributions inmediately after they are produced, reads [39]

$$\frac{\mathrm{d}n_{\mathrm{DM}}}{\mathrm{d}t} + 3Hn_{\mathrm{DM}} = \langle\sigma v_{\mathrm{M\o ll}}\rangle(n_{\mathrm{DM}}^2 - n_{\mathrm{DM}}^{\mathrm{eq.}\,2}) \ , \tag{1.3}$$

where the Møller velocity is defined in such a way that the cross section σ transforms as a scalar rather than as an area[2] and is defined as

$$v_{\mathrm{M\o ll}} = \frac{\sqrt{(p_1\cdot p_2)^2 - m_\chi^4}}{E_1E_2} = [\|\boldsymbol{v}_1 - \boldsymbol{v}_2\|^2 - \|\boldsymbol{v}_1\times\boldsymbol{v}_2\|^2]^{1/2} \ , \tag{1.4}$$

while

$$n_{\mathrm{DM}}^{\mathrm{eq.}} = \int \frac{\mathrm{d}^3p}{(2\pi)^3}\frac{g_{\mathrm{DM}}}{\mathrm{e}^{E/kT}\pm 1} \tag{1.5}$$

is the DM particle number density at equilibium, where g_{DM} is the number of degrees of freedom of the DM particle and the sign in the denominator is determined by the particle spin (- for bosons and + for fermions).

Equation (1.3) can easily be solved numerically if we assume that such *chemical decoupling* occurs in the radiation dominated epoch (when $H(t) = 1/2t \simeq \sqrt{g_{\mathrm{eff}}}T^2/M_{\mathrm{Planck}}$). For DM masses in the range of $10 - 1000\,\mathrm{GeV}$, the (relic) DM density parameter that results from evaluating the solution of eq. (1.3) after decoupling is [39]

$$\Omega_{\mathrm{DM}}h^2 \simeq 0.11\left(\frac{2.8\times10^{-26}\,\mathrm{cm}^3/2}{\langle\sigma v\rangle}\right) \ . \tag{1.6}$$

Rather interestingly, in the present time DM particles have speeds of the order of $\sim 10^{-3}$ times the speed of light. If the particle interaction amongst the DM particles is weak, i. e. $\sigma \sim \alpha_{\mathrm{em}}/\sin^2\theta_W/(100\,\mathrm{GeV})^2 \simeq 1\,\mathrm{pb}$, then $\sigma v \sim 3\times10^{-26}\,\mathrm{cm}^3/\mathrm{s}$ which

[2]Several particle physics textbooks –including Peskin and Scrhoeder's [40]– introduce the concept of cross section in terms of the relative velocity $v_{\mathrm{rel.}} = \|\boldsymbol{v}_1 - \boldsymbol{v}_2\|$ rather than the Møller velocity (1.4). In practice, cross section calculations are carried out either in the center-of-mass frame or in the lab frame and since $\boldsymbol{v}_1\times\boldsymbol{v}_2 = 0$ then $v_{\mathrm{rel.}} = v_{\mathrm{M\o ll}}$ in both frames.

is just the needed interaction strength needed for the DM to be thermally produced shortly after the Big Bang. This coincidence is sometimes quoted as the WIMP miracle, where WIMP stands for *Weakly Interacting Massive Particle*.

As a final comment on the WIMP paradigm, we notice that if we had assumed that the DM was composed by neutrinos –as they are non-baryonic weakly-interacting massive particles–, the sum of their masses would need to be significantly larger $\mathcal{O}(100\,\mathrm{eV})$ than present estimates from neutrino oscillation observations. Moreover, at freeze-out they would be still relativistic rendering them as **hot** DM. As we shall briefly discuss in chapter 3, cosmological N-body simulations strongly favor the hypothesis that DM was **cold** (non-relativistic) at freeze-out. Otherwise, present-time structures (clusters of galaxies, galaxies and so on) would not have been able to form.

This line of argumentation completes our gross introduction to the standard model of Cosmology: the Λ CDM model. We will discuss now these ideas are connected to claimed solutions of utterly uncorrelated problems in particle physics, making the WIMP paradigm the leading guiding principle for the DM searches that are investigated in this thesis.

1.3 Particle Physics Models

The standard model (SM) of particle physics has enormous success in describing the interactions of fundamental particles up to subnuclear scales $\sim 0.001\,\mathrm{fm}$. Its latest successful test was the discovery of a scalar boson that, to a high confidence level, bears the properties (couplings, decay channels, etc.) of the Higgs boson as predicted by the theory.

Nevertheless, the SM is by construction incomplete as it does not include gravity and has unnatural radiative behaviour. The latter limitation is usually referred-to as the *hierarchy problem*. Several solutions to this problem have been put forward, being the introduction of a new symmetry that relates fermionic degrees of freedom with bosonic ones called Supersymmetry (SUSY) the leading one.

Supersymmetric extensions of the SM not only solve the hierarchy problem in a rather elegant way but they also unify the electro-weak and strong interactions at some higher energy scale if SUSY is broken at the TeV scale. The price to pay is the introduction of at least the same amount of new particles as the already existing in the SM and uncertainties associated to our ignorance about how SUSY is broken. We do not aim to discuss the features of this theory in detail, but we will rather content ourselves with mentioning that some SUSY extensions of the SM, in particular the *Minimal Supersymmetric Standard Model* (MSSM) provide, almost accidentally, a suitable DM candidate: the SUSY *neutralino* χ^0

$$\chi^0 \equiv \tilde{\chi}_1^0 = N_{11}\tilde{B} + N_{12}\tilde{W}^3 + N_{13}\tilde{H}_1^0 + N_{14}\tilde{H}_2^0 \ , \tag{1.7}$$

which is a neutral Majorana fermion with couplings to SM particles that are related to the ones of the Z and H bosons. Interestingly, the reason why minimal SUSY extensions of the SM provide a DM candidate is motivated by pure particle physics reasons. Some soft SUSY breaking (trilinear) terms induce simultaneous lepton and baryon number violation that can be avoided by the introduction of the so-called R-parity symmetry. This symmetry then stabilizes the lightest supersymmetric particle (LSP) which we require to be neutral –otherwise we would have detected it– and thus provide us with a strong candidate that would reveal the nature of the DM and, at the same time, solve profound particle physics problems in an elegant way.

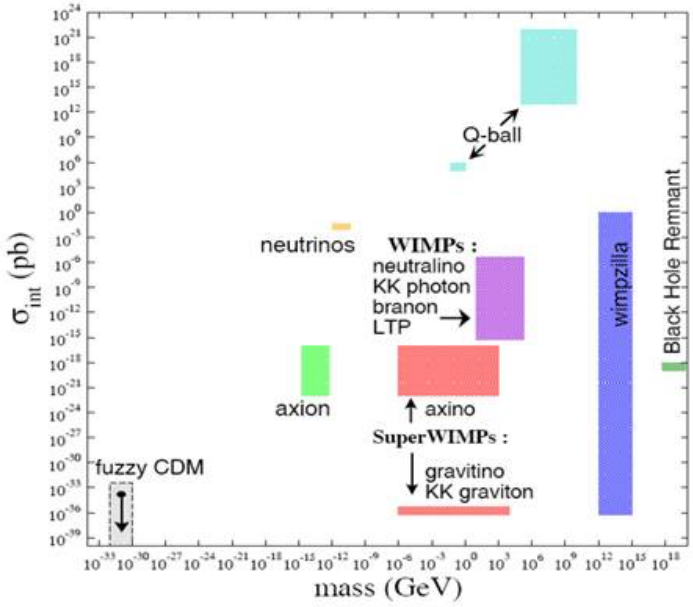

Figure 1.2: Typical mass and interaction cross section of several DM candidates [3]

In the cosmological setup introduced before, for a large "hyper volume" of the MSSM free-parameter space, the thermal average of the total annihilation rate of the neutralinos $\langle \sigma v_{\text{Møll}} \rangle$ is such that the DM density at present time is explained through the freeze-out mechanism discussed before. Furthermore, a phenomenologically interesting scenario can arise in some parameter regions where some of the assumptions leading to eq. (1.6) fail and DM co-annihilations (annihilation of a neutralino and all other supersymmetric particles) become important. In section 5.2 we will come across this co-annihilation region in a completely different context.

Several other models with WIMP candidates have been constructed under the principles of minimality: "Minimal DM", "The Inert Doublet Model", "Higgs Portal", while some others such as the MSSM are inspired by elementary particle physics. In the next section we will discuss in detail an example of the latter type of models, namely the effective theory that results from adding one extra dimension to the space-time where the particles propagate.

Although the WIMP scenario is rather appealing, there are several other concrete models that introduce different possible manifestations of the DM at microscopic scales. Figure 1.2 roughly displays the typical particle masses and interaction cross sections of several theories for DM.

1.3.1 Universal Extra Dimensions

Another interesting particle-physics-motivated DM candidate is the so-called Lightest Kaluza-Klein Particle (LKP) in models with Universal Extradimensions (UED). These models are constructed from non-renormalizable extra dimensional realizations of the Standard Model as the four-dimensional (4D) effective field theories that result from the *compactification* of such extra dimensions. In this thesis, specifically in chapter 6, we extensively considered one such models and thus, we shall dedicate this section to introduce these models in a fairly detailed way.

Although many of the conclusions at which we will arrive in this section apply

to theories with several extra dimensions, we will only consider one compact extra dimension x^5. In the circular (S^1) compactification the coordinate x^5 can be chosen in such a way that physics is invariant under the transformation $x^5 \to x^5 + 2\pi R$, where R is the compactification radius, while the rest of the coordinates describe the standard 4D space-time. In terms of field theory, the addition of an extra dimension has interesting kinematical consequences that are also easy to derive.

Let us consider an arbitrary scalar 5D field $F(x; x^5)$ describing a free particle of mass M. By decomposing the field in terms of its **discrete** Fourier modes in the extra dimension

$$F(x; x^5) \sim \sum_{p^5 = n/R} F_n(x)\, \mathrm{e}^{i p_5 x^5} \ ,$$

we effectivelly introduce and infinite set of 4D scalar fields $\{F_n(x)\}$ satisfying the 4D Klein-Gordon equation of particles with masses $M_n = \sqrt{M^2 + (n/R)^2}$:

$$\left(-\partial^2 + \left(\frac{n}{R}\right)^2 + M^2 \right) F_n(x) = 0 \ .$$

The towers of particles associated to the existence of extra dimensions are usually called *Kaluza-Klein mass towers* after Theodor Kaluza and Oskar Klein who first proposed the existence of extra dimensions in the context of general relativity [41, 42].

From the phenomenological point of view, this is a good start since the tower of infinite new degrees of freedom associated to the extra dimension are effectively heavier than the particles described by the zeroth-mode field $F_0(x)$. Notice that $F_0(x)$ is the field that results from ignoring the existence of extra dimensions. From Heiseberg's uncertainty principle considering $F_0(x)$ instead of its 5D "parent" F is approximately correct as long as $\Delta x \gg R$, or equivalently $\Delta E \ll R^{-1}$, where Δx and ΔE are the typical length and energy uncertainties of the particle described by F. We see that R^{-1} naturally (owing to Heisenberg's uncertainty principle) defines a critical energy scale above which the effects of the compactified extra dimension can be observed.

Under these premises, it seems clear that promoting the SM fields to 5 dimensions and modifying the SM Lagrangian accordingly will effectively result in a 4D theory embedding the familiar SM and an, in principle, infinite number of states that are only attainable at energies larger than R^{-1}. Most of the aforementioned will actually be true as we shall see soon. However, a simple dimensional analysis of the couplings that one would have to introduce in a 5D SM-like theory shows that such a theory is non-renormalizable and we should follow an effective-field-theory approach. We shall introduce a cut-off energy scale Λ above which unknown physics takes over. As a consequence only a limited subset of the tower of states associated to the compatified extra dimension will be regarded as physical.

Our introductory discussion has so far only been concerned with scalar fields. Nevertheless, the SM features also spinor and vector fields with chiral couplings, spontaneous symmetry breaking, etc. that need to be incorporated in the 5D model. The fact that 5 is an odd number represents a limitation in including chirality in the theory as such concept does not exist in odd-dimensional space-times (all spatial reflections are equivalent to some continuous rotation). The most direct way of getting around this is by reexamining the compactification scheme and introducing *ad hoc* some geometrical property that is connected to the concept of chirality in the lower-dimensional space-time. For example, by imposing certain mirror-symmetry conditions $x^5 \to -x^5$ automatically relating any two opposite points in a circle –e. g. $x^5 = 0$ and $x^5 = \pi R$– in the so-called *orbifold compactification.*

In this scheme out of all possible scalar fields F we "fold" the fifth dimension by decomposing the fields in terms of their parity: $F_\pm(x^5) = \pm F_\pm(-x^5)$ and we will call them even (+) or odd (-) depending on the sign of such identification. Notice that odd scalar fields have no zeroth-mode component. Since the fifth component of a vector field transforms as a scalar in the reduced 4D geometry, such a property will be crucial in consistently constructing a model with one extra dimension and no extra unobserved scalar degrees of freedom associated to the SM gauge bosons. All 5D vector gauge field in this theory will be such a way that $A_5(x, x^5)$ is odd owing to the gauge symmetry. Their orbifold identification will thus be the following $A_\mu(x, x^5), A_5(x, x^5) \to A_\mu(x, -x^5), -A_5(x, -x^5)$.

The parity of the orbifold spinors are defined according to the identification $\Psi(x, x^5) = \pm\gamma^5\Psi(x, -x^5)$. Notice that for spinors, both even and odd fields have non-vanishing zeroth-mode components and moreover, in the 4D realization those the zeroth-mode component of an even (odd) field will be left-handed (right-handed).

By promoting the SM fields to 5D fields in the orbifold with the identification rules just discussed we can retrieve the usual 4D SM Lagrangian plus additional degrees of freedom and interaction terms associated to the extra dimension. Without going into the details of such decomposition (we instead refer to Ref. [43]), we only comment of the resulting effective field theory.

SM bosons	g^a_μ, A_μ, Z_μ, $W^\pm_\mu$	H, G_Z, $G^\pm_W$	
KK$^{(n)}$ bosons	$g^{a\,(n)}_\mu$, $B^{(n)}_\mu$, $A^{(n)}_{3\,\mu}$, $W^{\pm\,(n)}$	$H^{(n)}$, $a^{(n)}_0$, $a^{(n)}_\pm$	$B^{(n)}_5$, $A^{(n)}_{3\,5}$, $W^{\pm\,(n)}_5$

SM fermions	e_R, (e_L, ν_e)	$(u, d)_R$, $(u, d)_L$
KK$^{(n)}$ fermions	$e^{(n)}_s$, $e^{(n)}_d$, $\nu^{(n)}_e$	$u^{(n)}_s$, $d^{(n)}_s$, $u^{(n)}_d$, $d^{(n)}_d$

Table 1.1: Particle spectrum of the model with one universal extra dimension. Dot-underlined fields are non physical Goldstone bosons and we omitted ghost fields. For clarity, we neglected the mass mixing associated to electro-weak symmetry breaking.

First, by performing a correct counting of the degrees of freedom we observe that in contrast to SUSY for every right-handed **and** left-handed fermion in the SM there will be a corresponding Kaluza-Klein (KK) tower of massive **Dirac** spinors. Since KK particles do not acquire their masses through spontaneous gauge symmetry breaking but through the compactification, KK excitations of those Higgs-doublet degrees of freedom that are non-physical in the SM will become physical. On the other hand, the missing longitudinal degrees of freedom for the (massive) KK excitations of vector gauge fields will be provided by their corresponding (Goldstone bosons) fifth component excitation[3].

Table 1.1 provides a summary of the particle content of the model. Notice that all KK excitations share the electro-weak group transformation properties of their corresponding zeroth-level partners. For instance, e_s is an SU(2) singlet and therfore has hypercharge -1. Finally, the dimensionfull gauge and Yukawa couplings in the 5D theory are related to the usual dimensionless couplings of the SM by the identification $g = g_5/\sqrt{2\pi R}$.

[3]Strictly speaking, KK excitations of both Higgs-doublet scalars and the fifth components of electro-weak gauge fields are linear combinations of three physical degrees of freedom and three Goldstone bosons per KK mode.

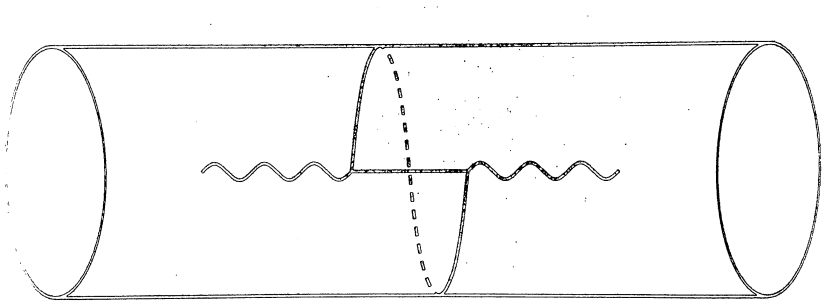

Figure 1.3: Lorentz violating 5D loop diagram [4].

1.3.1.1 Lightest Kaluza-Klein Particle

The UED theory as introduced before bears, by construction, the same symmetries as the SM. In particular, the Poincaré symmetry which is the product of translation and Lorentz invariance is an exact symmetry of the resulting 4D theory. However, such a symmetry in the 5D setup is broken by the compactification: the fact that the fourth spatial dimension is different than the other three breaks Lorentz invariance and the existence of two fixed points $x^5 = 0, \pi R$ in the orbifold compactification breaks translation symmetry. Since the conserved quantity associated to translations are the corresponding momentum components –in particular, $p^5 = n/R$ for translations in the x^5 coordinate–, breaking of such a symmetry results in violation of momentum conservation. Therefore, the KK-number is not conserved in this model.

Poincaré symmetry breaking and consequently KK-number violation occurs only globally. Locally, the compactness of the fifth dimensions is not apparent. In quantum-field theoretical terms this means that KK-number violation will become apparent at the *loop* level. However, a smaller discrete symmetry remains unbroken: *KK-parity*. This is basically the flipping invariance of the extra dimension. As a consequence, the lightest first-mode KK particle (LKP) is stable and, if the usual conditions are met, a suitable candidate for DM.

Understanding the mass spectrum of the KK mass tower is essential in determining which of the mode-1 KK particles is the LKP. We briefly mentioned before that the mass of the n-th KK excitation of a scalar particle has a mass $M_n = \sqrt{M_S^2 + (n/R)^2}$, where M_S is the mass of the zeroth-mode particle. By a similar argument the reader can convince himself that also for vector excitations the same formula applies, while for spinor fields $M_n^f = M_f + n/R$. If the compactification scale is orders of magnitude greater than the mass of the mode-0 particles, then the masses of all nth-mode KK particles lie around the same value $M_n \simeq n/R$. If we want to determine which one out of all the mode-1 KK particles is the lightest, radiative corrections are crucial.

Since the mechanism generating the masses of the KK particles is rather unconventional, we need to identify what kind of radiative phenomenon will be responsible for the quantum corrections of the KK particles masses. Although at the beginning it might seem rather formal and difficult to compute, radiative corrections affecting the mass of the KK particles exclusively stem from radiative terms with explicit Poincaré-symmetry violation.

Both orbifold and S^1 compactifications violate Lorentz symmetry, as (in a global or topological sense) the compact extradimension is different than the other ones. Vacuum polarization diagrams where the loop winds (see fig. 1.3) around the compact dimension will thus be the diagrams of interest. Ref. [4] showed that these diagrams are finite and computed them explicitely by summing over the winding number rather than over p^5.

The second and, at least for large n, main contributors of radiative mass corrections are translation violating terms that are localized in the orbifold fixed points. Vacuum polarization diagrams also contain KK-number-violating diagrams that give rise to kinetic and mass mixing terms. Also Ref. [4] comprehensively studied these and in the concrete case of UED they were able to obtain the full KK tower spectrum of physical masses by assuming *minimality*. Where the minimality is imposed by requiring that the radiative terms at the orbifold fixed points vanish at the cutoff scale where physics beyond the UED model takes over.

Figure 1.4 portrays the mass spectrum of mode-1 KK particles if minimality is assumed. Albeit using the exact formulae and methodology discussed in Ref. [4], we used a different value for the cut-off scale $\Lambda R = 5$ [44]. Larger values are not allowed as they would jeopardize the stability of the electroweak vacuum [45] (see also [46–49]).

We see in fig. 1.4 that the LKP is the first excitation of the U(1) gauge field B_μ (denoted as $B^{(1)}$). This is of course a suitable DM matter candidate since is neutral, massive, weakly interacting and moreover it could have been thermally produced in the early Universe if the compactification energy scale R^{-1} 1.2 TeV in combination with $\Lambda R = 5$ [50].

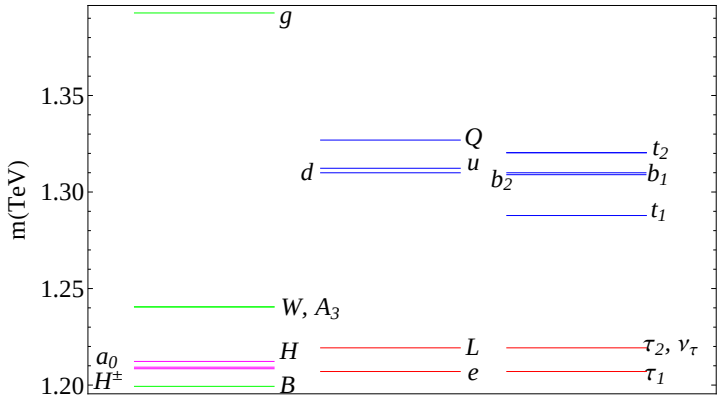

Figure 1.4: Mass spectrum of the first mode particles in the minimal UED for a compactification mass and cutoff scales $R^{-1} = 1.2\,\text{TeV}$ and $\Lambda = 5.6\,\text{TeV}$ respectively.

Chapter 2

Strategies to search for Dark Matter

In the previous chapter we discussed how an appealing theoretical mechanism can explain the observed abundance of DM in the Universe while at the same time providing solutions to intrinsic problems in elementary particle physics.

In the remaining of this thesis we will follow this *WIMP paradigm* as our guiding principle in searching for the DM. The hunt for WIMP DM can be divided into three categories depending on the process in which the WIMP participates. These are *collider production*, *direct* and *indirect searches for DM*. All these strategies are equally important as they complement each other. In this thesis we will focus on the latter while in the following we mention the basic idea behind the former strategies.

2.1 Colliders

WIMP DM has the defining property that it can be probed at the $\sim$ GeV $-$ TeV scale, which is precisely the energy scale of the CERN's Large Hadron Collider (LHC) [51] currently operating in the Swiss-French border near Geneva. Although there is up to date no claimed evidence of any signal at the LHC that can be attributed to DM, there is hope that in the next few years the LHC can shed some light on the nature of DM.

In the LHC high energy proton-proton collisions are investigated by, predominantly, two big experiments: ATLAS [52] and CMS [53]. Early 2012 both collaborations announced the discovery [54, 55] of a boson that, according to their measurements, has the properties of the Higgs boson of the Standard Model. After a two-year shutdown the LHC made its restart quite recently. It will now be able to reach its maximum centre-of-mass energy capabilities: 14 TeV.

In particle colliders such as the LHC, WIMP DM is expected to be produced quite rarely in collisions. This limitation can be overcome if the collider has a large luminosity which is the case of the LHC. The luminosity is, roughly speaking, a quantity that indicates the number of collisions per unit time.

Once a WIMP pair is produced in, for instance, a proton-proton collision at the LHC, they escape from detection. The key variable to identify events where these particles might have been produced is the so-called missing transverse energy. Depending on the particle physics model, other strategies are typically used to constrain the parameter space of the model.

A model-independent approach can be implemented by means of effective field theory

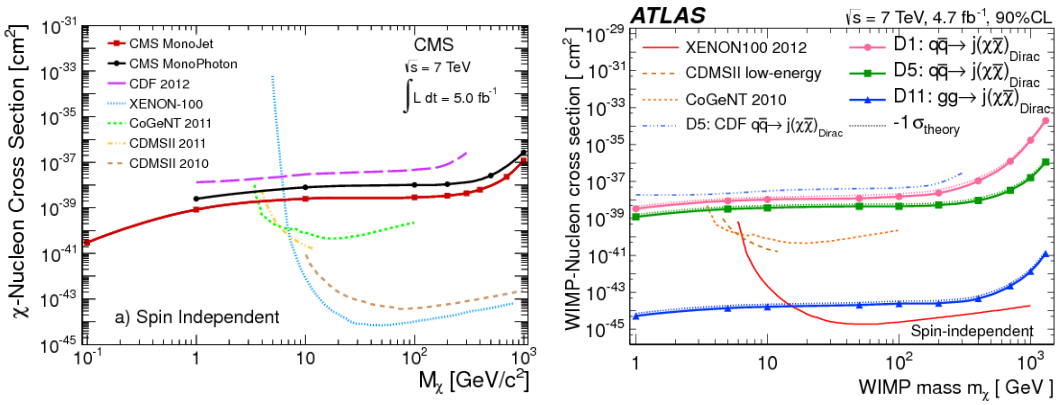

Figure 2.1: Inferred limits on the (spin-independent) WIMP-nucleon cross section from collider data. Left: CMS [5]. Right: ATLAS [6].

–for a review the reader can refer to [56] or to the earlier work [57]–. The resulting limits on the production cross section of WIMPS that are inferred from such analyses are then translated, by *crossing symmetry*, into limits on nucleon-WIMP scattering cross sections so that they can be compared to corresponding limits from experiments of direct DM detection. Figure 2.1 shows how the CMS constraints on the nucleon-WIMP cross sections [5, 6] compare to the constraints on the same process as obtained by direct detection experiments.

2.2 Direct detection

As we show below, in the solar neighbourhood we expect that there are seizeable amounts of DM. Therefore, interaction of ambient DM particles with experimentally monitored atomic nuclei could lead to detectable signals. This possibility of directly detecting DM has given rise to the birth of several dedicated experiments such as XENON100 (XENON1T) [58, 59], LUX [60], DAMA/LIBRA [61], etc. where nuclear recoils caused by an eventual scattering of a DM particle off a nucleus are measured through the scintillation light that is emitted in the process. Cryogenic detectors such as CDMS II [62], CRESST [63], EDELWEISS [64] on the other hand measure the recoils by detecting the heat that is produced when a nucleon-DM scattering takes place.

Figure 2.2 displays the limits on the scattering cross sections from different direct detection experiments. The DAMA/LIBRA collaboration and its predecessor DAMA/NaI reported an annual modulation which they interpreted as caused by DM [61]. Depending on the WIMP model, the preferred parameter regions associated to this interpretation are the bubbles in fig. 2.2. Similarly the CRESST collaboration interpreted in Ref. [65] a number of anomalous events as originated by DM. These claims are however in strong tension with other experiments.

2.2.1 Local DM density

Direct DM detection is highly dependent on the amount of DM in the Solar System: the higher the density of DM at Earth the higher the probability of detecting it. Since this quantity will be of great interest also for the indirect detection strategy that is discussed below, let us say a few words about the current situation.

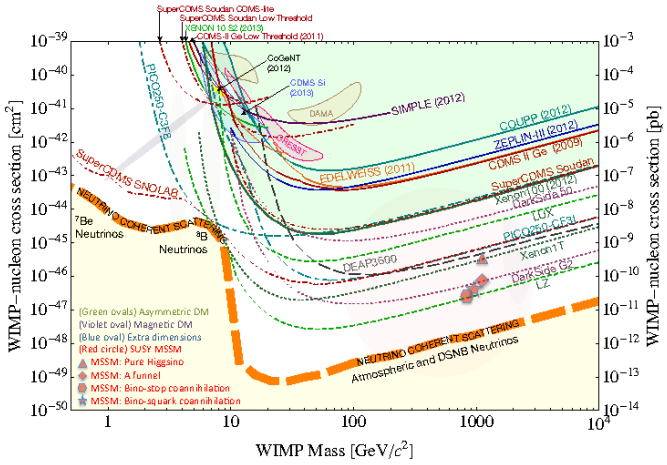

Figure 2.2: Limits from several direct DM detection experiments on the spin-independent WIMP-nucleon cross section and the sensitivity limit where atmospheric neutrino background fluxes are resolvable [7].

The local DM density can be measured "locally" by studying the vertical motion of stars near the Sun [66] or "globally" by fitting mass models for the Milky Way with rotation curve observations [67]. The usually accepted value is $\rho_\odot = 0.4\,\mathrm{GeV/cm^3}$, which corresponds to ∼1 - 40 DM particles in one litre.

The second method has the advantage that the uncertainties in $\rho_\odot$ are smaller at the price of making global assumptions about our DM halo (e. g. sphericity, etc.). We will however assume a spherical halo and adopt a local density $\rho_\odot = 0.4\,\mathrm{GeV/cm^3}$ consistently.

2.3 Indirect detection

Another strategy to look for DM is through the byproducts of its interactions in those astrophysical environments where it is very likely that processes such as DM annihilation or decay occur. In this thesis we focus on these indirect DM detection methods. In particular, we will comprehensively discuss prospective signals associated to DM in the electromagnetic spectrum but also mention and make use of indirect detection methods through cosmic rays.

The general method that is applied when indirectly hunting for DM consist of confronting theoretical estimates of the DM signal of interest as it arrives to Earth. The theoretical modelling is done by making educated guesses on the unknown DM distribution as well as its microscopic properties. More specifically, for each detection channel (gamma rays, cosmic-ray antiparticles, radio, etc.) we will introduce source functions of the type

$$q_{\mathrm{ann.}}(\boldsymbol{r}, E_m) = \frac{1}{2}\left(\frac{\rho_\chi(\boldsymbol{r})}{m_\chi}\right)^2 \langle\sigma v\rangle \sum_c \mathrm{BR}_c \left(\frac{\mathrm{d}N}{\mathrm{d}E_m}\right)_c \tag{2.1}$$

$$q_{\mathrm{decay}}(\boldsymbol{r}, E_m) = \frac{\rho_\chi(\boldsymbol{r})}{m_\chi}\Gamma_\chi \sum_c \mathrm{BR}_c \left(\frac{\mathrm{d}N}{\mathrm{d}E_m}\right)_c , \tag{2.2}$$

where $\rho_\chi(\boldsymbol{r})$ represents the DM mass distribution, $\langle\sigma v\rangle$, Γ_χ and m_χ are respectively the velocity-averaged *annihilation rate*, decay width and mass of the DM particle. The terms summed over are the branching ratios and differential yields of the particles relevant for detection.

N-body simulations will prove to be useful when modelling the DM distribution and some analytical ansätze for ρ are available. It is thus customary to scan over the different ansätze when modelling the DM signal so as to estimate the associated uncertainties. Analogously, we get around the uncertainties from the particle physics side by assuming BR=1 for several benchmark cases. The particle yields are obtained by software packages such as DarkSUSY [68].

After making the aforementioned assumptions on the sources, we plug the associated source functions (2.1-2.2) in the appropriate propagation model. Depending on the channel of interest, additional uncertainties, e. g. the magnitude of magnetic fields, diffusion coefficients, etc. are to be expected. In the following we briefly discuss the particularities of several indirect detection channels of DM.

2.3.1 The electromagnetic sky

Although WIMP DM is incapable to emit radiation by its own, there exist mechanisms where electromagnetic radiation that is associated to DM can be emitted. Due to the hypothesized properties of these WIMPs (mass range, etc.) they are indeed unable to produce measurable optical light. WIMP DM is almost completely black in the optical range.

However, there are other frequency ranges in the electromagnetic spectrum where the DM can be observed once quantum effects (DM annihilation) are taken into account. A quick inspection to equation (2.1) allows us to realize that for the typical WIMP DM mass ranges, photons that are produced by WIMP annihilation have energies comparable to the DM mass ($\sim$ 10 - 1000 GeV). These are gamma-ray energies.

Similarly, we notice that most of the photons from DM annihilation will be produced at those sites where the DM densities are the highest. In particular, the center of our own Galaxy is the greatest source of radiation associated to DM to which we have access. In figure 2.3 we see the observable spectrum of radiation coming from the Galactic Center (GC). We notice that the intermediate frequencies (from microwaves until ultraviolet frequencies) are inaccessible because of the interstellar dust clouds. They are invisible in the low and high frequencies.

Fortunately, gamma rays produced at the GC travel unperturbed all the way from their sources down to Earth. They are one of the most promising observational channels in the field of indirect DM detection. We will see in the next chapter that the spectral properties of a typical DM-induced gamma ray signal can be such that they can not be mimicked by any known astrophysical process, rendering them "smoking gun" indicators of DM.

On the opposite end of the spectrum, radio measurements can also be used to search for DM. Electrons and positrons produced by DM annihilation (or decay) will emit synchrotron radiation while they are deflected by the Galactic magnetic field. In chapter 4 we comprehensively discuss the DM radio signal and the methods and assumptions that enter in the associated theoretical predictions.

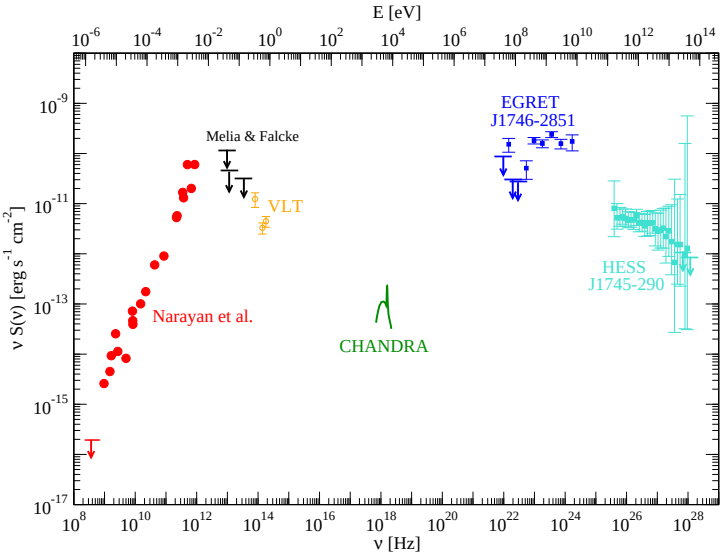

Figure 2.3: Observed electromagnetic spectrum of Sgr A* (Galactic center) [8]

2.3.2 Cosmic-ray antiparticles

Cosmic-ray measurements can also hint us about the existence of wimps. Since DM annihilation or decay produces as much particles as antiparticles, we better search for DM signals associated to the latter so that the signal-to-background (S/B) ratio is optimized. In particular, antiprotons and positrons are the only stable charged particles that might be promtly produced by DM and we shall focus on their corresponding signal. In contrast to neutral particles, antiprotons and positrons are stochastically deflected in their journey down to Earth and it is unfortunately impossible to point back to their sources.

2.3.2.1 Antiprotons

As predicted by almost every model, DM will annihilate or decay with a large branching ration into hadronic channels. After the final state of the annihilation/decay undergoes a hadronization process, created particles can start to propagate. Among these particles there are stable high-energetic antiprotons that after interacting with the interstellar medium arrive to Earth and are detected.

In order to describe the DM-induced antiproton signal and compare it to measurements, powerful methods have been devised [30, 69] which are based on statistical fits of cosmic-ray datasets to well motivated propagation models.

In the most general setting, the propagation of antiprotons in the Galaxy is described by a transport equation

$$\frac{\partial n_E^{\bar{p}}}{\partial t} - D(E)\nabla^2 n_E^{\bar{p}} - \frac{\partial}{\partial z}(V_c n_E^{\bar{p}}) - \frac{\partial}{\partial E}\left(D_E(E)\frac{\partial n_E^{\bar{p}}}{\partial E} - b(E) n_E^{\bar{p}}\right) = Q^{\bar{p}}(\boldsymbol{r}; E) \ , \quad (2.3)$$

where n_E is the antiproton number density per unit energy; D, D_E, V_c and $b(E)$ are propagation variables and Q is a source function containing a contribution associated to DM. In subsequent chapters we will use and scrutinize a similar equation in the context of synchrotron signals of DM. In this section, we shall simply make a shallow

discussion on the parameters entering the equation and refer to the most interesting results reported in the literature.

The parameters $D(E)$ and $D_E(E)$ in eq. (2.3) are the spatial and energy-space diffusion coefficients while V_c and $b(E)$ are respectively the speed of an convective wind and the antiproton energy-loss rate. The magnitude of all parameters in this model will be assumed to be constant within the antiproton propagation volume. The term proportional to $D_E(E)$ in eq. (2.3) is commonly quoted as the *reacceleration* or Fermi acceleration term. In a number of astrophysical setups the energy-space diffusion coefficient is not independent of the spatial one and the formula

$$D_E(E) = \frac{2}{9} V_a^2 \frac{p^4}{D(E) E^2}$$

is applicable [69]. V_a is the drift (Alfvén) velocity of the turbulent magnetic field (see [70] for a concrete definition) and p is the antiproton momentum. We will regard V_a as a constant parameter of the theory while we adopt the "pitch angle scattering" parametrization of the diffusion coefficient $D(E) = D_0 \beta (p/\mathrm{GeV})^\delta$.

As mentioned before, the source function contains a *signal* term related to the annihilation of DM in the halo and a *background* term associated to antiproton production via cosmic-ray nuclei –typically H and He– *spallation* off the interstellar medium. The signal term (2.1) is spherically symmetric respect to the center of the galaxy and subdominant respect to the background terms such as for instance

$$Q_{\mathrm{Helium}} = 4\pi \int \mathrm{d}E' \left(\frac{\mathrm{d}\sigma}{\mathrm{d}E}\right)_{He'^{+}+H_{ISM}\to\bar{p}+\ldots} n_{H_{\mathrm{ISM}}}(\boldsymbol{r}) \Phi_{He^+}(\boldsymbol{r}; E') \ , \tag{2.4}$$

where Φ_{He^+} is the flux of cosmic-ray Helium nuclei per unit energy at a point $\boldsymbol{r}$. In addition to these terms, an additional term of terciary antiprotons accounting for the annihilation of antiprotons on interstellar protons or the excitation of Δ resonances (inelastic scattering off interstellar protons) should also be included.

$$Q_{\mathrm{ter.}} = \int \mathrm{d}E' \left(\frac{\mathrm{d}\sigma}{\mathrm{d}E}\right)_{\bar{p}(E')+p_{ISM}\to\bar{p}(E)+\ldots} n_{H_{\mathrm{ISM}}}(\boldsymbol{r}) v'_{\bar{p}} n^{\bar{p}}_{E'}(\boldsymbol{r}) - \sigma_{\bar{p}(E')+p_{ISM}\to\bar{p}(E)+\ldots} n_{H_{\mathrm{ISM}}}(\boldsymbol{r}) v_{\bar{p}} n^{\bar{p}}_{E}(\boldsymbol{r}) \ . \tag{2.5}$$

By assuming that the interstellar gas is constrained to a *thin* disc of height $2h = 200\,\mathrm{pc}$, neglecting energy losses and imposing cylindrical boundary conditions $n^{\bar{p}}_E|_{\mathrm{edge}} = 0$ at the edge of a cylinder of radius $R_D = 20\,\mathrm{kpc}$ and variable height L, the authors of Ref. [69] were able to obtain analytical solutions for eq. (2.3) with no DM component. These solutions are parametrized by five parameters D_0, δ, V_a, V_c and L.

Notice that since the aforementioned parameters also describe other cosmic-ray observations, they are constrained and cannot be treated as completely free parameters. Although measurements of cosmic-ray fluxes of, for instance, heavier nuclei could potentially be useful in constraining the propagation parameters, a more powerful method considered in Ref. [71] will provide the tightest constraints on them. Namely, the ratio of secondary boron nuclei to their progenitor primary carbon nuclei.

In Ref. [71] the authors fitted their semi-analytical solutions of transport equations similar to (2.3) to the rather accurate boron-to-carbon (B/C) data available in year 2001. In their analysis they found excellent agreement between their model and the data in a parameter space that is mildly degenerate. Specifically, in the range $2 \lesssim L \lesssim 6$, variations of both L and D_0 are not independent. In this regime, it is more appropriate

to regard only the *diffusion time scale* L/D_0 as a true free parameter [72] Therefore, any attempt to fit the antiproton spectrum measured at Earth by means of the diffusion model defined by eq. (2.3) should be consistent with the B/C analysis. In chapter 5 we will discuss some of these aspects in more detail and find some improved fits to the PAMELA [23, 73] antiproton spectrum based on sophisticated statistical methods.

Another aspect that turns out to be extremely relevant for low-energy antiprotons is the so-called *solar modulation*, i. e. the influence of the solar wind on the propagation of the antiprotons. Before briefly discussing positrons in the context of indirect DM searches in the next section, let us mention that the physics of solar modulation can thoroughly be described by numerical methods that solve Boltzmann equations in spherical coordinates respect to the Sun's position [74]. The way solar modulation is implemented when making predictions of antiproton fluxes arriving to Earth consists of (*i*) obtaining the flux

$$\Phi_{\rm LIS}(\boldsymbol{r}; E) = \frac{1}{4\pi} n^{\bar{p}}_E(\boldsymbol{r}) v_{\bar{p}} \ ,$$

that arrives at the boundaries of the heliosphere –or, as usually called, the local interstellar (LIS) environment– by solving eq. (2.3); (*ii*) use such flux as a boundary condition to solve the equation describing the particle's propagation within the heliosphere and obtaining the flux at the Earth's *top of the atmosphere* (TOA).

Interestingly, the effect of solar modulation on antiprotons can be shown to be equivalent to a pure heliocentric electric field description [75, 76] in certain limits also discussed in those references. Fortunately, for the antiproton energy ranges we will be concerned in this thesis, the force-field approximation will be applicable. Under this *force-field* approximation, the fluxes at the top of the atmosphere and the local interstellar environment are related by a simple rule of three

$$\Phi_{\rm TOA}(E_{\rm TOA}) = \frac{p^2_{\rm TOA}}{p^2_{\rm LIS}} \Phi_{\rm LIS}(E_{\rm LIS}), \tag{2.6}$$

where $E_{\rm TOA} = E_{\rm LIS} + e\phi_F$ for antiprotons and ϕ_F is an electric (Fisk) potential associated to such effective heliocentric electric field. Its magnitude oscillates in resonance with the $\sim$11 years solar cycle.

By including a DM component, the degeneracy of the B/C analysis is broken and the results depend on L and D_0 independently [30]. In other words, there exist several choices of the propagation parameters that are consistent with the B/C but which impact on the antiproton analysis with a DM injection can lead to rather different outcomes. This propagation uncertainties can of course be quantified by pinpointing which set of propagation parameters correspond to the two extreme cases where (1) the antiproton flux is minimized ("MIN" model) and where (2) the same flux is maximized ("MAX" model). In chapter 5.4 we specify the set of parameters that result from the "MIN - MAX" model and we use them to put constraints on the annihilation cross section of DM.

2.3.2.2 The positron fraction

Cosmic ray positron signals have received lots of attention recently in light of the experimental evidence of a rise in the *positron fraction*: the ratio of the positron flux to the total flux of electrons and positrons "$e^+/(e^+ + e^-)$". Already hinted by the HEAT, AMS-01 and PAMELA experiments, it was recently confirmed with high precision by the AMS-02 mission [9] (see figure 2.4).

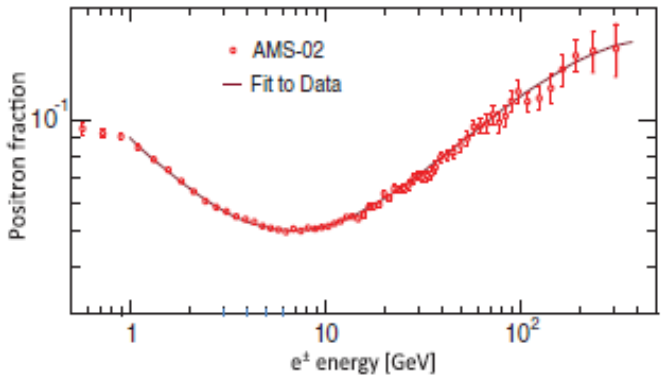

Figure 2.4: AMS-02 measurements of the positron to electron and positron flux ratio as reported in Ref. [9].

Although it is tempting to attribute the existence of the excess to a DM-related process (e. g. annihilation or decay in the halo), an astrophysical explanation is more likely to clarify the origin of the excess. Without going into much details, the main reason why it is difficult reconcile the excess with a DM process is, as we shall demonstrate in chapter 4, that positrons are not able to travel large ($\gtrsim$ kpc) distances without losing most of their energy. Since the center of the galaxy, which is the main source of DM-induced positrons, is much too far from the Solar System ($\sim 8.5\,$kpc), a DM interpretation of the strong positron fraction rise must also explain why the flux is so large.

Several theories ranging from local sources (pulsars), supernovae dynamics down to propagation effects have been put forward. Without having any take on the possible explanations of the excess, the AMS-02 collaboration came up with a set parametrization templates for both the electron and positron fluxes they measured. These are phenomenologically constructed as the sum of a source term –power-law with an exponential cutoff– that is identical for electrons and positrons and independent power-law distributions. As apparent in fig. 2.4 they manage to fit their measurements remarkably.

$$\Phi_{e^\pm} = C_\pm E_{e^\pm}^{-\alpha^\pm} + C_S E_{e^\pm}^{-\beta}\, \mathrm{e}^{-E_{e^\pm}/E_\mathrm{c}} \quad . \tag{2.7}$$

The study of the DM positron signal works pretty much as in the case of antiprotons. We consider propagation models for the positrons and solve an equation similar to (2.3) where owing to the positron's lower mass, the convection term as well as the inelastic scattering sink term (positron annihilation with the ISM) can be neglected albeit consideration of the otherwise neglected energy loss term. In chapter 4 we will thoroughly discuss the leading mechanisms responsible for the positron's losses of energy, namely synchrotron radiation, inverse Compton scattering, bremsstrahlung and for lower energies Coulomb interactions. As far as this section is concerned, we will content ourselves by mentioning that the propagation of positrons in our galaxy is dominated by such energy-loss mechanisms.

Regarding the source terms participating in the positron's propagation equation, we can either (*i*) pick a particular model (pulsars, SN, etc.) explaining the positron rise and inject the DM through an adequate function (2.1); or (*ii*) use the parametrization (2.7) (with all the parameters kept as variable) as a background flux to which we add the DM-only signal. Refs. [10, 77] obtained the up-to-date most stringent constraints

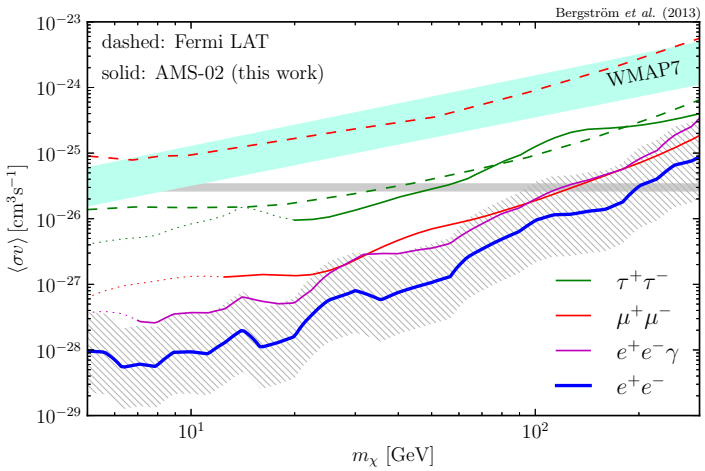

Figure 2.5: Positron limits on the annihilation cross section of DM as deducted in Ref. [10] from the AMS-02 2014 measurements [9].

on $m_\chi \lesssim 300\,\text{GeV}$ DM annihilation into leptonic channels (figure 2.5). Notice that in analogy to the antiproton analysis, the positron flux that one obtains by solving the usual transport equation also needs to be multiplied by a solar modulation correction factor that fortunately can also be approximated by the force-field prescription introduced in the previous section. In section 5 we shall revisit these concepts in the context of model-building constraints for the claimed indication of a DM-like signal in gamma rays.

Chapter 3

Gamma rays

Gamma-ray observations as the ones carried out by the *Large Area Telescope* on the Fermi Gamma Ray Space Telescope spacecraft (FERMI-LAT) [11] are of particular interest when searching for DM. This kind of radiation is expected to be promptly emitted as byproducts of WIMP DM annihilation or decay. In contrast to other channels, they do not suffer from complicated interactions with magnetic fields in their paths, providing therefore accurate spatial information about their sources.

3.1 The Gamma-ray sky as seen by FERMI

The relatively newborn field of high energy astrophysics is as fascinating as complex. Extreme phenomena can be accessed and theoretical models can be tested with experimental probes such as the *Fermi* telescope. This space-borne experiment is characterized by a large field-of-view ($\sim$ 20% of the sky), a large energy span (30 MeV - 1 TeV) and large collection period.

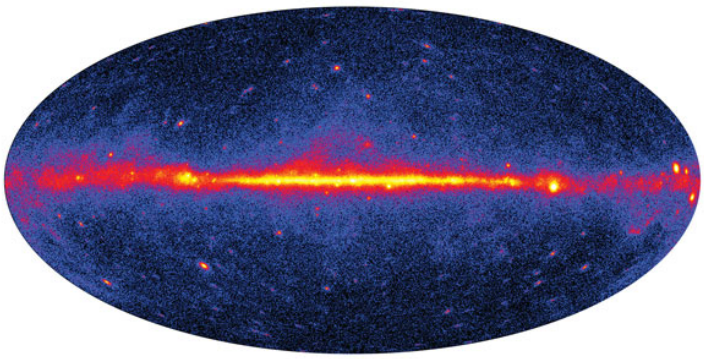

Figure 3.1: NASA/DOE/Fermi LAT collaboration [11]. Gamma-ray full-sky map.

Figure 3.1 shows the Fermi sky map of one year (2009) of observations of gamma rays with energies larger than 300 MeV [11]. According to the present understanding, the gamma-ray sky portrayed in fig. 3.1 is composed by three major components.

1. **Resolved sources:** these are mostly extragalactic *Active Galactic Nuclei* (AGNs) which are extreme galaxies hosting supermassive black holes (with masses 10^5 - $10^9 M_\odot$) in their rather luminous cores. They release tremendous amounts of energy

and matter in form of jets that extend up to several hundred kiloparsecs (being the nucleus just the size of a few parsec). Depending on their alignment respect to us, they are also named *radio galaxies* (edge-on), *Seyfert galaxies* (almost edge-on), *quasars* (jet is almost head-on) and *blazars* (head-on jet).

We will however be more interested in the less abundant Galactic resolved sources. The most energetic ones are mainly *supernova remnants* and *pulsars* (short for pulsating rotating star). The former are the residual materials of either the core collapse or the thermonuclear explosion of a dying star, while the latter are highly magnetized rotating neutron stars. Other sources are globular clusters, pulsar wind nebulae and high-mass X-ray binaries.

2. **Isotropic gamma ray background:** unresolved extragalactic sources of high energy radiation such as the ones mentioned in the previous entry will effectively add to an, on average, isotropic background. However other exotic components such as intergalactic shocks in galaxy cluster mergers can also contribute.

   In DM-dominated environments, gamma rays from DM annihilation are also expected to contribute to this background. Although such analyses are beyond the scope of this thesis, we refer the reader to recent studies on such interesting DM signatures.

3. **Galactic diffuse emission:** besides the Galactic sources that can be resolved by *Fermi*, a diffuse component covers most of the gamma-ray sky. The dominant emission mechanisms are:

   (a) **Inverse Compton scattering:** high energy comic-ray electrons may scatter ambient low frequency radiation fields. A rather cumbersome kinematical analysis of this process shows that if $E = \gamma m_e c^2$ is the initial energy of the electron, the frequency of the scattered photon can be boosted by up to a γ^2 factor. For instance, electrons of a few GeV ($\gamma = 10^4$) can scatter off a background light photon $\sim$ eV which energy after the interaction can reach that of a gamma ray ($\sim$ GeV).

   (b) **Bremsstrahlung:** analogously, diffuse cosmic ray electrons propagating in the interstellar gas will emit braking radiation (customarily called bremsstrahlung for historical reasons) as a reaction to their encounters with heavier nuclei. The physical description of this type of radiation is closely related to the Compton scattering just discussed and it is explored in more detail in the next chapter.

   (c) **π^0 decay:** nuclear collisions between cosmic ray nuclei and the ISM will produce showers of secondary particles including neutral pi mesons π^0. Pions are however unstable and their main decay channel is $\pi^0 \to \gamma\gamma$. In the rest frame of the pion, each decay photon has an energy of 70 MeV. However, they are boosted by the pion's momentum.

Apart from the aforementioned components, an extended structure of two giant lobes perpendicular to the Galactic plane and with a height of about 8 kpc each (not distinguishable in fig. 3.1), was recently discovered in the Fermi data [78]. Although its counterparts had been already seen in X rays [79] and more recently in microwave frequencies by WMAP [80], there is no clear explanation of the origin of these *Fermi Bubbles*. In the remainder of this chapter we will discuss the morphology and spectral

properties of a prospective new diffuse component in the gamma-ray sky, namely the DM component.

3.2 Gamma rays from DM

In contrast to all other messengers that are relevant to indirect DM detection, the physical description of the propagation of gamma rays is straightforward. Namely, we just need to line of sight integration of the gamma ray emissivity function, which at a given point $\boldsymbol{r}$ is given –as a function of the photon's energy– by[1]

$$\Gamma(\boldsymbol{r}, E_\gamma) = \frac{1}{2}\left(\frac{\rho_\chi(\boldsymbol{r})}{m_\chi}\right)^2 \langle\sigma v\rangle \sum_c \mathrm{BR}_c \left(\frac{\mathrm{d}N}{\mathrm{d}E_\gamma}\right)_c \,.$$

The associated brightness is therefore given by the line of sight integral of the emissivity $j = \frac{1}{4\pi}\Gamma(\boldsymbol{r}, E_\gamma)E_\gamma$. Nevertheless, gamma-ray detectors usually report their measurements in units of [number of photons] $\times$ time^{-1} $\times$ area^{-1} $\times$ [solid angle]$^{-1}$ $\times$ energy^{-1} in order not to propagate the systematic uncertainties of E_γ also measured in real time. Similarly, instead of directly measuring the photon flux Φ_γ per unit energy, which according to our analysis reads

$$\frac{\mathrm{d}\Phi}{\mathrm{d}E_\gamma}(E_\gamma, \psi) = \frac{1}{4\pi}\frac{\langle\sigma v\rangle}{2m_{\mathrm{DM}}^2}\sum_c \mathrm{BR}_c \left(\frac{\mathrm{d}N}{\mathrm{d}E_\gamma}\right)_c \int_{\Delta\Omega}\mathrm{d}\Omega \int_{\mathrm{l.o.s}} \mathrm{d}l(\psi)\rho^2(\boldsymbol{r}) \tag{3.1}$$

for DM-induced photons, gamma-ray data is usually reported in terms of the differential flux $\mathrm{d}^2\Phi_\gamma/\,\mathrm{d}E_\gamma\,\mathrm{d}\Omega$:

$$\frac{\mathrm{d}^2\Phi}{\mathrm{d}E_\gamma\,\mathrm{d}\Omega}(E_\gamma, \psi) = \frac{1}{4\pi}\frac{\langle\sigma v\rangle}{2m_{\mathrm{DM}}^2}\sum_c \mathrm{BR}_c \left(\frac{\mathrm{d}N}{\mathrm{d}E_\gamma}\right)_c \int_{\mathrm{l.o.s}} \mathrm{d}l(\psi)\rho^2(\boldsymbol{r})\,, \tag{3.2}$$

since the angular resolution of such detectors is energy dependent.

Formula (3.2) will be central in our study of DM-induced gamma rays. Notice that provided that none of the effects discussed in the introductory sections of chapter 6, the gamma-ray flux (3.2) formula can conveniently be divided into two parts. The first one is called the astrophysical J-factor

$$J(\psi) = \frac{1}{4\pi}\int_{\mathrm{l.o.s}} \mathrm{d}l(\psi)\rho^2(\boldsymbol{r})\,,$$

that completely describes the spatial structure of the DM signal. This factor is then multiplied by a prefactor that only depends on the microscopic properties of the DM

$$K(E_\gamma) = \frac{\langle\sigma v\rangle}{2m_{\mathrm{DM}}^2}\sum_c \mathrm{BR}_c \left(\frac{\mathrm{d}N}{\mathrm{d}E_\gamma}\right)_c$$

that provides the signal's full spectral information.

[1] An extra 1/2 factor is necessary if the DM particle is not its own antiparticle.

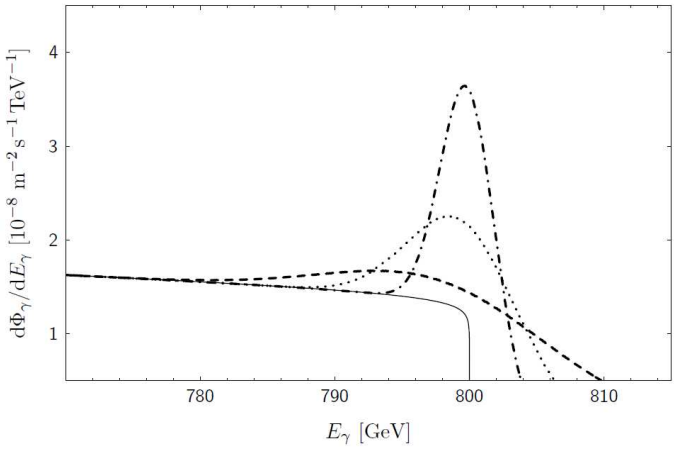

Figure 3.2: Typical spectrum of DM-induced gamma rays [12] featuring a continuum (secondaries) and a spectral line (primary). The line's width is determined by the energy resolution of the gamma-ray telescope.

3.3 Spectrum

Let us start by characterizing the spectral features of the DM signal in gamma rays. We do this by focusing on the particle physics prefactor $K(E_\gamma)$. When performing indirect searches for DM it is customary to assume that the annihilation proceeds with a branching ratio BR $\simeq 1$ into some specific channel. Particularly popular is the $\bar{b}b$ channel. The associated coupling constants participating in the computation of the $\chi\chi \to \bar{b}b$ amplitude are relatively large and, in several well-motivated models for DM, they make this channel the dominant one. In such a scenario gamma rays are produced as *secondary* particles from the fragmentation of the $\bar{b}b$ final state resulting in a rather featureless spectrum.

If gamma-ray photons are generated primarily via a two body or three body final state, then interesting spectral properties aries. The former case will manifest itself as a monochromatic gamma-ray line whereas the latter could show bump-like features that are of course interesting for gamma-ray searches. Figure 3.2 shows a typical (Kaluza-Klein DM) gamma-ray spectrum from DM annihilation in the halo [43] summarizing all these aspects. In the next few sections we will discuss them in detail.

3.3.1 Gamma-ray lines

One of the most striking signatures indicating the existence of DM through indirect searches for it, are the so-called gamma-ray lines. These would manifest themselves as byproducts of DM annihilations into two-body states that bear at least one photon if they should exist in nature. Kinematics arguments assure that such a photon is monochromatic. This is the reason why such signals are known as (gamma-ray) *line* signals in the spectroscopy language. The probably most important property of these signals is that there is no known astrophysical mechanisms capable of producing similar ones. They are therefore "smoking gun" signatures for indirect DM searches.

The energy of such signals depends on the mass of the second final-state particle. Namely, if m_X is the mass of the accompanying particle (X is typically a Z, H boson

or another gamma-ray photon) 4-momentum conservation requires that

$$\frac{\mathrm{d}N_{\mathrm{line}}}{\mathrm{d}E_\gamma} = \delta(E_\gamma - E_{\mathrm{mono}}) \ , \ E_{\mathrm{mono}} = m_\chi \left(1 - \frac{m_X^2}{4m_\chi^2}\right) \ . \tag{3.3}$$

There are two limiting factors that play an important role in searching for this kind of signals, though. The first one is more fundamental as it is related to the neutrality of the DM particle. Since DM particles do not directly couple to photons because they are electrically neutral, processes giving rise to line signals are "loop" suppressed. The second limitation comes from the detection performance of the experimental instruments measuring gamma rays. In theory, the width of a gamma-ray line is infinitely narrow –eq. (3.3)– but in practice, it is actually finite and depends on, for instance, the velocity dispersion of the DM particles (see section 6.4.1 for a thorough discussion). Nevertheless, the energy resolution of operating detectors at experiments such as FERMI-LAT and HESS is not able to resolve such small widths and (if the product $\langle\sigma v\rangle\,\mathrm{BR}_{\ \gamma X}$ is large enough) they would instead measure a bump centered at $E_\gamma = m_\chi(1 - m_X^2/4m_\chi^2)$ and a characteristic width ΔE determined by the detector's energy resolution. In section 3.5 we will come across an example where certain gamma-ray dataset can be fitted in such a way that one can accommodate a line signal to it with a fairly high confidence level.

3.3.2 Secondaries

The resulting spectrum of processes like $\chi\chi \to \bar{b}b$ can be obtained numerically through software packages such as DarkSUSY[68] or MicrOmegas[81]. The details of such numerical calculations are beyond the scope of this thesis but the reader might refer to the documentation files and the aforementioned references for an overview on the methods and calculational routines applied there.

Fortunately, the gamma-ray spectrum that results from DM annihilations into $\bar{b}b$ is approximately universal as it resembles the corresponding spectra for annihilations into other two-body channels (fermion and gauge boson pairs) where photons are only produced as secondaries. Moreover, such spectrum can conveniently be parametrizing through the formula [26]

$$\frac{\mathrm{d}N_{\mathrm{sec.}}}{\mathrm{d}E_\gamma} = \frac{0.42}{m_\chi} \frac{\mathrm{e}^{-8x}}{x^{3/2} + 1.4 \times 10^{-4}} \ . \tag{3.4}$$

The only exception are annihilations into $\tau^+\tau^-$ where the spectrum shows departures from that formula and a numerical approach is therefore unavoidable.

3.3.2.1 Internal bremsstrahlung

The appealing possibility of finding DM through a "smoking-gun signature" is certainly exciting. However, the loop suppression of the cross sections associated to these signals represents a major limitation in searching for them. Therefore, it will be interesting to extend our searching strategies by investigating "alternative" processes giving rise to unique spectral features. One such example are photons from *internal bremsstrahlung* (IB) on otherwise helicity-suppressed processes.

Motivated by SUSY models, consider an initial s-wave state of Majorana wimps. As we discuss in section 5.2.1, such an initial state will have vanishing total angular momentum and conservation of the same quantity will forbid a final state of **massless** Dirac fermions. If the fermions are massive, the process is allowed and by simple dimensional

analysis we expect that the corresponding cross section is proportional to $\sim m_f^2/m_\chi^2$, where m_f is the mass of the Dirac fermion. If this mass is orders of magnitude smaller than the DM particle mass, then the m_f^2/m_χ^2 factor will cause a suppression in the cross section. This phenomenon is usually called helicity suppression and in sec. 5.2.1 we shall provide a more technical explanation for it.

Interestingly, such suppression can be "lifted" radiatively, i. e. the branching ratio of the radiative process $\chi\chi \to \bar{f}f\gamma$ can become larger than the helicity suppressed $\chi\chi \to \bar{f}f$. Notice that since the IB process is defined by a three-body final state, an additional (suppressing) factor of $\sim \alpha_{\rm em}$ will replace the typically smaller m_f^2/m_χ^2 factor. In supersymmetric models IB processes can receive further enhancements if the neutralino mass is close to degenerate with charged sleptons (in particular staus in the so-called co-annihilation region). An analytical formula is even available [13] in the limit of massless fermions

$$\frac{\mathrm{d}N_{\rm IB}}{\mathrm{d}x} = \alpha_{\rm em} Q_f^2 \frac{|\tilde{g}_R|^2 + |\tilde{g}_L|^2}{64\pi^2} [m_\chi^2 (\sigma v)_{\chi\chi\to\bar{f}f}]^{-1} (1-x) \times \\ \times \left[\frac{4x}{\mu(\mu-2x)} - \frac{2x}{(\mu-x)^2} + \frac{\mu(\mu-2x)}{(\mu-x)^3} \log\frac{\mu}{\mu-2x} \right] , \tag{3.5}$$

where $x = E_\gamma/m_\chi$ and $\mathrm{d}N_{\rm IB}/\,\mathrm{d}x = (\sigma v)^{-1}_{\chi\chi\to\bar{f}f} (\mathrm{d}\sigma v/\,\mathrm{d}x)_{\chi\chi\to\bar{f}f\gamma}$ is e. g. defined in [13] as the *photon multiplicity*. The mass of the sfermions $\tilde{f}_R$ and $\tilde{f}_L$ was assumed to be the same, $\mu \equiv m_{\tilde{f}_R}^2/m_\chi^2 + 1$ and $\tilde{g}_R(\tilde{g}_L)$ are the couplings between the right (left) handed SM fermion f with the neutralino and the corresponding sfermion.

The Feynman diagrams responsible for the helicity-suppression lifting are those where the outgoing gamma ray couples to a virtual particle (diagrams of the type (c) in figure 3.3). Those photons are usually called *virtual internal bremsstrahlung* (VIB) photons while in those cases where diagrams of the type (a) and (b) are the dominant, we will speak of *final-state radiation* (FSR). The term internal bremsstrahlung includes of course both.

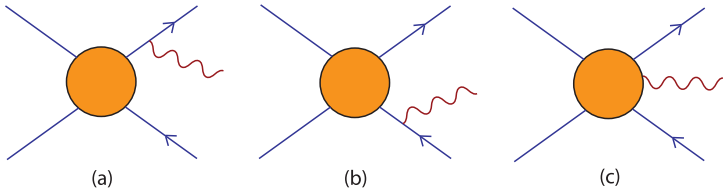

Figure 3.3: Feynman diagrams contributing to the first order QED corrections of the helicity suppressed annihilation of WIMPs into a pair of charged fermions [13].

More generally, IB processes can be sizeable even if the "parent" process does not suffer from helicity suppression. In those cases, FSR photons usually dominate the emission spectrum associated to IB, specially at photon energies close to the DM mass. This is attributed to collinearity of the radiated photon and either outgoing fermion, when the fermion masses are vanishingly small. From fig. 3.3 it is not too surprising that one can relate the cross section of the FSR process with the parent process $\chi\chi \to \bar{f}f$ in a universal model-independent way. Namely, formula 3.6 can be used for any model where the leading component of IB is FSR [82]:

$$\frac{\mathrm{d}N_{\rm FSR}}{\mathrm{d}x} \simeq \frac{\alpha_{\rm em} Q_f^2}{\pi} \frac{1+(1-x)^2}{x} \log\left[\frac{4m_\chi^2(1-x)}{m_f^2} \right] . \tag{3.6}$$

In particular, the UED model is an example where the FSR is not only the leading component of the IB but from most of the continuum spectrum [83].

3.4 Spatial morphology

Numerical simulations such as Via Lactea II (VL2) [84] and Aquarius [85] provide quantitative insights about the DM mass distribution in galaxies like ours. In this section we will discuss some basic ideas on what we have learned from N-body simulations about the structure and sub-structures of DM in our Universe. These are essential ingredients in understanding not only the spatial configuration of the DM-associated gamma-ray signal but also of all possible indirect DM signals and in particular the ones relevant to radio astronomy which will be the subject of the next chapter. After introducing all those ideas, we will proceed to characterize the spatial properties of the DM signal in gamma rays and discuss what the prospects of DM detection through gamma rays are.

The aforementioned cosmological simulations describe the mass distribution at a galactic level, while cluster-scale simulations like Phoenix A-1 and cosmic-scale simulations like DEUS FUR, Millennium, MultiDark, Horizon Run and Bolshoi are designed to describe larger scales. Independent of the scale, all these simulations predict substructures, i. e. the DM halo mass distribution is composed by a smooth component and the DM *clumps* or subhalos. Both of which are, to a very good approximation, spherically symmetric. Let us in the following characterize these structures in more detail.

3.4.1 Smooth component

The DM density profile that is inferred from the aforementioned simulations can be accurately fitted by the following parametrization

$$\rho_{(\alpha,\beta,\gamma)}(r) = \rho_0 \frac{R_0^\gamma}{r^\gamma} \left(\frac{1 + (R_0/r_s)^\alpha}{1 + (r/r_s)^\alpha} \right)^{\frac{\beta-\gamma}{\alpha}} , \tag{3.7}$$

where, for our galaxy, the normalization $R_0 \simeq 8.5\,\mathrm{kpc}$ (distance to the GC), $\rho_0 \simeq 0.4\,\mathrm{GeV/cm^3}$ (local DM density) is assumed. The benchmark values for the rest of the parameters are $(\alpha, \beta, \gamma) = (1, 3, 1)$ and $r_s \sim 20\,\mathrm{kpc}$ which correspond to the Navarro-Frenk-White (NFW) profile [86] for a Milky-Way like galaxy. However, the parameter sets $(\alpha, \beta, \gamma) = (1.5, 3, 1.5)$ [87] and $(\alpha, \beta, \gamma) = (2, 2, 0)$ [1] are also physically interesting and worth considering as we shall observe later. The divergent dependence $\rho \propto r^{-\gamma}$ of the DM profile (3.7) for small r means that the DM distribution has a cusp. However, galactic simulations can resolve only distances that are larger than a few 10 pc and thus, the radial dependence of the innermost region of the DM distribution and the very existence of a cusp remains uncertain.

A cusp-less variant, which is favoured by the latest simulations [85], is the Einasto profile

$$\rho_{\mathrm{Ein}}(r) = \rho_0\, \mathrm{e}^{-\frac{2}{\alpha}\left[\left(\frac{r}{r_s}\right)^\alpha - \left(\frac{R_0}{r_s}\right)^\alpha\right]} , \tag{3.8}$$

where $\alpha = 0.17$ and as before $r_s = 20\,\mathrm{kpc}$ gives the best fit to the Galactic halo.

Not surprisingly this type of distribution resembles the one defined by eq. (3.7) for everywhere but at the center ($r \to 0$) where no cusp is predicted. This DM profile is favoured by the *Aquarius* simulation while *Via Lactea II* in turn favours the NFW variant.

We notice in passing that none of the high-resolution N-body simulations describing the formation of DM halos include the effects of baryonic physics as no baryonic matter is taken into account. This is certainly a good approximation in the global sense as most of the matter is non-baryonic but locally, e. g. galaxy centers, effects such as baryonic contraction [88] can modify the degree of cuspiness of the DM profile. The exponent γ in eq. (3.7) could phenomenologically take into account such effects. The extreme case $\gamma = 1.5$ mentioned before –the associated model is commonly called the Moore profile– is such that the gamma-ray flux linked to DM annihilations at $r = 0$ becomes arbitrarily large. This is of course regularized by an equilibrium density plateau ρ_p such that the time scale of annihilations ($m_\chi/\rho_p\langle\sigma v\rangle$) and the age of the SMBH (10^8-10^{10} yr) sitting at the center of the galaxy are equal

3.4.2 DM Subhalos

In characterizing the DM halo substructure we will need to introduce some relevant quantities: virial mass and radius, concentration parameter, clump density, etc. Since the formation of structures is a hierarchical process, the profile of the DM subhalos ought to have the same form as their parent halos. For definiteness we will consider only NFW profiles keeping in mind, however, that this discussion can be extended to other halo models.

Notice that the result of integrating the DM density of an NFW profile –or, in general, of a profile like (3.7) with $\beta \leq 3$– over all space is formaly infinite. This does not represent a paradox since the profile is embedded in a larger continuous distribution that for radii larger than some characteristic *virial* radius $R_{\rm vir}$ starts to become the dominant component. Determining the size of the virial radius of a clump with virial mass M is done by multiplying the volume of a sphere with radius $R_{\rm vir}$ by the collapse overdensity $\Delta_c\rho_c$, where $\rho_c = 3H^2/8\pi G$ is the critical density defined in chapter 1. The parameter Δ_c can be estimated by $\Delta_c \approx 18\pi^2 - 82\Omega_\Lambda - 39\Omega_\Lambda^2$ [89].

The definition $R_{\rm vir}$ introduces a different length scale in addition to the scale parameter r_s. By dividing them we can define a universal variable (scale-independent) that quantifies how concentrated the substructure is. We call this variable the *concentration parameter* $c = R_{\rm vir}/r_s$. From the equation

$$(M =)4\pi\rho_s \int_0^{R_{\rm vir}} \frac{r^2\,\mathrm{d}r}{\frac{r}{r_s}\left(1+\frac{r}{r_s}\right)^2} = \frac{4\pi}{3}\Delta_c\rho_c R_{\rm vir}^3$$

we can analytically obtain the normalization ρ_s as a function of the concentration parameter

$$\rho_s(c) = \Delta_c\rho_c\frac{c^3}{3}\left[\log(1+c) - \frac{c}{1+c}\right]^{-1} \quad . \tag{3.9}$$

This equation holds only for a NFW profile. For other types of profiles, $\rho_s(c)$ is obtained numerically. In all cases, however, the scale-independent parameter c and the virial mass M describe the substructure completely.

N-body simulations are able to relate the virial mass with the concentration parameter down to masses $\sim 10^6 M_\odot$. However, the clump masses can be much smaller and extrapolations at larger mass scales are therefore needed. Unless very close, small clumps are in any case usually taken into a smooth average and resembling the form of the main halo profile.

In order to describe how subhalos are distributed in the main halo, the sub-halo number density $\mathrm{d}N/\mathrm{d}M$ is introduced: $\mathrm{d}N$ is the number of subhalos with masses

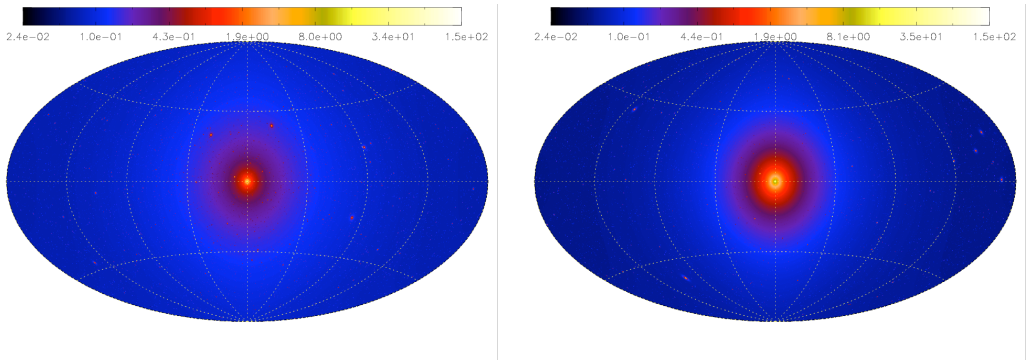

Figure 3.4: The prompt gamma-ray emission profile from DM annihilations in simulated halos including substructures [14]. Left: *Aquarius*. Right: *Via Lactea II*.

between M and $M + \mathrm{d}M$. Simulations have proven that the number density distribution follows a power law with exponent $\mu = 2 - \varepsilon^2$, with $\varepsilon \approx 0$ [85]:

$$\frac{\mathrm{d}N}{\mathrm{d}M} = \frac{\kappa}{M_0} \left(\frac{M}{M_0} \right)^{-\mu} . \tag{3.10}$$

If larger clumps are considered boosting effects can occur for instance in the gamma-ray flux. These are negligible when pointing at the center of the galaxy where there is less substructures. As an illustrative example the gamma-ray sky map that results from integrating all photon energies above 3 GeV is portrayed in fig. 3.4 for a DM candidate of mass $m_\chi = 40\,\mathrm{GeV}$ mainly annihilating into a $b\bar{b}$ state with thermal annhilation rate $\sigma v = 3 \times 10^{-26}\,\mathrm{cm}^3/\mathrm{s}$. The authors used the *Aquarius* (left panel) and the *Via Lactea II* (right panel) simulations in modeling the DM halo and subhalos. These maps were obtained in Ref. [14]

3.5 Have we already discovered DM through gamma rays?

In this section we will introduce the results of two recent analyses that showed indications of DM signals in the gamma-ray sky. In one case the energy spectrum of some subset of the FERMI-LAT data was shown to be compatible with the spectrum expected for a line or a VIB signal. In the other case, the spatial structure of the background-subtracted FERMI-LAT data and the energy spectrum seem also to be compatible with a DM signal from secondary gamma rays.

3.5.1 The 130GeV line

Recently, an analysis of the publicly available FERMI data based on a novel method [16] was able to tightly constrain the annihilation cross section into VIB photons while finding and indication of a possible signal peaked at the energy of 130 GeV. When interpreted in terms of DM annihilating into VIB photons, the DM would weight 150 GeV. A later analysis of one of the authors of Ref. [16] showed that using the same method one can also interpret such an excess in terms of a line signal [15].

Our discussion will mainly be concerned with such a *line* interpretation as we shall in chapter 5 scrutinize this hypothesis with a theoretically quite sophisticated machinery also discussed there. Nevertheless, most of the "line" analysis is identical to the one carried out in Ref. [16].

The original analysis reported in Ref. [15] was based on a 43-month FERMI-LAT dataset, featuring gamma-ray energies between 1 and 300 GeV. The novelty about the analysis carried out in both Refs. [15, 16] was that they developed a method that allowed them to select target regions that optimally resolve the DM signal. This of course depends on the DM profile and in light of the factorization property of the DM flux discussed in section 3.2, the problem of finding such an optimal target does not involve any consideration of the spectral shape of the DM signal.

In order to empirically be able to model the uncertain astrophysical background, the authors of Refs. [15, 16] used a template obtained from a data subset of energies that are uninteresting for their DM search ($E < 40\,\text{GeV}$ in [16] and $E < 20\,\text{GeV}$ in [15]) but whose correlation to the background noise at the "interesting" energies is expected to be large. The region of the sky that they investigate is defined by a latitude $|b| < 84\,^\circ$ and longitude $|l| < 90\,^\circ$.

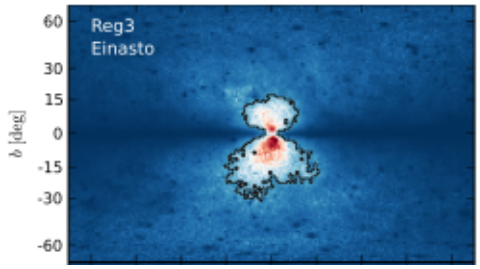

Figure 3.5: Target region used in the analysis of Ref. [15]. Pixels were selected in such a way that the DM search is optimized, following the method introduced in Ref. [16].

The algorithm they implement in order to approximately find the best target regions is a bit involved but is discussed in detail in both references. Fig. 3.5 portrays the target region that is optimal for DM searches if the DM distribution follows an Einasto profile (3.8).

Once the target is fixed, the $E > 20\,\text{GeV}$ data originated there can be applied some spectral fits. We first notice that owing to the bumpy shape of line signals in general, only a small energy "window" around the line's position $E = m_\chi$ will be necessary when searching for lines. This remark is of fundamental importance, since it allowed the authors to locally model the highly non-trivial background with a power law. The width of such sliding energy windows was adjusted according to the detector's energy resolution.

Figure 3.6 shows the results of fitting the data of the gamma-ray photons with $E > 20\,\text{GeV}$ from the optimal region 3.5 to a background plus a line signal at the 130 GeV energy. An comprehensive statistical analysis also carried out in [15] shows that the significance of the excess amounted to 4.3σ. However, since the scans over different sliding energy windows are statistically independent from each other, the probability of finding statistical fluctuations that resemble the line signal increases and therefore the line's significance effectively decreases. This fact is known as the look-elsewhere effect and it reduces the significance of the 130 GeV line down to 3.2σ. The best-fit values were then found to be $m_\chi = 129.8 \pm 2.4^{+7}_{-13}\text{GeV}$ and $\langle\sigma v\rangle_{\chi\chi\to\gamma\gamma} = (1.27 \pm +0.32^{+0.18}_{-0.28} \times 10^{-27})\text{cm}^3/\text{s}$ for the Einasto profile (3.8).

An independent later analysis reported in Ref. [90] confirmed these findings with even larger significances suggesting new gamma-ray detection strategies at FERMI – see also [91]–. By using a slightly different dataset the Fermi collaboration also found

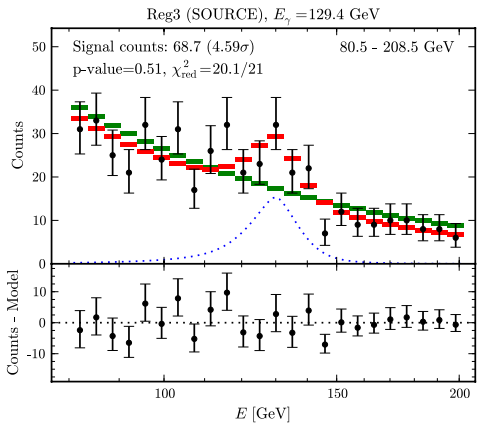

Figure 3.6: Statistical fit to the count of photons coming from the optimal region (3.5) as obtained in Ref. [15].

indications of a line-like signal at the 133 GeV energy but with a lower global significance of 1.5σ [92].

Nevertheless, after more years of data acquisition by FERMI, the significance of the line signal started to systematically drop as shown in figure 3.7. In section 5.2 we shall constrain the model building for the 130 line feature with the set of parameters originally described in Ref. [15].

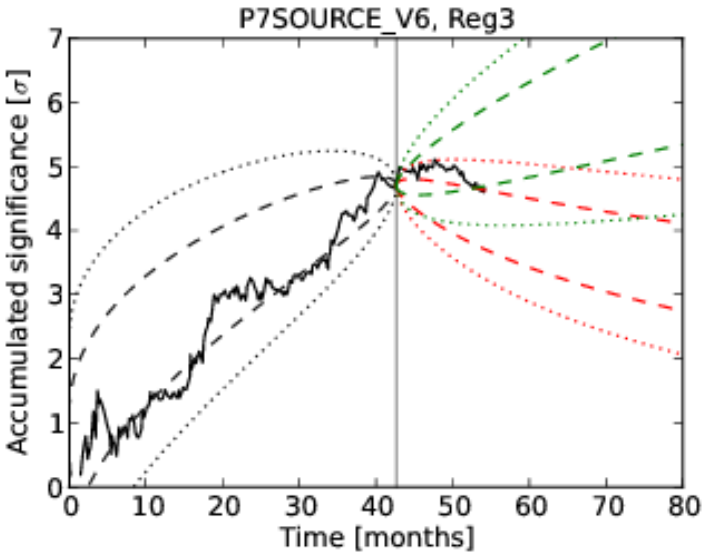

Figure 3.7: Significance of the 130 GeV feature as a function of data collection time [17].

3.5.2 The GeV excess

Another highly scrutinized case for DM is the so-called GeV *excess*. Originally suggested more than five years ago [93, 94] and recently revisited [24] this GeV excess could be explained by low-mass DM annihilating in the inner galaxy.

The authors of Ref. [24] also analyzed FERMI data taken between August 4, 2008

and December 5, 2013 and by applying a different event-selection scheme than the one customarily used by the *Fermi* collaboration they were able to spot a gamma-ray excess at the vicinity of the GC that is consistent with a DM interpretation.

In their study, they considered two different regions of interest (ROIs). The first one (*inner galaxy*) is defined in galactic coordinates by $|l| < 20^\circ$ and $1^\circ < |b| < 20^\circ$ while the second one (*galactic center*) by $|l| < 5^\circ$ and $|b| < 5^\circ$.

In both analyses after carrying out their refined event selection, they generated a set of sky maps binned in energy. In the inner-galaxy study they masked out the ROI's 300 brightest point sources. For several choices of the slope γ in

$$\rho_\gamma(r) = \rho_0 \frac{R_0^\gamma}{r^\gamma} \left(\frac{1 + R_0/r_s}{1 + r/r_s} \right)^{3-\gamma} , \tag{3.11}$$

they fitted the measured photons to the sum of three spatial background-photon templates: 1) diffuse component as modelled by the FERMI collaboration, 2) isotropic gamma-ray background and 3) *Fermi* bubbles. The fourth component is given by (3.2).

Figure 3.8 shows their results of their *inner galaxy* study. On the left panel we see how by varying the slope γ impacts the quality of the fits in terms of their *Test Statistics* (TS) variable. The preferred value was found to be $\gamma = 1.2$. In the first version a larger ROI was considered and the preferred value there was instead $\gamma = 1.28$. In section 5.4 and in Paper [II] we use the former.

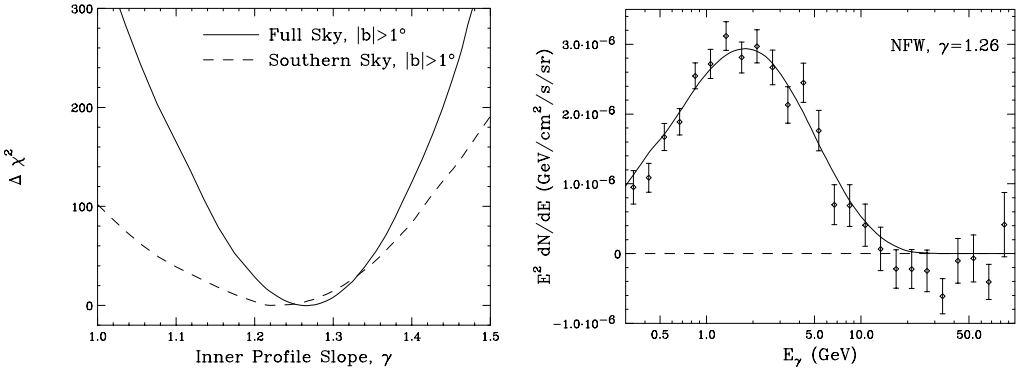

Figure 3.8: Left frame: TS as a function of the inner slope of the dark matter halo profile, γ for the full sky (solid line) and only the southern sky (dashed line). Right frame: DM component spectrum. A generalized NFW halo profile with an inner slope of $\gamma = 1.26$ (normalized to the flux at an angle of 5° from the GC) is assumed. Shown for comparison (solid line) is the spectrum predicted from WIMPs annihilating into $\bar{b}b$.

By fixing the spatial form of the DM signal through such an analysis, they fit the energy spectrum of the resulting DM templates for a set of different main annihilation channels and DM masses. The right panel of fig. 3.8 shows the (updated) resulting best-fit curve for the gamma-ray spectrum of the DM component if the DM were to annihilate mainly into $b\bar{b}$ pairs.

An almost identical analysis was done in the innermost region defined by $|l| < 5^\circ$ and $|b| < 5^\circ$ (GC analysis). The only difference was that they did not include the Fermi bubbles spatial template and instead of masking out point sources, they modelled them. In this analysis the resulting preferred slope region is broader $\gamma \in (1.04, 1.24)$ than the one encountered in the inner-galaxy study: $\gamma \in (1.15, 1.22)$.

In figure 3.9 we show in a annihilation-rate vs. DM mass parameter-space diagram the preferred values of the **Inner Galaxy** analysis of Ref. [24] for the several

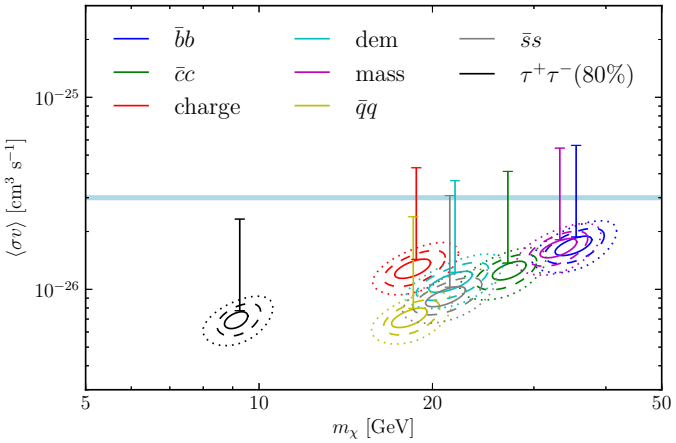

Figure 3.9: 1, 2 and 3σ contours of the preferred regions of the GeV excess if interpreted in terms of DM annihilating into the channels displayed in the figure. The upper ends of the bars indicate the centroids of the same regions for the shallower slope $\gamma = 1.04$

annihilation channels considered there. The error bars indicate the propagated uncertainties on the annihilation rate σv from considering the shallower profiles favoured by their **Galactic Center** analysis. In practical terms the upper ends of those error bars are obtained by multiplying the each blob centroid by the numerical factor $\rho^2_{\gamma=1.24}[r(3\,^\circ)]/\rho^2_{\gamma=1.04}[r(3\,^\circ)] \simeq 3.16$, where $r(3\,^\circ) \simeq 445\,\mathrm{pc}$ is the radial distance to the GC such that the subtended angle in relation to the Sun amounts to $3\,^\circ$.

The possibility that the GeV excess is really an indication of DM annihilations in the center of our galactic DM halo has certainly raised lots of interest in the community. We actually investigated the implications of this claim in other indirect detection channels in section 5.4. Most of the results we present there are also included in our paper [95].

Another related publication that received lots of attention and inspired some of the modifications for the newest version of Ref. [24] was Calore et al comprehensive study of the background model systematics [96]. The strongest result there is that the GeV excess energy spectrum can also be well fitted by a broken power law in contrast to typical spectra from secondary gamma-rays from DM annihilation into charged particles (see for instance fig. 3.8). The main reason why this is possible and compatible with the findings of Ref. [24] is that the background contribution is orders of magnitude larger than the signal expected from DM annihilation. Even relative small changes in the background field can lead to qualitative differences in the subdominant (DM) component.

Chapter 4

Radio

Astronomical observations in the radio band have been essential in the development of modern astronomy. Major discoveries in the 20th-century astronomy such as not only the CMB but also the first quasars and pulsars, and the 21-cm hydrogen line were achieved by radio astronomers

In this chapter we will introduce the possible imprints of WIMP DM on the radio sky. Although the data used in this thesis to e. g. put constraints on the DM models is not particularly new, the methods and theoretical models discussed in this chapters are the state-of-the-art tools for DM phenomenology in these frequencies. The fact that high-quality data from low-frequency radio interferometers such as the *Low Frequency Array* (LOFAR) [97] and the planned *Square Kilometre Array* (SKA) [98] will become available in the next few years, makes it crucial to deeply understand the DM signatures in radio.

4.1 Basic facts about radioastronomy

One of the reasons why radio observations are so useful is that in analogy to the optical radiation, for radio signals the atmosphere is transparent and, for a related reason, they can pass through interstellar regions that are impossible to penetrate by their optical counterpart. As a consequence, radio observations are one of our windows to e. g. the dynamics of the center of our galaxy.

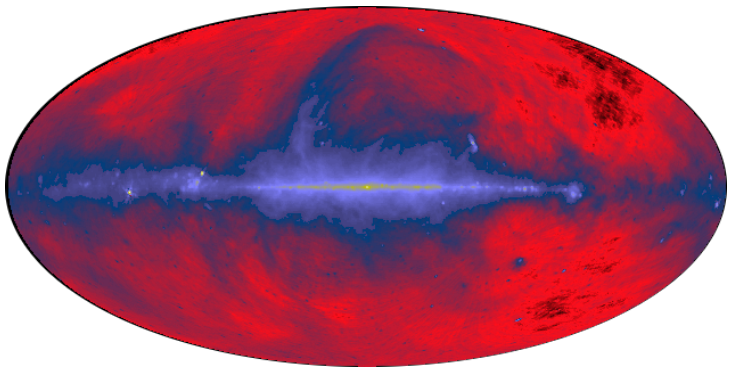

Figure 4.1: Max Planck Institute for Radio Astronomy. Full radio sky map generated by Glyn Haslam [18].

Due to the macroscopic scale of radio wavelengths, an enormous level of engineering is

required to attain a good angular resolution. Figure 4.1 shows the 408 MHz sky map that results from combining measurements of the radio antennas of three radio observatories: Jodrell Bank in England [99], the Max Plack Institute for Radioastronomy in Germany [100] and the Parkes Observatory in Australia [101].

Analogous to gamma rays, the bright spots in fig. 4.1 are distant radio sources such as pulsars, supernova remnants in our Galaxy and all different types of AGNs: radio galaxies, quasars, blazars, etc. There is also an isotropic background which has been recently characterized in Ref. [102] and investigated in the context of annihilating WIMP DM in Ref. [103]. The rest of the emission is mostly attributed to diffuse synchrotron radiation and thermal bremsstrahlung in interstellar nebulae.

In the next section we will describe the emission of radio waves through synchrotron radiation in quite some detail. We will however also briefly discuss the spectral features of the free free (bremsstrahlung) emission. As a final remark about the fascinating physics of radio astronomy, the polarization information of the observed radio waves can be used to learn about the interstellar magnetic field. This is done by means of the Faraday rotation measure RM

$$\mathrm{RM} = \frac{e^3}{2\pi m^2 c^4} \int \mathrm{d}s n_e(s) B_{\parallel}(s) \ , \tag{4.1}$$

where n_e is the number density of electrons that the radio wave faces in its path. This formula relates the axial component of the magnetic field $B_{\parallel}$ in the line of sight of the observed polarized source (typically a synchrotron emitter) with the observed angle of polarization $\theta_{\text{obs.}}$ through the formula $\theta_{\text{obs.}}(\lambda) - \theta_{\text{emit.}}(\lambda) = \mathrm{RM}\lambda^2$. Although the original polarization is of course not known, an spectral analysis suffices to be able to determine RM.

4.2 Synchrotron radiation

Charged particles accelerated by magnetic fields radiate in form of *synchrotron radiation*. Although its name refers only to laboratory experiments where this type of radiation was first observed [104], this phenomenon is present in countless physical settings. As mentioned before, several observations in radio astronomy are explained by synchrotron emission. In particular, annihilation or decay of DM particles may produce ultra-relativistic electrons and positrons that interact with ambient magnetic fields causing them to emit synchrotron radiation. In this section we will discuss the properties of such synchrotron signal focusing however on ultra-relativistic cosmic-ray electrons (positrons).

4.2.1 Angular dependence and trajectory

Given a charged particle's trajectory $\boldsymbol{r}(t)$ its associated radiated power per unit solid angle is obtained with aid of the Poynting vector $\boldsymbol{S}$ evaluated at a distance $R \to \infty$ and direction $\boldsymbol{n}$ by [19]

$$\frac{\mathrm{d}P(t')}{\mathrm{d}\Omega} = \lim_{R\to\infty} R^2 [\boldsymbol{S} \cdot \boldsymbol{n}](1 - \boldsymbol{\beta} \cdot \boldsymbol{n}) \ , \tag{4.2}$$

where the solid angle element $\mathrm{d}\Omega$ is constructed with respect to the particle's instantaneous position (see fig. 4.2), the $1 - \boldsymbol{\beta} \cdot \boldsymbol{n}$ factor is necessary in order for t' to indicate the particle's proper time. For a particle experiencing acceleration perpendicular to its

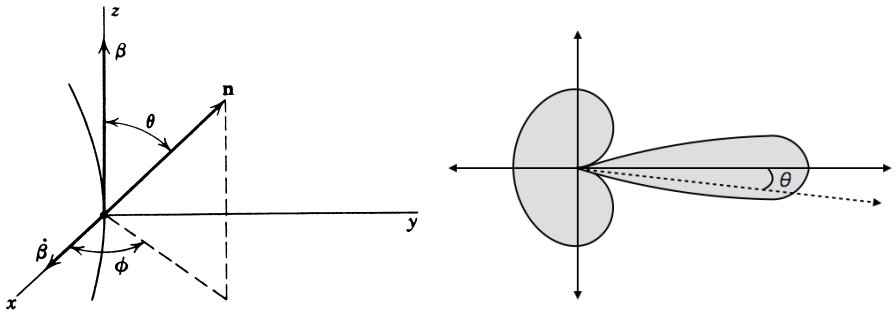

Figure 4.2: Right: graphical definition of the angular coordinates considered. Left: instantaneous emission profile of a ultra-relativistic synchrotron emitter. Images borrowed from J. D. Jackson's Classical Electrodynamics [19] and M. S. Longair's High Energy Astrophysics [20].

velocity, the resulting power reads

$$\frac{\mathrm{d}P(t')}{\mathrm{d}\Omega} = \frac{e^2}{(4\pi)c}\frac{\|\dot{\boldsymbol{\beta}}\|^2}{1-\beta\cos\theta}\left[1-\frac{\sin^2\theta\cos^2\phi}{\gamma^2(1-\beta\cos\theta)^2}\right] \ . \tag{4.3}$$

In order to better understand formula (4.3) notice that for ultrarelativistic particles the denominators become vanishing small at $\theta = 0$, meaning that most of the power goes in the forward direction of the particle's motion. It is therefore safe to expand trigonometric functions involving θ and take the leading terms as we will do henceforth. Right panel of figure 4.2 depicts the emission profile described by eq. (4.3). The emission can be shown to be constricted to a narrow cone of half angle $\Delta\theta \sim \gamma^{-1}$ in the direction of motion.

Let us now discuss the particular case of an ultrarelativistic charged particle with charge e in a uniform magnetic field $\boldsymbol{B}$. As it is well known, even without neglecting energy losses due to synchrotron radiation, the motion of such particle describes an helix around a magnetic field line[1]. The angular frequency is given by $\omega_B = ecB/E$, the *Larmor* radius $r_L = \beta_\perp c/\omega_B$ and the pitch angle α (angle between $\boldsymbol{B}$ and $\boldsymbol{v}$) is a free parameter. For the moment we set $\alpha = \pi/2$ (circular motion perpendicular to $\boldsymbol{B}$).

Notice that the angular coordinates in eq. (4.3) depend on t'. This means that an observer sitting at a fixed position will measure pulses of synchrotron radiation at a frequency $\nu_0 = \omega_B/2\pi$ (see fig. 4.3). By integrating eq. (4.3) we obtain the instantaneous radiated power

$$P_{\text{synch.}} = \frac{2}{3}\frac{e^2\|\dot{\boldsymbol{\beta}}\|^2}{c}\gamma^4 = \frac{2e^4B^2E^2}{3m_e^4c^7} \ . \tag{4.4}$$

Conservation of energy implies that $P(t') = -\,\mathrm{d}E/\,\mathrm{d}t'$. In one period

$$\delta T_B = 2\pi/\omega_B = \frac{2\pi E}{ecB} \sim 1\,\mathrm{h}\left(\frac{B}{\mu\mathrm{G}}\right)^{-1}\left(\frac{E}{\mathrm{GeV}}\right)$$

[1] A convincing way to realize that energy losses affect very little the particle's orbit is by noticing that even big variations of $\gamma(\gg 1)$ do not affect the condition $\beta \simeq 1$.

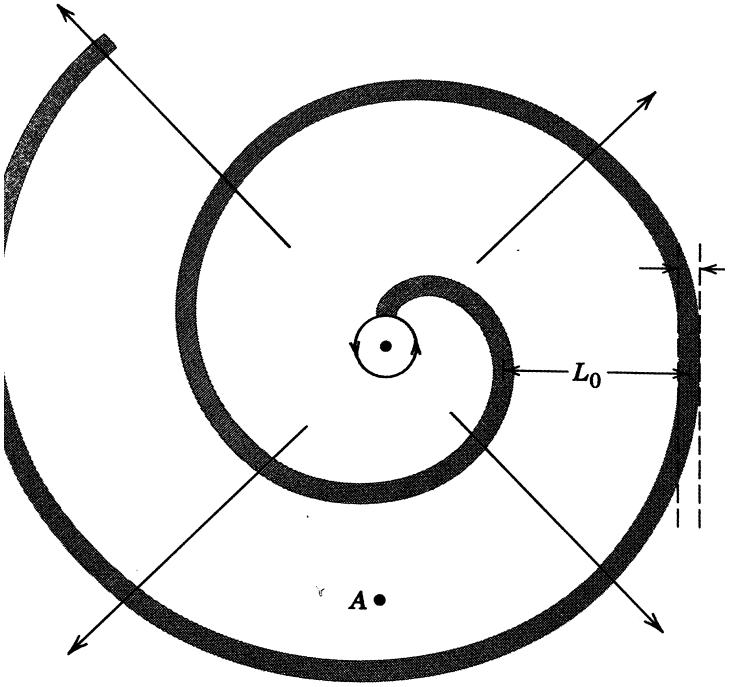

Figure 4.3: Synchrotron radiation wavefronts of ultrarelativistic charged particles in circular motion. Image from [19].

the induced change in E is extremely small:

$$\frac{\delta E}{E} = -\frac{4\pi e^3 B E^2}{3 m_e^4 c^8} \sim -10^{-15} \left(\frac{B}{\mu\mathrm{G}}\right) \left(\frac{E}{\mathrm{GeV}}\right)^2 . \tag{4.5}$$

This condition certainly supports the assumption that the radiating electron's trajectory is well described as a perfect helix. In the following we shall focus on the frequencies that the synchrotron radiation is able to produce.

4.2.2 Spectrum

The frequency span of the synchrotron radiation is very rich as it involves a wide range of frequencies that can be estimated by first principles. From figure 4.3 we notice that observers will measure an almost exact periodic emission profile with fundamental frequency $\omega_0 = \omega_B$ (c/L_0 in fig. 4.3). As a consequence of the syncrhotron radiation's pulsating structure, the first modes of its Fourier expansion will give negligible contributions while high frequencies $\omega_c \sim c/L$ (or equivalently higher-order modes $\sim L_0/L$) will dominate. The discreteness property of the spectrum can therefore be disregarded (large Fourier-mode limit).

Estimation of ω_c (or L in fig. 4.3) can be done in two steps. First, observable radiation will be emitted in a time $\Delta t_* = \Delta s/v \simeq r_L \Delta\theta/c\beta$, where Δs is the distance traveled by the particle while it emits observable radiation and $v = c\beta$ is its speed. Second, notice that the arrival times differ from Δt_* due to the fact that radiation

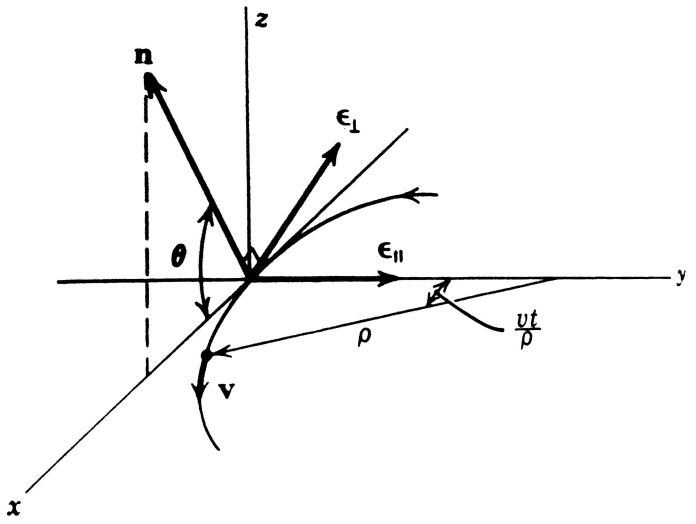

Figure 4.4: Graphical definition of polarization vectors and curvature radius. Image from [19].

moves at the speed of light[2], and therefore

$$\Delta t = \frac{L}{c} = \left(\frac{1}{\beta} - 1\right)\frac{r_L}{c\gamma} \simeq \frac{r_L}{c\gamma^3} = \frac{1}{\gamma^3\omega_0} \ ,$$

where we used $\Delta\theta \simeq \gamma^{-1}$. As customary we define the cutoff frequency $\omega_c \sim 1/\Delta t$ of the synchrotron emission as

$$\omega_c \equiv \frac{3}{2}\left(\frac{E}{mc^2}\right)^3 \omega_B = \frac{3eE^2B}{2m^3c^5} \ . \tag{4.6}$$

With this expression we can estimate the number of photons emitted per cycle $N_{\rm cyc}$ by multiplying eq. (4.5) by $E/\hbar\omega_c$ yielding

$$N_{\rm cyc} = 2 \times 10^6 \left(\frac{E}{\rm GeV}\right) \ .$$

Interestingly, the expression is independent of B and the large number justifies the classical treatment of this phenomenon.

A formal treatment of the spectrum of the synchrotron emission in the general $\alpha \neq 0$ case can be done by considering the Fourier decomposition of eq. (4.2), which after some amount of algebra can be written as

$$\frac{\mathrm{d}^2W}{\mathrm{d}\omega\,\mathrm{d}\Omega} = \frac{e^2}{4\pi^2c}\left|\int \mathrm{d}t\boldsymbol{n}\times(\boldsymbol{n}\times\boldsymbol{\beta})\,\mathrm{e}^{i\omega(t-\boldsymbol{n}\cdot\boldsymbol{r}(t)/c)}\right|^2 \ , \tag{4.7}$$

where in contrast to eq. (4.2) the solid angle element $\mathrm{d}\Omega$ here refers to fixed direction in space. Nevertheless, owing to the localized –in angular terms– property of the synchrotron emission both solid angle elements are the same for the times where there will be actual radiation emitted in that direction. By choosing a system of coordinates such that the z axis is perpendicular to the instantaneous trajectory plane and defining

[2]Think the pulse as a rectangular train of energy. While the front edge travels a distance $c\Delta t_*$ the rear one will be behind the front one by a distance $c\Delta t_* - \Delta s$

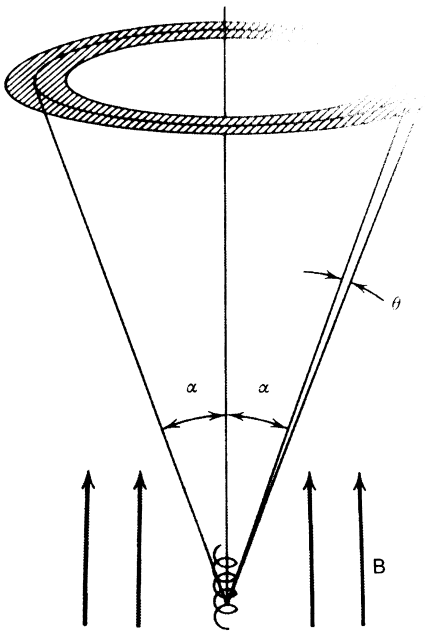

Figure 4.5: Time averaged emission profile of a synchrotron emitter traveling with a pitch angle α. Image from [21].

unitary vectors $\boldsymbol{\epsilon}_\perp$ and $\boldsymbol{\epsilon}_\parallel$ as displayed in figure 4.4, the vectorial prefactor and exponent in eq. (4.7)'s integrand can be written as [21]

$$\boldsymbol{n}\times(\boldsymbol{n}\times\boldsymbol{\beta}) = -\boldsymbol{\epsilon}_\parallel\beta\sin(\omega_{B_\perp}t) + \boldsymbol{\epsilon}_\perp\beta\cos(\omega_{B_\perp}t)\sin\theta \simeq -\boldsymbol{\epsilon}_\parallel\omega_{B_\perp}t + \boldsymbol{\epsilon}_\perp\theta$$

$$\omega\left(t - \tfrac{\boldsymbol{n}\cdot\boldsymbol{r}(t)}{c}\right) = \omega\left(t - \tfrac{r_L}{c}\sin\omega_{B_\perp}t\cos\theta\right) \simeq \tfrac{\omega}{2}\left(\left[\tfrac{1}{\gamma^2}+\theta^2\right]t - \tfrac{\omega_{B_\perp}^2}{3}t^3\right)\left[1+\mathcal{O}(\gamma^{-2})\right]$$

where we introduced $\omega_{B_\perp} = ecB_\perp/E = \omega_B\sin\alpha$. We can thus write

$$\tfrac{\mathrm{d}^2W}{\mathrm{d}\omega\,\mathrm{d}\Omega} = \tfrac{e^2}{4\pi^2c}\left|-\boldsymbol{\epsilon}_\parallel A_\parallel(\omega) + \boldsymbol{\epsilon}_\perp A_\perp(\omega)\right|^2 \tag{4.8}$$

$$A_\parallel(\omega) = \omega_{B_\perp}\int \mathrm{d}t t\exp i\tfrac{\omega}{2}\left[\left(\tfrac{1}{\gamma^2}+\theta^2\right)t - \tfrac{\omega_{B_\perp}^2}{3}t^3\right] = \tfrac{i}{\sqrt{3}\omega_{B_\perp}}\left(\tfrac{1}{\gamma^2}+\theta^2\right)K_{2/3}(\xi)$$

$$A_\perp(\omega) = \theta\int \mathrm{d}t\exp i\tfrac{\omega}{2}\left[\left(\tfrac{1}{\gamma^2}+\theta^2\right)t - \tfrac{\omega_{B_\perp}^2}{3}t^3\right] = \tfrac{1}{\sqrt{3}\omega_{B_\perp}}\left(\tfrac{1}{\gamma^2}+\theta^2\right)^{1/2}K_{1/3}(\xi)$$

$$\xi \equiv \tfrac{\omega}{3\omega_{B_\perp}}\left(\tfrac{1}{\gamma^2}+\theta^2\right)^{3/2}\ ,$$

where $K_\nu(\xi)$ are modified Bessel functions of order ν.

The decomposition (4.8) allows us to learn about the polarization properties of the synchrotron emission as the unitary vectors $\boldsymbol{\epsilon}_\perp$ and $\boldsymbol{\epsilon}_\parallel$ are precisely the polarization vectors of the radiation field. By integrating (4.8) over all angles we obtain the radiated energy per unit frequency radiated in one orbit for both polarizations:

$$\tfrac{\mathrm{d}W_\perp}{\mathrm{d}\omega} = \tfrac{\sqrt{3}e^2E\sin\alpha}{2mc^3}\left[F\left(\tfrac{\omega}{\omega_{c\perp}}\right) + G\left(\tfrac{\omega}{\omega_{c\perp}}\right)\right] \tag{4.9}$$

$$\tfrac{\mathrm{d}W_\parallel}{\mathrm{d}\omega} = \tfrac{\sqrt{3}e^2E\sin\alpha}{2mc^3}\left[F\left(\tfrac{\omega}{\omega_{c\perp}}\right) - G\left(\tfrac{\omega}{\omega_{c\perp}}\right)\right] \tag{4.10}$$

$$F(x) = x\int_x^\infty \mathrm{d}\xi K_{5/3}(\xi)\ ,\ G(x) = xK_{2/3}(x) \tag{4.11}$$

where $\omega_{c\perp}$ is obtained by making the substitution $B \to B \sin\alpha$ and the angular integration was actually confined to the cone shown in figure 4.5 ($\mathrm{d}\Omega \to 2\pi \sin\alpha \, \mathrm{d}\theta$). The total energy radiated in one orbit per unit frequency is therefore

$$\frac{\mathrm{d}W}{\mathrm{d}\omega} = \frac{\sqrt{3}e^2 E \sin\alpha}{mc^3} F\left(\frac{\omega}{\omega_{c\perp}}\right) \ . \tag{4.12}$$

After a highly non-trivial argument discussed in the appendix B the associated power is obtained by dividing this expression by one period $T = 2\pi/\omega_B$ yielding

$$\frac{\mathrm{d}P_{\mathrm{synch.}}}{\mathrm{d}\omega} = \frac{\sqrt{3}e^3 B \sin\alpha}{2\pi mc^2} F\left(\frac{\omega}{\omega_{c\perp}}\right) \ , \tag{4.13}$$

which, when integrated, leads to formula (4.4) modulo the transformation $B \to B_\perp$. This formula is the central result of this section. In figure 4.6 we show in arbitrary units and for $\alpha = \pi/2$ such a spectrum.

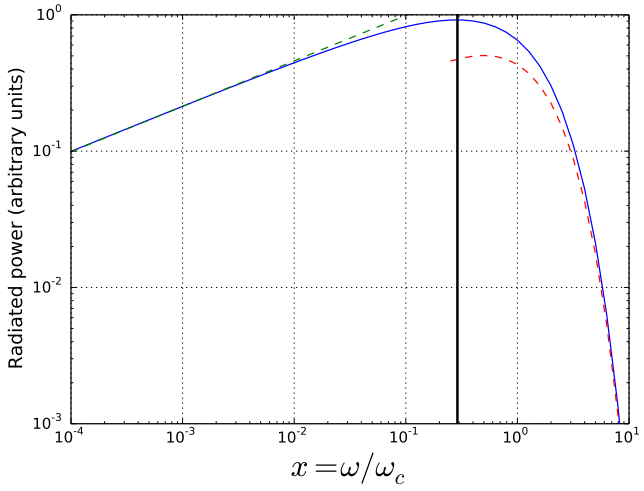

Figure 4.6: Synchrotron radiation spectrum. Dashed green and red lines graphically represent the low (4.14) and high (4.15) frequency tails of the spectrum respectively.

We see that the synchrotron spectrum is characterized by a very broad flat part at frequencies below ω_c which can be estimated by a soft power law

$$\frac{\mathrm{d}P_{\mathrm{synch.}}}{\mathrm{d}\omega} \sim \frac{e^2\omega_B}{c}\left(\frac{\omega}{\omega_B}\right)^{1/3} \quad \omega \ll \omega_c \, . \tag{4.14}$$

At the other end of the spectrum one finds a sharp cutoff at frequencies of the order of ω_c reaching a maximum at $\omega \simeq 0.29\omega_c$. The functional dependence of the spectrum at the high frequency limit is given by

$$\frac{\mathrm{d}P_{\mathrm{synch.}}}{\mathrm{d}\omega} \simeq \sqrt{3\pi/2}\frac{e^2\omega_B}{2\pi mc^3}\left(\frac{\omega}{\omega_B}\right)^{1/2} \mathrm{e}^{-\omega/\omega_c} \quad \omega \gg \omega_c \, . \tag{4.15}$$

4.2.3 Energy losses revisited

Let us, as usually done in the literature, rewrite the emitted energy –or equivalently the absolute value of the particle energy loss rate (4.4)– in terms of the electromagnetic energy density $u_{\rm EM} = B^2/8\pi$

$$-\frac{{\rm d}E}{{\rm d}t} = P_{\rm synch.} = \frac{2\sigma_{\rm T} u_{\rm EM} E^2 \sin^2\alpha}{m^2c^3} \ , \tag{4.16}$$

where $\sigma_{\rm T} = 8\pi e^4/m^2c^4$ is the total Thomson scattering cross section (between a classical electron and an electromagnetic radiation field). For an ensemble of electrons with random orientations, the average energy loss rate over pitch angles will also prove to be useful:

$$\left\langle \frac{{\rm d}E}{{\rm d}t} \right\rangle_{\rm pitch} = -\frac{2\sigma_{\rm T} u_{\rm EM} E^2}{m^2c^3}\frac{1}{2}\int_0^\pi {\rm d}\alpha \sin\alpha \sin^2\alpha = -\frac{4\sigma_{\rm T} u_{\rm EM} E^2}{3m^2c^3} \ , \tag{4.17}$$

where the average is performed over al solid angle elements ${\rm d}\Omega = 2\pi \sin\alpha \, {\rm d}\alpha$. In the next subsection we discuss such averaging at the fluxes level.

4.2.4 Pitch-angle average

The discussion presented in this section has so far been concerned with the synchrotron emission of electrons in anuniform magnetic field. In practice this assumption is not valid globaly: galactic magnetic fields are turbulent and unfortunately up-to-date there remain countless open questions as to the details on how they are generated. We can however make use of basic known facts in order to understand the synchrotron signals that high energetic electrons produce in the regions of interest to this work and ultimately justify that pitch angles can be averaged out.

The central argument here is that the coherence length of the interstellar magnetic field is $\mathcal{O}(10 - 100\,{\rm pc})$ which is several orders of magnitude larger than typical Larmor radii of $\sim$ GeV electrons ($\sim 10^{-6}\,{\rm pc}$). Therefore, locally the results just discussed can safely be regarded as exact. In more generic cases, however, the direction of the magnetic field will significantly vary within the observed regions as well as along the line of sight. It is thus reasonable to assume that all synchrotron radiation that we receive from a specific direction is produced by a randomly oriented magnetic field such that, on average, the power radiated by a single electron synchrotron per unit frequency is given by

$$\left\langle \frac{{\rm d}P}{{\rm d}\omega} \right\rangle_{\rm pitch} = \frac{\sqrt{3}e^3 B}{4\pi mc^2}\int_0^\pi {\rm d}\alpha \sin^2\alpha F\left(\frac{\omega}{\gamma^3\omega_B \sin\alpha}\right) \ . \tag{4.18}$$

Such integration can be carried out analytically [105] yielding

$$\frac{{\rm d}P_{\rm random}}{{\rm d}\omega} = \frac{2\sqrt{3}e^3 B}{\pi mc^2}x^2\left(K_{4/3}(x)K_{1/3}(x) - \frac{3}{5}x[K^2_{4/3}(x) - K^2_{1/3}(x)]\right) \ , \tag{4.19}$$

with $x = \omega/\omega_c$.

4.2.5 Monochromatic approximation

Formulas (4.13) and (4.19) provide a very accurate description of the physics of synchrotron radiation. However, one encounters quite often cases where astronomical uncertainties are so big that it is possible to give up the accuracy in favor of the practical,

e. g. saving computation time. Therefore, it is common for people to assume that the synchrotron spectrum of high energetic particles is composed by a single frequency $\omega = 0.29\omega_c$ –the frequency where the power 4.13 is maximized–. In mathematical terms this is equivalent to making the identification

$$F(x) = x\int_x^\infty \mathrm{d}\xi K_{5/3}(\xi) \to \frac{8\pi}{9\sqrt{3}}\delta(x-0.29)\ .$$

This approximation, besides making the calculations easier, serves as a pedagogical tool that helps to understand complicated physical phenomena where synchrotron radiation is emitted. Additionally, the fact that the synchrotron power has abrupt feature around the critical frequency makes this approximation a bit sensible.

4.3 Diffusion-loss equation

The synchrotron radiating electrons and positrons that will interest us will scatter with the turbulent magnetic field in a random manner while adiabatically losing their energy –eq. (4.5) makes this evident–. Both effects are captured in a special limit of the Boltzmann equation, namely the *diffusion-loss equation*. An instructive way of deriving this equation is given in Longair's textbook [20]. In the following we will reproduce such a derivation.

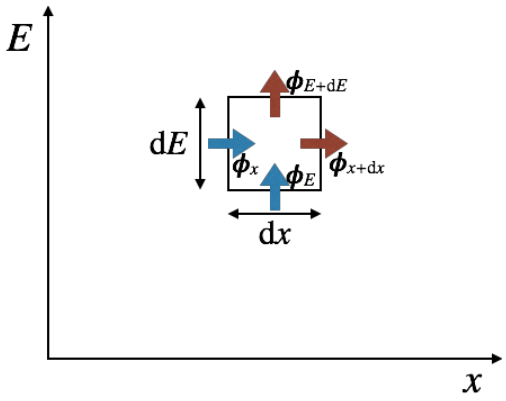

Figure 4.7: Diagram illustrating the continuity equation in a phase-space element. Image inspired from [20].

Let us consider an ensemble of particles in one dimension. Each particle will be completely identified by its position x and its energy (or momentum) E. We thus define $n_E(x;t)$ as the particle number per unit energy and per unit length and derive an equation that describes its dynamics by requiring that the total flux of particles in a phase-space element vanishes unless there is a mechanism injecting new particles –e. g. DM annihilations–.

As portrayed in figure 4.7, the number of particles $\delta n(t) = n_E(x;t)\,\mathrm{d}E\,\mathrm{d}x$ in a phase-space element can change both by (*i*) the inflow or outflow of particles with the same energy from either side (left or right of x) into or out of the line element $\mathrm{d}x$ and by (*ii*) the energy loss or gain of particles sitting at point x. Taking both effects into account at once, plus the possibility that particles are injected leads to

$$\frac{\mathrm{d}}{\mathrm{d}t}(\delta n(t)) = -(\Phi_{x+\mathrm{d}x}(E) - \Phi_x(E))\,\mathrm{d}E - (\Phi_{E+\mathrm{d}E}(x) - \Phi_E(x))\,\mathrm{d}x + q(x,E;t)\,\mathrm{d}x\,\mathrm{d}E$$

$$\frac{\partial n_E(x;t)}{\partial t}\,\mathrm{d}x\,\mathrm{d}E = -\frac{\partial \Phi_x(E;t)}{\partial x}\,\mathrm{d}x\,\mathrm{d}E - \frac{\partial \Phi_E(x;t)}{\partial E}\,\mathrm{d}x\,\mathrm{d}E + q(x,E;t)\,\mathrm{d}x\,\mathrm{d}E\ ,$$

$$\frac{\partial n_E(x;t)}{\partial t} = -\frac{\partial \Phi_x(E;t)}{\partial x} - \frac{\partial \Phi_E(x;t)}{\partial E} + q(x,E;t)\ , \tag{4.20}$$

where $q(x,E;t)\,\mathrm{d}x\,\mathrm{d}E$ is the number of injected particles per unit time and Φ_x, Φ_E are the components of phase-space current density.

4.3.1 Diffusion term

The first term on the right-hand side of equation (4.20) can easily be recognized. It is namely the one-dimensional divergence of the particle number's current density Φ_x. For a "coherent" velocity field, the familiar formula in fluid dynamics and electromagnetism $\Phi_x = n_E(x;t)v(x;t)$ applies. However, in the cases we will confront here, particle motion is better described by a *random walk*, i. e. the number of incoming and outgoing particles is randomly distributed. When the number of particles is large and the time scale of interest is larger than the time scale of the random walk steps, this transport mechanism is well described by Fick's law

$$\Phi_x = -D(x,E;t)\frac{\partial n_E}{\partial x}\ . \tag{4.21}$$

The diffusion coefficient $D(x,E;t)$ in equation (4.21) encompasses all the physics of the random walk in just one function. A rather neat way of physically understanding D is the following: consider a single particle in a random walk, at time scales larger than the typical random-walk time step, the average particle's position will be unchanged ($\langle\Delta x\rangle(t) = 0$). Nevertheless, the dispersion $\langle\Delta x^2\rangle(t)$ will be different from zero and will actually increase linearly with time. The proportionality constant is thus the diffusion coefficient: the larger the diffusion coefficient the farther a particle can travel diffusively.

Fick's law can formally be obtained from the assumption that the motion of the particles are described by random walks. We will however content ourselves by noticing that essentially, eq. (4.21) states that particles move from regions with larger n_E to regions with smaller n_E (Φ_x is proportional to minus the gradient of the particle density). In three dimensions eq. (4.21) is a tensorial equation:

$$\Phi_i = -D_{ij}\frac{\partial n_E}{\partial x_j}\ .$$

If isotropy is assumed then, $D_{ij} = D\delta_{ij}$. This simplifying assumption is usually taken in the literature and proves successful in fitting cosmic ray data Although electrons and positrons may interact with heavy particles in the ISM through Coulomb processes, most of their diffusion is caused by the scattering driven by the turbulent interstellar magnetic field. Relevant quantities in deriving diffusion coefficients are the magnetic field coherence length, the Larmor radius and the pitch angle of the scattered particle. The simplest diffusion coefficient that can be constructed with these ingredients is the *Bohm diffusion* coefficient

$$D_{\mathrm{Bohm}} = \frac{1}{3}r_{\mathrm{L}}c = \frac{Ec}{3eB}\,. \tag{4.22}$$

This model for diffusion however fails at describing the observed cosmic ray fluxes. Some extra degree of sophistication in the modelling of the diffusion coefficient is thus necessary.

Although a complete and satisfactory theoretical understanding of diffusion processes of charged particles in a turbulent magnetic field remains an open problem, we still can introduce an alternative model for the diffusion coefficient by e. g. relating it with the coherence length of the turbulent magnetic field.

The way this is done is by means of the classical method of the *adiabatic invariants* [106]. One can show that the pitch angle α is "scattered" by the turbulent magnetic field by an amount $\delta\alpha \propto \delta B/B$ if the fluctuations of the magnetic field occur on length scales larger than the Larmor radius. Under these assumptions the diffusion coefficient reads

$$D \simeq D_{\text{Bohm}} \left(\frac{\langle B \rangle}{\delta B} \right)^2 \Bigg|_{k \sim r_L^{-1}} = D_0 \beta \left(\frac{E}{\text{GeV}} \right)^{\delta} . \tag{4.23}$$

where k is the Fourier variable of the spatially fluctuating magnetic field. The expression on the left hand side is customarily used in the context of cosmic ray research. The index δ is determined by the magnetic field turbulence. Canonical theoretical models predict $\delta = 1/3$ (Kolmogorov) and $\delta = 1/2$ (Kraichan). However, this index is usually regarded as a free parameter that will be fitted with the data. For a unquestionably comprehensive discussion about these topics we refer to the modern textbook [70] and the reference therein.

4.3.2 Energy loss term

Let us now move to the next term in the left-hand side of eq. (4.20). This term resembles the first one, being in this case the energy the differentiated variable. In contrast to the previous case where we disregarded the possibility of convective transport $\Phi_x = n_E(x;t)v(x;t)$ in favor of diffusive one, the current density in energy space Φ_E is better described by an analog formula to the convective one $\Phi_E = n_E(x;t)b(E;t)$ for the type of processes responsible for the electron's energy losses. Following the directions of such analogy, we identify the function $b(E;t)$ as the energy gain or loss of single particles ($v(x;t) = \mathrm{d}x/\,\mathrm{d}t \to b(E;t) = \mathrm{d}E/\,\mathrm{d}t$). The term $\partial(bn_E)/\partial E$ is known as the *energy loss term* although the function b can also account for energy gains which are however rare in the astrophysical setups that are typically considered.

A diffusion term in energy (or momentum) space has also physically interesting applications. Not surprisingly the diffusion coefficient in momentum space will actually be related to the spatial diffusion coefficient just discussed. For the cases of interest in this work one can show that diffusion in momentum space is negligible respect to either energy losses or spatial diffusion, provided that no Alfvén instabilities are present [20, 70].

Since our main interest in this section is to describe how DM-induced electrons and positrons propagate while they emit synchrotron radiation, we focus on the mechanisms responsible for their energy losses in the interstellar medium. These are namely inverse Compton scattering, synchrotron radiation, bremsstrahlung and Coulomb scattering.

The energy losses due to synchrotron radiation were extensively discussed in the previous section and are given by formula (4.17):

$$\left(\frac{\mathrm{d}E}{\mathrm{d}t} \right)_{\text{synch.}} = -\frac{4\sigma_{\text{T}} u_{\text{EM}} E^2}{3m^2c^3} = -2.5 \times 10^{-20} \left(\frac{B}{10\mu\text{G}} \right)^2 \left(\frac{E}{0.01\,\text{GeV}} \right)^2 \text{GeV/s} . \tag{4.24}$$

We shall in the following briefly introduce these processes and show without derivation their corresponding energy loss rates.

4.3.2.1 Inverse Compton Scattering

As discussed in the previous chapter, an inverse Compton scattering occurs when a high energy electron encounters a low energy photon (typically from the CMB). In this process most of the electron's energy is transferred to the photon. The energy loss associated to this kind of process has a similar functional form to the synchrotron radiation one

$$b_{\rm ICS} = -\frac{4\sigma_{\rm T} u_{\rm rad.} E^2}{3m^2c^3} \ . \tag{4.25}$$

This is not very surprising as synchrotron radiation and ICS stem from essentially the same process: charged particle in a background electromagnetic field. The radiation field can vary from region to region but in most of the cases it is a safe assumption to use the CMB energy density $u_{\rm rad.} = 0.25\,{\rm eV/cm^{-3}}$ in formula (4.25), i. e. assume that the radiation field is solely composed by CMB photons.

4.3.2.2 Bremsstrahlung

Electrons may also emit radiation as a consequence of their accelerated motion when they are scattered off by heavier particles –typically protons or helium ions– in the ISM. Although the correct description of this process requires a quantum treatment, some classical considerations serve as guidance.

Usually bremsstrahlung processes are better visualized in the Weizsäcker-Williams methode of *Virtual Quanta*. In this method, one studies the process in the rest frame of the incident electron (or positron). In this frame, the heavier particle moves relativistically which means that its field lines are almost perfectly transverse to its motion. Therefore, the electron experiences a pulse of virtual radiation right when the heavier particle passes by. The interaction between the pulse of virtual radiation and the electron can be regarded as a Thomson (Compton) scattering where a real photon is emitted [21]

$$\frac{{\rm d}W'}{{\rm d}\omega'} = \sigma_T \frac{{\rm d}^2W'}{{\rm d}A'\,{\rm d}\omega'} \ , \tag{4.26}$$

where ${\rm d}^2W'/\,{\rm d}A'\,{\rm d}\omega'$ is the spectrum of the virtual photon in the rest frame of the electron. Transforming back to the original frame and yields

$$\frac{{\rm d}P_{\rm brem}}{{\rm d}\omega} \simeq \frac{16Z^2e^6n_{\rm ion}}{3m_e^2c^4} \ln\left(\frac{0.68E^2}{\hbar\omega m_e c^2}\right) \ , \tag{4.27}$$

where Z and n are respectively the charge and number density of the scattered ions. This formula is of course only valid for soft photons ($\hbar\omega \ll E$) where the classical description is valid. For larger frequencies, one can still use this method if instead of the Thomson scattering differential cross section we use the corresponding (Compton scattering) Klein-Nishina formula. The energy loss that is results from integrating eq. (4.27) over all frequencies yields

$$b_{\rm brem} \simeq \frac{16Z^2e^6n_{\rm ion}0.68E^2}{3m_e^3c^6} \int_0^{m_ec^2/0.68E} (-\ln x)\,{\rm d}x = \frac{16Z^2e^6n_{\rm ion}E}{3m_e^2c^4} \ln\left(\frac{0.25E}{m_ec^2}\right) \ . \tag{4.28}$$

Even though this formula is far from exact, it provides a good approximation for the total energy loss rate due to bremsstrahlung of electrons in the interstellar gas. The equations just derived can also be adapted to the closely related process of *free free absorption* where instead, radiation is absorbed by an electron passing by a heavy nucleus. We refer the reader to Ref. [21] for a detailed account of this interesting phenomenon.

4.3.2.3 Coulomb Scattering

At lower energies, bremsstrahlung ceases to be the dominant cause for the electron's energy loss in a electron-nucleus scattering process. Most of the energy losses of the electron are thus due to their scattering in the Coulomb field of the nucleus. In a ionized medium the energy loss rate is [19]

$$b_{\rm Coul} \simeq \frac{4\pi Z^2 e^4 n_{\rm ion}}{m_e c\beta}\left[\ln\left(\frac{\sqrt{2}pc}{\langle E_{\rm ion}\rangle}\right) - \beta^2\right] \ , \tag{4.29}$$

where $\langle E_{\rm ion}\rangle$ is the mean excitation energy of the bound state that the target nucleus and the impinging electron would form if the former traps the latter.

4.3.3 Source (injection) term

The last term in the right-hand side of eq. (4.20) is the most important one. Without this term, the physically interesting solutions to the diffusion-loss equation would actually vanish. In order to better understand the injection term, let us for a moment assume no energy transport. In this case, eq. (4.20) simply states that the particle density at a given point in phase space increases (it decreases if q is negative: particle leakage case) at the rate given by $q(x, E; t)$. By promoting eq. (4.20) to three dimensions:

$$\frac{\partial n_E(\boldsymbol{r};t)}{\partial t} = \boldsymbol{\nabla}\cdot(D(\boldsymbol{r},E;t)\boldsymbol{\nabla}n_E(\boldsymbol{r};t)) - \frac{\partial}{\partial E}(-b(\boldsymbol{r},E;t)n_E(\boldsymbol{r};t)) + Q(\boldsymbol{r},E;t) \ , \tag{4.30}$$

the injection function in the context of DM annihilations obtained in previous chapters reads

$$Q(\boldsymbol{r},E) = \frac{\langle\sigma v\rangle}{2m_\chi^2}\rho_\chi^2(r)\sum_c {\rm BR}_c\left(\frac{{\rm d}N_e}{{\rm d}E}\right)_c \ , \tag{4.31}$$

where, as usual, an extra factor of 1/2 should be included if the DM particle is not its own anti-particle. In passing, we point out that, henceforth, $b(\boldsymbol{r}, E; t)$ will refer to the particle's energy **loss** rate, i. e. b is positive if the particle loses energy and negative if it gains energy.

The solutions of interest of eq. (4.30) are those which are proportional to $\langle\sigma v\rangle$. Many other solutions are mathematically possible but the number density that results from them can no longer be interpreted as originated from DM annihilation. Formally speaking, the diffusion-loss equation is a linear inhomogeneous equation and as such, adding any solution of the homogenous equation (the equation that results from setting $Q = 0$) to a solution of the inhomogeneous one is also a solution of the latter.

4.3.4 Time scales in the diffusion-loss equation

Equation 4.30 can not be solved analytically for arbitrary functions $D(\boldsymbol{r}, E; t)$ and $b(\boldsymbol{r}, E; t)$ and a numerical approach is needed. Software packages such as *DRAGON* [107] and *GalProp* [108] are suitable. It will therefore become necessary to learn how to weight each term in a way that is both motivated on physical grounds and that is mathematically consistent. The contribution of diffusion and energy losses to the rate defined by eq. (4.30) is effectively weighted by comparing their respective time scales $t_{\rm loss}$, $t_{\rm diff.}$:

$$\frac{\partial n_E}{\partial t} \sim \frac{n_E}{t_{\rm diff}} + \frac{n_E}{t_{\rm loss}} + Q \ ,$$

where the time scale variables ($t_{\rm loss}$ and $t_{\rm diff}$) are usually estimated through a simple dimensional analysis, i. e. $t_{\rm loss} \simeq E/b$ and $t_{\rm diff} \simeq \sqrt{L/D}$ where L is the problem's typical length scale and it is usually determined by Q. As clearly apparent by the previous formula, the greater a time scale of a given process is, the less important its effect on the propagation will be. Therefore, to a big extent our analyses will be concerned with the estimation of the typical time scales of the different processes to which the particles are subject.

4.3.5 Analytical methods

We previously mentioned that the diffusion-loss equation can not be solved analytically for arbitrary diffusion coefficients and energy losses. However, if some conditions are imposed, analytical methods will work. We derive in this section general analytical solutions for those cases where it is possible.

As already mentioned, equation (4.30) is a linear inhomogeneous equation. If its homogeneous counterpart ($Q = 0$) is analytically solvable (and the solutions are known), then obtaining solution for (4.30) with general Q is straightforward. One only needs to construct a suitable Green's function and perform the corresponding integrations.

Let us assume that the diffusion coefficient and the energy loss function only depend on the particle's energy. By introducing the *Syrovatskii variables* λ and T [109] (see also excercise 14.2 in Sigl's textbook [70]) defined by

$$T = t - \tau \ , \text{ where } \ {\rm d}\tau = -\frac{{\rm d}E}{b(E)}$$
$$\text{and } \ {\rm d}\lambda = -\frac{D(E)\,{\rm d}E}{b(E)} \ ,$$

we can reduce the number of effective variables. To see this we multiply eq. (4.30) by $b(E)$ and introduce $f = b(E)n_E$. The equation then transforms to

$$\begin{aligned}
\frac{\partial f}{\partial t} - D(E)\boldsymbol{\nabla}^2 f - b(E)\frac{\partial f}{\partial E} &= b(E)Q(\boldsymbol{r}, E; t) \\
\frac{\partial T}{\partial t}\frac{\partial f}{\partial T} + \frac{\partial \lambda}{\partial t}\frac{\partial f}{\partial \lambda} - D(E)\boldsymbol{\nabla}^2 f - b(E)\left(\frac{\partial T}{\partial E}\frac{\partial f}{\partial T} + \frac{\partial \lambda}{\partial E}\frac{\partial f}{\partial \lambda} f\right) &= b(E)Q(\boldsymbol{r}, E; t) \\
\frac{\partial f}{\partial T} - D(E)\boldsymbol{\nabla}^2 f - b(E)\left(\frac{1}{b(E)}\frac{\partial f}{\partial T} - \frac{D(E)}{b(E)}\frac{\partial f}{\partial \lambda}\right) &= b(E)Q(\boldsymbol{r}, E; t) \\
-D(E)\boldsymbol{\nabla}^2 f + D(E)\frac{\partial f}{\partial \lambda} &= b(E)Q(\boldsymbol{r}, E; t) \ ,
\end{aligned}$$

or simply

$$\frac{\partial f}{\partial \lambda} - \boldsymbol{\nabla}^2 f = \tilde{Q}(\boldsymbol{r}, \lambda, T) \ , \tag{4.32}$$

where of course $\tilde{Q}(\boldsymbol{r}, \lambda, T) = b(E)Q(\boldsymbol{r}, E; t)/D(E)$. This expression has two special features. First, the T derivative dropped out and the number of effective variables is reduced and second, the equation is analogous to the familiar –analytically solvable– inhomogeneous heat equation.

The method just described is very general and has been applied to solve countless problems in cosmic-ray physics. However, in order to make a physical sense of the Syrovatskii variables it will be worthy to stick to the specific case where the particles

are electrons generated by DM annihilations. Under this assumption we integrate the defining equations for T and λ

$$T(t,E) = t - \int_E^{m_\chi} \frac{\mathrm{d}E'}{b(E')} \text{ and } \lambda(E) = \int_E^{m_\chi} \frac{D(E')\,\mathrm{d}E'}{b(E')} \ .$$

We observe that $t - T(= \tau)$ is essentially the time that it takes for an electron of initial energy m_χ to reach an energy E, while $\sqrt{\lambda}$ is the electron's root-mean-square displacement through diffusion during that time. The most general (physically interesting) solution can be constructed by means of the Green's function method:

$$f(\boldsymbol{r},\lambda,T) = \int \mathrm{d}T'\,\mathrm{d}\lambda'\,\mathrm{d}^3\,\boldsymbol{r'} G(\boldsymbol{r},\boldsymbol{r'},\lambda,\lambda',T,T')\tilde{Q}(\boldsymbol{r},\lambda) \ , \tag{4.33}$$

where $G(\boldsymbol{r},\boldsymbol{r'},\lambda,\lambda',T,T')$ satisfies

$$\frac{\partial G}{\partial \lambda} - \boldsymbol{\nabla}^2 G = \delta^3(\boldsymbol{r}-\boldsymbol{r'})\delta(\lambda-\lambda')\delta(T-T') \ . \tag{4.34}$$

The simplest solution of this equation reads

$$G(\boldsymbol{r},\boldsymbol{r'},\lambda,\lambda',T,T') = \frac{\Theta(\lambda-\lambda')}{[4\pi(\lambda-\lambda')]^{3/2}}\,\mathrm{e}^{\frac{\|\boldsymbol{r}-\boldsymbol{r'}\|^2}{4(\lambda-\lambda')}}\,\delta(T-T') \ , \tag{4.35}$$

excluding the Dirac delta function $\delta(T-T')$, this solution is usually refered to as the *heat kernel*. Actually, given that all solutions to (4.34) are proportional to $\delta(T-T')$ **and** that the injection functions under consideration are time independent, the general solution to (4.30) is stationary (independent of t) and given by

$$n_E(\boldsymbol{r}) = \frac{1}{b(E)} \int_E^{m_\chi} \mathrm{d}E' \int \mathrm{d}^3\,\boldsymbol{r'} G(\boldsymbol{r},\boldsymbol{r'},E,E')Q(\boldsymbol{r},E') \ , \tag{4.36}$$

where $G(\boldsymbol{r},\boldsymbol{r'},E,E')$ is defined through

$$G(\boldsymbol{r},\boldsymbol{r'},\lambda(E),\lambda'(E'),T,T') = G(\boldsymbol{r},\boldsymbol{r'},E,E')\delta(T-T') \ , \tag{4.37}$$

and we used the fact that $\mathrm{d}\lambda'\tilde{Q} = \mathrm{d}E'Q$ in arriving at eq. (4.36).

The Green's function $G_{\mathrm{HK}}(\boldsymbol{r},\boldsymbol{r'},E,E')$ –henceforth heat kernel– that results from our prescription (4.37) to the solution given by eq. (4.35) will be the key ingredient when constructing Green's functions that are suitable for the geometry of the problem. It is customary to impose Dirichlet conditions on the boundaries ($n_E|_{\text{bound.}} = 0$). Such conditions are physically interpreted and usually quoted as *free escape conditions* in the literature. The Dirichlet condition induces a spatial discontinuity in n_E at the boundaries and as a consequence the current density there: let z be a coordinate such that the boundary condition can be written as $z = \text{const.}$, then $-D\partial_z n_E|_{\text{bound}}$ becomes infinite[3].

As an example, the diffusion zone in our galaxy is approximately cylindrical and in cartesian coordinates the boundary conditions $n_E|_{z=\pm L/2} = 0$ are imposed, where L is the height of the baryonic matter halo. One can construct a Green's function that satisfies $G|_{z=\pm L/2} = 0$ by relying on a powerful tool from electrostatics: the *method of*

[3]The current density Φ_z is proportional to a Dirac delta centered at the boundary. For instance if the boundary is defined in cartesian coordinates by $z = L/2$, then $\Phi_z \simeq \varphi(x,y)\delta(z-L/2)$ close to $z = L/2$. $\varphi(x,y)$ is thus the number of particles that escape at point $(x,y,L/2)$ per unit surface.

images. Since our region of interest is constrained to $|z|$ and $|z'| < L/2$ we can add to the heat kernel (4.35) solution as many solutions to the homogeneous cousin of eq. (4.34) as we want. Particularly, we can (*i*) add solutions like (4.35) with shifted $|z'| > L/2$ so that it solves the homogeneous equation and (*ii*) choose $|z'|$ in such a clever way that the boundary conditions are satisfied. This is in essence how the method of images work. The shifted solution is called an "image solution" of the original one.

If the only condition to be satisfied is $G|_{z=L/2} = 0$ and our region of interest is $z < L/2$, then adding an image at $L - z'$ suffices:

$$G(\boldsymbol{r}, \boldsymbol{r'}, E, E') = G_{\rm HK}(\boldsymbol{r}, x', y', z', E, E') - G_{\rm HK}(\boldsymbol{r}, x', y', L - z' E, E')$$

solves (after following the prescription 4.37) eq. (4.34) and it moreover fulfills the boundary condition $G|_{z=L/2} = 0$. Solving for both boundaries requires an infinite ammount of images as the reader can easialy convice themself. The images should be located at $z'_n = nL + (-1)^n z'$ and the resulting Green's function reads [110]

$$G(\boldsymbol{r}, \boldsymbol{r'}, E, E') = \sum_{n=-\infty}^{\infty} (-1)^n G_{\rm HK}(\boldsymbol{r}, x', y', z'_n, E, E') \ . \tag{4.38}$$

Let us now implement the results from the previous and current sections in predicting the radio flux associated to DM annihilations.

4.4 Radio fluxes

In the previous two sections we characterized in quite some detail the radio emission of single electrons due to synchrotron radiation and their corresponding diffusive propagation in average regions of the galaxy. We shall now put these pieces together in obtaining a formula for the radio fluxes associated to DM-induced synchrotron-radiating electrons and positrons that arrive to Earth.

Electrons and positrons from DM annihilation are created in a random fashion where all directions are equally probable. With the definitions presented in the previous two sections the emissivity j_ν –i. e. emitted power per unit volume, per unit solid angle and per unit frequency– for DM-induced synchrotron radiation emitters is given by [21]

$$j_\nu(\boldsymbol{r}) = \frac{1}{4\pi} \int_{m_e}^{m_\chi} {\rm d}E 2 n_E(\boldsymbol{r}) \underbrace{\left(2\pi \frac{{\rm d}P_{\rm syn}}{{\rm d}\omega} \right)}_{({\rm d}P/\,{\rm d}\nu)_{\rm syn}} \ . \tag{4.39}$$

where the $1/4\pi$ factor takes into account the fact that at a given time the emitters are isotropically distributed and the factor 2 multiplying n_E ensures that both positrons and electrons are accounted for (assuming CP conserving annihilation). The differential radio flux I_ν for a small aperture angle subtending a solid angle $\Delta\Omega$ is then given by[21]

$$F_\nu = \int_{\Delta\Omega} {\rm d}\Omega \int_{\rm l.o.s.} {\rm d}s j_\nu(\boldsymbol{r}(s)) \ , \tag{4.40}$$

where, as usual, l.o.s. stands for *line of sight*. In the following we will encounter cases where the emission coefficient formally diverges; for instance, for a NFW profile j_ν will be a spherically symetric function with a pole at $r = 0$. In such cases, even though

the emissivity as the integrand in eq. (4.40) diverges, the integral defining I_ν converges since close to the pole $\mathrm{d}\Omega\,\mathrm{d}s = \mathrm{d}V/s^2 \simeq \mathrm{d}V/R^2_{\mathrm{source}}$ and therefore

$$F_\nu \simeq \frac{1}{R_{\mathrm{s}}^2}\int_{\mathrm{cone}} \mathrm{d}V\, j_\nu(\boldsymbol{r})\ . \tag{4.41}$$

In appendix B the general method to compute such half-cone integrals with spherical symmetry respect to the source is provided.

Recapitulating what has been discussed so far, the emission coefficient of synchrotron radiation indirectly produced by DM and given by eq. (4.39) can be analytically calculated once the space-independent energy loss and diffusion coefficients as well as the profile of the DM distribution, the mass of the DM, its annihilation rate and modes are given. All these variables enter in the computation of $n_E(\boldsymbol{r})$ (eq. 4.36) while on the other hand, the determination of the synchrotron power of single particles is quite precise if the uncertainties on the magnetic field are under control. Therefore, in most of the cases of interests, and as previously pointed out, using the monochromatic approximation and for instance neglecting absorption effects carry errors that are small compared to the aforementioned uncertainties.

In the following we will apply the machinery just presented to some specific cases with the aim of setting constraints on the DM model parameters.

4.4.1 Galactic Center

Radio observations of the galactic center (GC) provide, on the one hand, a window to the astrophysical phenomena occurring there in as much as the dust in the GC field of view becomes essentially transparent specially at low frequencies. On the other hand, the GC is a tremendously active region hosting a supermassive black hole (SMBH) driving most of its dynamics in the innermost regions. The impossibility of actually being able to see this region in the infrared to the optical range (because of the dust) is a rather limiting factor in characterizing it in more detail. In particular, very little is known about the magnetic field there and one must rely on theoretical estimates based on the accretion properties of the SMBH sitting there. Nonetheless, recent observations have provided evidence of strong fields in the vicinity of the GC [25] we shall make use of.

As just mentioned, even though our understanding of the magnetic field in the innermost regions of our galaxy is very limited, it seems reasonable [25] to assume that it is a strong one. Keeping in mind that the energy losses associated to energy-consuming processes other than synchrotron radiation are expected to be small, it will be reasonable to assume that most of the electron energy losses will be due to the latter. This assumption is mainly motivated by the hard power-law dependence on the magnetic field of the synchrotron loss function ($b_{\mathrm{syn.}} \propto B^2$). This is in contrast to the less harder dependence on, for instance, the gas and radiation densities of the energy loss function associated to the other processes.

Let us now concretely compare the typical time scales of energy loss and diffusion as defined in the previous section. If we take a Bohm diffusion coefficient then

$$t^{-1}_{\mathrm{loss}} = \frac{4B^2E^2/9m_e^2c^3}{E} \simeq (4\times10^{17}\,\mathrm{s})^{-1}\left(\frac{E}{0.01\,\mathrm{GeV}}\right)\left(\frac{B}{10\mu\mathrm{G}}\right)^2 \tag{4.42}$$

$$t^{-1}_{\mathrm{diff}} = \frac{Ec/3eB}{l^2} \simeq (3\times10^{17}\,\mathrm{s})^{-1}\left(\frac{E}{0.01\,\mathrm{GeV}}\right)\left(\frac{B}{10\mu\mathrm{G}}\right)^{-1}\left(\frac{l}{\mathrm{pc}}\right)^{-2}\ . \tag{4.43}$$

As a mnemonic aid notice that for $E = 0.01\,\mathrm{GeV}$, $B = 10\,\mu\mathrm{G}$ and $l = 1\,\mathrm{pc}$ both the typical loss and Bohm diffusion times are of the order of the age of the Universe. In

particular, the ratio of the two time scales does not depend on the particle energy and has a strong dependence on the magnetic field

$$\frac{t_{\rm loss}^{-1}}{t_{\rm diff}^{-1}} \simeq \left(\frac{B}{10\mu{\rm G}}\right)^3 \left(\frac{l}{\rm pc}\right)^{-2} \ , \tag{4.44}$$

where and extra factor of $D/D_{\rm Bohm}$ should be included if a different diffusion model should be considered.

The next step is to make a sense of l, namely the typical length scale of the problem. Neglecting for the moment any space dependence from the D and b functions in eq. (4.30), the only length scale in the problem is atributed to the source function or, equivalently to the DM distribution. Therefore, spatial variations in the electron density $n_E(r)$ will be only noticeable for length scales larger or of the order of $l(r) = -\rho^2(r)/[\rho^2(r)]' = -\rho(r)/2\rho'(r)$, where $\rho'(r) = {\rm d}\rho/\,{\rm d}r$ is assumed to be negative (ρ monotonically decreasing). For a generalized Navarro-Frenk-White (NFW) profile (eq. 3.7) $l_{\rm NFW}(r) \simeq r/2\gamma$ close to the center, while for an Einasto profile (5.21) the length scale is effectively the scale radius r_s: $l_{\rm Ein}(r) \simeq (r_s/2)(r/r_s)^{1-\alpha}$.

The recent discovery of a magnetar PSR J1745-2900 at only 0.12 pc away from the GC reported by reference [25] provides a handle on the magnetic properties of such a complex region. The authors were able to estimate the strength of the magnetic field by two different methods yielding in one case (simplistic calculation) a conservative limit of 50 μG. A more sophisticated method yields a lower limit of 8 mG. All these estimates are based on multi-wavelength analyses of the emission profile of the magnetar in the radio band.

Taking the conservative value for B at the magnetar position and the expressions just derived for the typical diffusion and loss time scales, we observe that for an NFW profile the ratio energy loss vs. diffusion is $t_{\rm loss}^{-1}/t_{\rm diff}^{-1} \simeq 5^3(.6)^{-2} \sim 350 \gg 1$, while in the case of an Einasto distribution $t_{\rm loss}^{-1}/t_{\rm diff}^{-1} \sim 580 \gg 1$. We may therefore safely assume that close to the GC electrons lose most of their energy with no effective diffusive displacement.

Turning back to the analytical method exposed before, by redefining the λ Syrovatskii variable in terms of a scaling parameter ϵ ($\lambda \to \epsilon\lambda$) the limit $\epsilon \to 0$ is equivalent to neglecting the diffusion term in eq. (4.30). One can show that in that limit $G_{\rm HK}(\boldsymbol{r}, \boldsymbol{r'}, E, E') \to \delta^3(\boldsymbol{r} - \boldsymbol{r'})$ and thus

$$n_E(\boldsymbol{r}) = \frac{1}{b(E)} \int_E^{m_\chi} {\rm d}E' Q(\boldsymbol{r}, E') = \frac{\langle\sigma v\rangle}{2m_\chi^2 b(E)} \rho_\chi^2(r) \underbrace{\sum_c {\rm BR}_c N_c(E)}_{N_e(E)} \ , \tag{4.45}$$

where $N_e(E)$ is the integrated yield of electrons or positrons with energies larger than E per annihilation. An explicit integration of eq. (4.30) in absense of the diffusion term shows that in the solution (4.45) we can actually promote the energy loss function b to a space dependent function. In particular, this condition allows us to extend the description of the DM-induced synchrotron radiation discussed so far to cases where the magnetic fields are space dependent.

4.4.1.1 Equipartition magnetic field at Sgr. A*

The presence of the SMBH at Sagitarius A* and its presumably very dynamic accretion can give rise to strong magnetic fields. The strength of these can be estimated through magnetohydrodynamical arguments [111–113]. Namely, assuming spherical accretion

of a collisionless pure Hydrogen plasma the speed of the particles is given by $v(r) = \sqrt{2GM_{\rm BH}/r}$, where $M_{\rm BH} \simeq 4.3 \times 10^6 M_\odot$ is the mass of the black hole (the Schwarzschild radius is $r_{\rm S} = 2GM_{\rm BH}/c^2 \simeq 4 \times 10^{-7}\,{\rm pc}$). Under these assumptions the distance at which the surrounding gas starts to accrete into the BH is $R_{\rm acc} \approx 0.04\,{\rm pc}$ [112]. The mass-loss rate of the BH due to accretion was estimated to be $|\dot{M}| \simeq 10^{-12} M_\odot/{\rm s}$ [111].

Integrating the continuity equation over a sphere of radius r allow us to relate the gas density with the mass-loss rate: $4\pi r^2 j(r) = 4\pi r^2 \rho_{\rm H}(r) v(r) = |\dot{M}|$. As a consequence the density scales like $r^{-3/2}$ with the radial distance to the center of the BH. After some fairly reasonable arguments pointed out in Ref. [111], inside the accretion region the magnetic energy density should be comparable (and thus share the radial dependence) with the kinetic energy of the fluid. Equating these two densities $\rho_{\rm H}(r)v^2(r)/2 = B^2/8\pi$ imply $B^2 = |\dot{M}| r_{\rm S}^{1/2} c / r^{5/2}$ ($B \propto r^{-5/4}$).

The equipartition assumption is only valid inside the accretion radius. In the outer regions the radial dependence is expected to follow the usual magnetic-flux conserving dependence $B \propto r^{-2}$. This ansatz for the magnetic field based on crude estimations has been of great use in the community. We will also use this model as our reference model whenever we investigate the synchrotron signal from DM at the GC. Specifically, we chose –as in Ref. [114]– a specific normalization and radius after which the average galactic magnetic field starts to become relevant:

$$B(r) = 7.2\,{\rm mG} \times \begin{cases} (R_{\rm acc}/r)^{5/4} & r < R_{\rm acc} \\ (R_{\rm acc}/r)^2 & R_{\rm acc} < r \lesssim 100 R_{\rm acc} \\ 10^{-4} & r \gtrsim 100 R_{\rm acc} \end{cases} . \tag{4.46}$$

Before discussing further the methodology of our radio analyses, we caution the reader that by implementing ansatz (4.46) we do not aspire to obtain predictions of high precision. For instance, notice that in its derivation nothing about the e. g. coherence length of the B-field is revealed. We will however be able to get an idea of the certainly large flux of DM-associated synchrotron emission at the GC.

4.4.1.2 Radio flux formula for the GC

In a few sections before, we mentioned that our no-diffusion solution (4.45) can be consistently made more general by including space dependence in the energy loss parameter b. Since we will neglect energy losses other than the synchrotron ones, we can safely use $b(r, E) = 4E^2 B^2(r)/9m_e^4 c^7$. Notice that the assumption of no diffusion implies that each electron effectively travels a distance that is small compared the typical length scale of the DM profile. Owing to the similarities in the spatial dependence (power-law like) of the DM profiles considered and our reference model (4.46) for the magnetic field, electrons and positrons barely experience the non uniform features of B and the whole formalism discussed above –based on the assumption of uniform magnetic fields– applies.

We will now make use the monochromatic approximation as most of the uncertainties will come from the unresolved magnetic field and to a bigger extent –as we shall see later– from the unsettled inner structure of the DM profile. Taking a randomly oriented magnetic field, the synchrotron emission power of an electron per unit frequency in this approximation reads

$$\frac{{\rm d}P_{\rm syn}}{{\rm d}\nu} = \frac{\sqrt{3}e^3 B}{m_e c^2} F_r\left(\frac{\nu}{\nu_c}\right) , \quad F_r(x) \approx \frac{16\pi}{27\sqrt{3}} \delta(x - 1/3) , \tag{4.47}$$

where $\nu_c = \omega_c/2\pi = 3eBE^2/4\pi m_e^3 c^5$. We can easily check that formula (4.17) is retrieved after integrating over all frequencies

$$b_{\rm syn}(r,E) = \int \frac{{\rm d}P_{\rm syn}}{{\rm d}\nu}\,{\rm d}\nu = \frac{4e^4B^2(r)E^2}{9m_e^4c^7}\ . \tag{4.48}$$

Note that ${\rm d}P_{\rm syn}/\,{\rm d}\nu$ can be also written as $(b_{\rm syn}/\nu_c)\delta(\nu/\nu_c - 1/3)$. We are now finally in position to write a formula that states how much synchrotron flux is indirectly produced by the annihilation of DM at the center of the galaxy. We start by evaluating the energy integral (4.39) leading to the emission coefficient

$$\begin{aligned} j_\nu &= \frac{1}{2\pi}\int {\rm d}E n_E(r)\frac{{\rm d}P_{\rm syn}}{{\rm d}\nu} = \frac{1}{2\pi}\int {\rm d}E n_E(r)\frac{b_{\rm syn}}{\nu_c}\delta\left(\frac{E_\nu^2(r)}{3E^2} - \frac{1}{3}\right) \\ &= \frac{1}{2\pi}\int {\rm d}E n_E(r)\frac{b_{\rm syn}}{\nu_c}\frac{\delta(E-E_\nu)}{|-2E_\nu^2/3E_\nu^3|} = \frac{1}{4\pi}\frac{b_{\rm syn}}{\nu}E_\nu n_{E_\nu}(r)\ . \end{aligned} \tag{4.49}$$

In the last step we defined $E_\nu(r) = \sqrt{4\pi m_e^3 c^5\nu/eB(r)}$ –the energy of an electron/positron synchrotron monochromatically radiating at the frequency ν– and used the fact that $\nu = \nu_{\rm syn}/3$. Substituting our expression (4.45) for $n_E(r)$ in (4.49) and plugging it into eq. (4.41) yields

$$F_\nu \simeq \frac{\langle\sigma v\rangle}{8\pi\nu R_\odot^2 M_\chi^2}\int_{\rm cone} {\rm d}V \rho_\chi^2(r)E_\nu(r)N_e[E_\nu(r)]\ . \tag{4.50}$$

This simple formula will be of great use in the subsequent chapters as it will allow us to set limits on the annihilation rate $\langle\sigma v\rangle$ after making some assumptions on the DM profile. In appendix B we show how to reduce the narrow observation-cone volume integral to a radial integral.

4.4.1.3 The 408 MHz bound on Sgr A*

In chapter 2 we showed the state-of-the-art measurements of the full electromagnetic spectrum of Sgr A* (figure 2.3). One of the key features of that spectrum was the fact that at radio frequencies the radiation intensity strongly decreases as the frequency becomes smaller. In particular, at the frequency of 408 MHz (wavelength of 73.5 cm) no observable signal has been so far detected as reported in reference [115]. This fact sets an upper limit of 50 mJy[4] (the interferometer sensitivity) on the differential flux. The inferred angular diameter of this signal $\theta_s \propto \lambda^2$ (λ being the wavelength) that results from the extrapolation of several measurements also carried out by the Jodrell Bank was found to be of $\sim 8''$. This corresponds to distances of ~ 0.17 pc from the center.

The large uncertainties in characterizing the galactic center radio emission (both from astrophysical sources and the DM component) make it formally impossible to perform spectral fits to the available measurements as in the case of gamma rays discussed in the previous chapter. These signals are however useful to constrain the DM annihilation cross section. We do this by comparing the flux that one obtains through formula (4.50) at a given frequency where no measurable flux has been reported (408 MHz turns out to be the optimal) and assume that the DM indirect signal is responsible for the *entire* flux.

[4] 1 Jy(Jansky)=10^{-26} erg/s/cm^2/Hz is a commonly used unit for differential spectral flux in the radioastronomy community.

Although there have been observational updates on the radio signal at Sgr A* –a positive signal of 0.4 Jy was claimed by the *Very Large Array* (VLA) Ref. [116] at the frequency 330 MHz (91 cm) with an inferred angular diameter of $\sim 12''$ ($r \sim 0.26$ pc)– the upper limit set by the Jodrell Bank at 408 MHz remains to be particularly special when constraining the DM cross section with synchrotron signals. Measurements at lower frequencies have larger angular diameters (λ^2 scaling) while the fluxes at higher frequencies are much too large compared to the typical DM-associated fluxes. Refs. [117, 118] used however a more robust measurement at that same frequency but within a larger angular region ($3\,^\circ$) to estimate the magnetic field strength on ~ 400 pc scales while Ref. [119] used it in the context of indirect DM searches.

The reader should however keep in mind that even though we, on the one hand, take the most conservative attitude by assuming no astrophysical background in modelling the 408 MHz signal, as including it would result in stronger limits. We, on the other hand by neglecting absorption in our derivation of formula (4.50), implicitly assumed that the radio signal cutoff at $\nu \lesssim 1$ GHz is not caused by the interaction of the radio wave with the interstellar medium through the so-called free-free absorption. This mechanism is the leading theory explaining the cutoff in the same way as interstellar scattering –which is also not considered in our formalism– is the accepted theory explaining the observed broadening of the angular diameter $\theta_s \propto \lambda^2$.

Chapter 5

Constraints on DM models

In this chapter we extend the theoretical ideas discussed in the previous chapters with the purpose of confronting them with actual astrophysical observations. In particular, we focus on the most recent indications of possible DM signals in the gamma-ray sky that we introduced and discussed in section 3.5, namely the *130 GeV line* and the *GeV excess*.

We shall first introduce a rather general formalism based on the QFT's optical theorem that relates measurable quantities describing different processes relevant for indirect DM searches. As we shall see, this formalism can be applied to constrain the DM model building of spectral gamma ray line signals and as a pratical application we employ it in the context of the 130 GeV feature.

In the last section we confront the DM interpretation of the GeV excess with updated antiproton, positron and radio-wave limits on the relevant DM annihilation cross sections. We discuss in detail the way such limits are obtained and point out ways to improve them.

5.1 The optical theorem

One of the central results in quantum scattering theory is the so-called optical theorem. This theorem basically states that the total cross section of a two-particle-system interaction is directly related to the imaginary part of the amplitude of forward scattering of the two particles[1] (see for instance Ref. [40]). In this section we will tend to be a bit more formal than in previous sections. We will however try to make as much as possible reference to the optical theorem's concrete applications on DM phenomenology. Let us start by noticing that its validity can actually be understood quite easily as it only assumes unitarity:

Let $|ab\rangle$ be an arbitrary two-particle initial state and $U = \mathbf{1}+iT$ the evolution operator of the system under consideration. Unitarity requires that $U^\dagger U = \mathbf{1}$, equivalently

$$i(T^\dagger - T) = T^\dagger T \;\Rightarrow\; 2\,\mathrm{Im}\langle ab|T|ab\rangle = \langle ab|T^\dagger T|ab\rangle \;. \tag{5.1}$$

In the last step we used the property $\mathcal{M}_{ab\to ab} \equiv \langle ab|T|ab\rangle = \langle ab|T^\dagger|ab\rangle^*$. In perturbation theory the quantity $\langle ab|T|ab\rangle$ is known as the scattering amplitude for forward scattering. While $\langle ab|T^\dagger T|ab\rangle = \||T|ab\rangle\|^2$ is simply the squared amplitude for any

[1] With forward scattering we of course mean that the final state is the same as the initial one, regardless of whether these are momentum eigenstates or not.

interaction. Translated to cross sections this means that

$$\sigma_{ab}^{\rm TOT} = \sum_{\rm states} \sigma_{ab\to \rm state} \propto {\rm Im}\mathcal{M}_{ab\to ab} \ , \tag{5.2}$$

where the proportionality constant depends on the normalization of $|ab\rangle$. We will not discuss the normalization details of the optical theorem here but we will instead introduce a more general version of it in the following.

5.1.1 Generalization

In the derivation we just performed, we focused on just diagonal matrix elements ($\langle ab|\mathcal{O}|ab\rangle$). If we consider more general matrix elements such as $\langle cd|\mathcal{O}|ab\rangle$, then the unitarity condition reads

$$-i\langle cd|T|ab\rangle + i\langle ab|T|cd\rangle^* = \langle cd|T^\dagger T|ab\rangle \ , \tag{5.3}$$

which at first sight does not look very informative. However, careful consideration of both sides of the equation will allow us to relate different physical observables.

Let us start with the left hand side of eq. (5.3) and consider states $|ab\rangle$ and $|cd\rangle$ satisfying $\langle cd|T|ab\rangle = \langle ab|T|cd\rangle$. We show in appendix C that this symmetry condition is precissely fulfilled by quantum two-particle states with definite angular momenta. In particular, non-relativistic s-wave DM pairs as the ones that we typically consider in the context of WIMP DM fall into this category. Under this assumption the left hand side of eq. (5.3) reduces to

$$-i\langle cd|T|ab\rangle + i\langle cd|T|ab\rangle^* = 2\,{\rm Im}\langle cd|T|ab\rangle \ .$$

The right hand side is a bit more intricate but still treateable, as we shall see. Let us start by considering a complete basis of what we will subsequently call *intermediate states* $\{|X\rangle\}$. We define the normalization of these states in such a way that

$$\sum_X |X\rangle\langle X| = \mathbf{1} \ .$$

Eq. (5.3) becomes

$${\rm Im}\langle cd|T|ab\rangle = \frac{1}{2}\sum_X \langle X|T|cd\rangle^*\langle X|T|ab\rangle \ . \tag{5.4}$$

By squaring both sides of the equation and identifying $\langle cd|T|ab\rangle = \mathcal{M}_{ab\to cd}$, $\langle X|T|ab\rangle = \mathcal{M}_{ab\to X}$ and $\langle X|T|cd\rangle = \mathcal{M}_{cd\to X}$, we obtain

$${\rm Im}[\mathcal{M}_{ab\to cd}]^2 = \frac{1}{4}\left|\sum_X \mathcal{M}^*_{ab\to X}\mathcal{M}_{cd\to X}\right|^2 \leq \frac{1}{4}\sum_X |\mathcal{M}_{ab\to X}|^2 \sum_Y |\mathcal{M}_{cd\to Y}|^2 \ , \tag{5.5}$$

where we used the Cauchy-Schwarz inequality in the last step. Expression (5.5) constraints the imaginary part of the amplitude relevant for the process $ab \to cd$ in terms of the product $\sigma_{ab}^{\rm TOT}\sigma_{cd}^{\rm TOT}$. Specifically,

$${\rm Im}[\sigma_{ab\to cd}] \leq \frac{\beta_{cd}^2 s}{64\pi^2}\sigma_{ab}^{\rm TOT}\sigma_{cd}^{\rm TOT} \ , \tag{5.6}$$

where β_{cd} is the center of mass (CoM) speed of the two-particle state $|cd\rangle$ and $\sqrt{s}$ its CoM energy. In addition we defined ${\rm Im}[\sigma_{ab\to cd}] \equiv ({\rm Im}[\mathcal{M}_{ab\to cd}]^2/|\mathcal{M}_{ab\to cd}|^2)\sigma_{ab\to cd}$ and assumed that both $|ab\rangle$ and $|cd\rangle$ are eigenstates of the total energy -see appendix C for details-. We shall in the next section comprehensively describe states with definite angular momentum.

5.1.2 Helicity eigenstates and partial waves

In QFT particle interactions are typically described in terms of asymptotic initial and final states, which are labeled by the 4-momenta and spin of each particle participating in the process. In this framework our initial state $|ab\rangle$ would be both eigenstate of type "a" and "b" particles' 4-momentum and spin component in some given direction as all those quantities commute with each other. Moreover, by virtue of Lorentz invariance of interactions described by QFT such 2-body states are completely labeled by the center of mass energy $E_{\mathrm{CoM}} = \sqrt{s}$, their individual spin in some given direction $\sigma_{a,b}$ and the directive angles of, say, type "a" particle's momentum (θ, ϕ): $|ab\rangle = |\sqrt{s}, \theta, \phi; \sigma_a, \sigma_b\rangle$.

In analogy to single particle states, we would be interested in decomposing states of the form $|\sqrt{s}, \theta, \phi; \sigma_a, \sigma_b\rangle$ in terms of angular momentum eigenstates. In order to do this, let first consider the operator algebra of the total angular momentum $J^{\alpha\beta}$ and the individual particle 4-momenta P_a^μ, P_b^μ

$$\begin{aligned} [J^{\alpha\beta}, J^{\gamma\delta}] &= i(\eta^{\alpha\gamma} J^{\beta\delta} - \eta^{\alpha\delta} J^{\beta\gamma} - \eta^{\beta\gamma} J^{\alpha\delta} + \eta^{\beta\delta} J^{\beta\gamma}) \quad , \\ [J^{\alpha\beta}, P^\mu_{a,b}] &= i(\eta^{\alpha\mu} P^\beta_{a,b} - \eta^{\beta\mu} P^\alpha_{a,b}) \quad . \end{aligned} \tag{5.7}$$

We introduce helicity opertors

$$\Lambda_{a,b} \equiv \frac{1}{P_{a,b}} \epsilon_{ijk} J^{ij} P^k_{a,b} \ , \tag{5.8}$$

where particle momenta $P_{a,b}$ are fully determined by the center of mass energy $P_a = P_b = [(s - (m_a + m_b)^2)(s - (m_a - m_b)^2)]^{1/2}/2\sqrt{s}$ ($m_{a,b}$ are the particle masses). In particular, commutation relations (5.7) imply that $J^2 = J_{ij}^2$ and, say, J^{12} together with P^0 and the particles' helicities $\Lambda_{a,b}$ form a complete set of commuting operators needed to fully describe states $|ab\rangle$.[2]

Ref. [120] discusses in a tremendously elegant way how such helicity states of the form $|J, M, \lambda_a, \lambda_b\rangle$ are constructed in terms of plane wave states, namely

$$|J, M, \lambda_a, \lambda_b\rangle = \sqrt{\frac{2J+1}{4\pi}} \int \mathrm{d}\Omega \, \mathrm{e}^{-i(M-\lambda)\phi} \, d^J_{M,\lambda}(\theta) |\theta, \phi, \lambda_a, \lambda_b\rangle \ , \tag{5.9}$$

where $\lambda \equiv \lambda_a - \lambda_b$.

5.1.2.1 Partial waves

In the same way by which we constructed the helicity basis, we can also construct a new basis where instead of the two helicity operators $\Lambda_{a,b}$ we consider instead Casimir operators L^2 and S^2. These operator can easily be constructed in the non-relativistic limit by decomposing the total angular momentum as $J^i = L^i + S^i$ and $S^i = S^i_a + S^i_b$, where $S_{a,b}$ are fundamental representations of the particles' spins. A fully relastivic construction of L and S is more involved. However, the change of base matrix is less intricated [120]

$$\langle J, M; L, S | J, M; \lambda_a, \lambda_b\rangle = \sqrt{\frac{2L+1}{2J+1}} C(LSJ; 0, \lambda) C(S_a S_b S; \lambda_a, -\lambda_b) \ , \tag{5.10}$$

[2]Such helicity states are perfectly covariant in the relativistic sense $\rightsquigarrow$ they are defined in the CoM frame. For 1-particle states helicity is of course frame-dependent

where $C(J_1 J_2 J, m_1, m_2)$ are Clebsch-Gordan coefficients. Both bases have the property that S-matrix elements are real provided that interactions respect time reversal symmetry as shown in appendix C and they are therefore suitable for application of formula (5.6). In the next section we will apply this formalism to a specific case, the case where $|ab\rangle = |\chi\chi\rangle$ and $|cd\rangle = |\gamma\gamma\rangle$ or $|\gamma Z\rangle$ or $|\gamma H\rangle$.

5.2 Model building constraints for gamma-ray lines

Equation (5.6) can be exploided in many ways. The applicability of it to processes relevant to indirect searches for DM is particularly interesting. In this section we will illustrate how we can set constraints on DM model building by combining information extracted from indirect DM dectection observations in several channels with known processes in the standard model.

The key element making formula (5.6) applicable to indirect DM detection physics is the fact that the partial wave basis is well suited to describe DM annihilations relevant for indirect DM detection. Namely, in the limit of vanishing speed the initial state is well described by an s-wave, i. e. a state with $L = 0$.

In this section we will apply the optical theorem to constrain the model building for gamma ray lines with DM, particular attention will of course be given to the 130 GeV feature introduced in chapter 3. Therefore, we make in formula (5.6) the identification $|ab\rangle = |\chi\chi\rangle$ and $|cd\rangle = |\gamma\gamma\rangle$ or $|\gamma Z\rangle$ or $|\gamma H\rangle$, where the initial state satisfies $L|\chi\chi\rangle = 0$. Moreover, we will for phenomenological reasons only consider those cases where the DM annihilation into benchmark channels ($b\bar{b}$, WW, etc.) occurs with branching ratios close to unity. In terms of our generalized version for the optical theorem, this means that we can just disregard the sum over $|X\rangle$ states in eq. (5.3), or more formally speaking, the sum will only run over the different quantum numbers describing $|X\rangle$. For instance, for DM that mainly annihilate into WW pairs, the condition

$$\mathrm{Im}[(\sigma v)_{\chi\chi\to\gamma Z}] \leq \frac{\beta_{\gamma Z}^2 m_\chi^2}{16\pi^2}(\sigma v)_{\chi\chi\to WW}\sigma_{\gamma Z\to WW} \tag{5.11}$$

allows to constrain the imaginary part of the amplitude describing the γ-ray line $\chi\chi \to \gamma Z$ by means of constraints on the process $\chi\chi \to WW$ which we obtain from indirect detection experiments. The way this method will be used is captured in figure 5.1 where the fact that a 1-loop process ($\chi\chi \to \gamma Z$) is related to two tree-level processes is apparent. In the next section we shall introduce the method we use to compute the cross sections describing the process $cd \to X$ and of course calculate them for several interesting choices of intermediate and final states.

5.2.1 Standard model cross sections

Here we shall rewrite the master formula (5.6) as

$$\frac{\mathrm{Im}[(\sigma v)_{\mathrm{line}}]}{(\sigma v)_{\mathrm{lead.}}} \leq \frac{\beta_{\mathrm{line}} s}{64\pi^2}\sigma_{\mathrm{line}\to\mathrm{lead.}}\ , \tag{5.12}$$

where the left hand side is constructed by physical quantities where the DM particle participates whereas the right hand side of the equation only depends on quantities that are independent of the model describing the DM particle. We compute in this section such terms by only using symmetry properties and the SM Lagrangian.

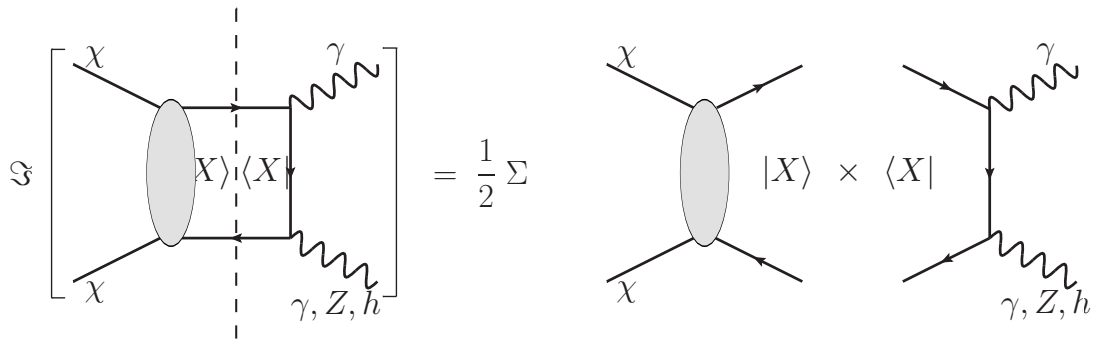

Figure 5.1: Diagram depicting the essence of our application of the generalized optical theorem.

As motivated before, the initial state $|\chi\chi\rangle$ will be assumed to be an s-wave. If the DM is a scalar particle the total angular momentum $J = L$ vanishes and there is only one possible s-wave state, namely $|\chi_{\text{sc.}}\chi_{\text{sc.}}\rangle = |J = 0, M = 0, L = 0, S = 0\rangle$ $(= |J = 0, M = 0, \lambda_a = 0, \lambda_b = 0\rangle)$. Note that we included the CP quantum number when labeling the state (see appendix C for a thorough discussion). This will become important when establishing selection rules for final and intermediate states. For Majorana DM particles, since they are their own antiparticle and they are fermions that satisfy Pauli's exclusion principle, there is only one possible s-wave state $|\chi_{\text{Maj.}}\chi_{\text{Maj.}}\rangle = |J = 0, M = 0, L = 0, S = 0\rangle$ $(= \frac{1}{\sqrt{2}}|J = 0, M = 0, \uparrow\uparrow\rangle - \frac{1}{\sqrt{2}}|J = 0, M = 0, \downarrow\downarrow\rangle)$. While for Dirac fermion DM, the state

$$\begin{aligned} |\bar{\chi}_{\text{Dir.}}\chi_{\text{Dir.}}\rangle^+ &= |J = 1, M = 0, L = 0, S = 1\rangle \\ &= \frac{1}{\sqrt{3}}|\uparrow\uparrow\rangle + \frac{1}{\sqrt{6}}|\uparrow\downarrow\rangle + \frac{1}{\sqrt{6}}|\downarrow\uparrow\rangle + \frac{1}{\sqrt{3}}|\downarrow\downarrow\rangle \end{aligned} \tag{5.13}$$

is also possible. We will however only focus here on scalar and Majorana DM while most of next chapter will be mainly concerned –in a rather different context, though– with vector DM.

5.2.1.1 Selection rules

Notice that for both initial states composed by scalar or Majorana DM pairs J vanishes and the only difference between them is their CP sign. Let us now use basic conservation laws so as to "predict" the possible outcomes from the annihilations in the partial wave basis.

Final states

First we notice that annihiliation into a γH state is forbiden[3] by angular momentum conservation. We therefore shall only consider $\gamma\gamma$ and γZ vector final states. Two spin-1 particle states with vanishing total angular momentum are spanned by three helicity eigenstates $|J = 0, M = 0, \lambda_1 = 1, \lambda_2 = 1\rangle$, $|J = 0, M = 0, \lambda_1 = 0, \lambda_2 = 0\rangle$ and $|J = 0, M = 0, \lambda_1 = -1, \lambda_2 = -1\rangle$ or, equivalently, by the three possible partial waves $|J = 0, M = 0, L = 0, S = 0\rangle$, $|J = 0, M = 0, L = 1, S = 1\rangle$ and $|J = 0, M = 0, L = -2, S = 2\rangle$ which are related by the following transformation rule

$$|L = 0,\ S = 0\rangle = \tfrac{1}{\sqrt{3}}|1, \lambda_2 = 1\rangle - \tfrac{1}{\sqrt{3}}|\lambda_1 = 0, \lambda_2 = 0\rangle + \tfrac{1}{\sqrt{3}}|\lambda_1 = -1, \lambda_2 = -1\rangle$$

[3]In realistic terms, such process is actually suppressed by the vanishingly small relative speeds.

$$|L=1,\ S=1\rangle = -\tfrac{1}{\sqrt{2}}|\lambda_1=1,\lambda_2=1\rangle + \tfrac{1}{\sqrt{2}}|\lambda_1=-1,\lambda_2=-1\rangle$$
$$|L=2,\ S=2\rangle = \tfrac{1}{\sqrt{6}}|\lambda_1=1,\lambda_2=1\rangle + \sqrt{\tfrac{2}{3}}|\lambda_1=0,\lambda_2=0\rangle + \tfrac{1}{\sqrt{6}}|\lambda_1=-1,\lambda_2=-1\rangle\,.$$

We omit henceforth the J and M labels which are assumed to vanish throughout. We now observe that states $|L=0,\ S=0\rangle$ and $|L=2,\ S=2\rangle$ contain zero helicity components and therefore, they can not be constructed neither with $\gamma\gamma$ or γZ quantum states. However, there is a linear combination of them which can be constructed. Namely,

$$|f_S\rangle = \sqrt{\frac{2}{3}}|L=0,\ S=0\rangle + \frac{1}{\sqrt{3}}|L=2,\ S=2\rangle = \frac{1}{\sqrt{2}}|\uparrow\uparrow\rangle + \frac{1}{\sqrt{2}}|\downarrow\downarrow\rangle\ . \tag{5.14}$$

This state is CP-even since $|L=0,\ S=0\rangle$ and $|L=2,\ S=2\rangle$ are also CP-even themselves. It is moreover the only allowed final 2-vector state in an annihilation of scalar DM particles. While the state $|f_M\rangle = |L=1,\ S=1\rangle$ is CP-odd and corresponds to the complementary case where DM particles are Majorana.

Intermediate states

Particles in $|X\rangle$ can either have spin 1/2 (quarks, charged leptons) or 1 (W bosons). In the former case, the only intermediate states with a non-vanishing matrix element $\langle X|T|f\rangle$ are

$$|X_S^{1/2}\rangle = |L=1,\ S=1\rangle = -\tfrac{1}{\sqrt{2}}|\uparrow\uparrow\rangle - \tfrac{1}{\sqrt{2}}|\downarrow\downarrow\rangle \quad , \tag{5.15}$$
$$|X_M^{1/2}\rangle = |L=0,\ S=0\rangle = \tfrac{1}{\sqrt{2}}|\uparrow\uparrow\rangle - \tfrac{1}{\sqrt{2}}|\downarrow\downarrow\rangle \quad ; \tag{5.16}$$

where we used the transformation rule defined in eq. (5.10) in deriving the coefficients multiplying the helicity eigenstates in a two spin 1/2 particle system.

Notice that for massless Dirac (Weyl) fermions, none of such states are realizable for a particle-antiparticle pair as the antiparticles in the Weyl representation have opposite helicities as their counterparts. Their states are spanned by $\{|\uparrow\downarrow\rangle, |\downarrow\uparrow\rangle\}$ and therefore $J=0$ is forbiden. If the fermions have instead a mass m_f that is small compared to the center of mass energy $\sqrt{s}$, the amplitude associated to the process $|\chi\chi(J=0)\rangle \to |\bar{f}f\rangle$ will be suppressed by a factor $m_f/\sqrt{s}$. These kind of processes are said to suffer from *helicity suppression*. Determining whether a process is helicity suppressed or not is rather straightforward and therefore helicity considerations serve as powerful cross-check tools for cross-section calculations.

For W bosons, however, selection rules do not constrain completely the space of possible outcomes with $|f_S\rangle$ as initial state, as it will do when $|f_M\rangle$ is the initial state. This reflects the fact that the subspace of two spin-1 particles with $J=M=0$ has dimension three (states with zero helicity play a role). Taking as a reference the selection rules that, in the previous discussion, enabled us to derive the final states, we conclude that $|X_M^1\rangle$ as there, is simply $|L=1,\ S=1\rangle$, while $|X_S^1\rangle$ is a linear combination of $|L=0,\ S=0\rangle$ and $|L=2,\ S=2\rangle$ or, equivalently, of transverse and longitudinal states

$$|t\rangle \equiv \frac{1}{\sqrt{2}}|\lambda_1=1,\ \lambda_2=1\rangle + \frac{1}{\sqrt{2}}|\lambda_1=-1,\ \lambda_2=-1\rangle \quad , \quad |l\rangle \equiv |\lambda_1=0,\ \lambda_2=0\rangle\ . \tag{5.17}$$

The coefficients occurring in such linear combinations will be obtained from the SM interaction and therefore carry interesting physical information.

5.2.1.2 Formulae

In appendix C a comprehensive explanation of the computation of the several cross sections needed is carried out. The method is simple in that we know a priori what the initial, final and intermediate states are. We write them in the helicity basis obtaining a sum of a handful of amplitudes which we compute using the Feynman rules choosing appropriately the polarization vectors. Tables 5.1 and 5.2 show the results of performing such calculations ($\beta_f = 1 - m_Z^2/4m_\chi^2$ and $\beta_X^2 = 1 - m_{f(W)}^2/m_\chi^2$).

Majorana DM	'final' state X (L,S)	$\frac{\Im(\sigma v)_{\gamma\gamma}}{(\sigma v)_{\rm tree}}$	$\frac{\Im(\sigma v)_{\gamma Z}}{(\sigma v)_{\rm tree}}$
$\chi\chi \to \bar{f}f$	$(0,0)$	$\frac{N_c Q^4 \alpha_{\rm em}^2 m_f^2}{2m_\chi^2} \frac{1}{\beta_X}\left[\tanh^{-1}\beta_X\right]^2$	$\frac{N_c Q^2 \alpha_{\rm em}\alpha m_f^2}{\cos^2\theta_W m_\chi^2}\left[\frac{T_3}{2} - Q\sin^2\theta_W\right]^2 \times$ $\times \frac{\beta_f}{\beta_X}\left[\tanh^{-1}\beta_X\right]^2$
$\chi\chi \to W^+W^-$	$(1,1)$	$2\alpha_{\rm em}^2 \beta_X \left[\tanh^{-1}\beta_X\right]^2$	$4\alpha_{\rm em}\alpha\cos^2\theta_W \beta_f \beta_X \left[\tanh^{-1}\beta_X\right]^2$

Table 5.1: Ratios of the (squared) imaginary part of the loop-suppressed gamma ray line amplitude to the total annihilation cross section for Majorana DM mainly annihilating into the channels displayed in the fist column. These formulas were obtained in appendix C by using eq. (5.12).

Scalar DM	'final' state X (L,S)	$\frac{\Im(\sigma v)_{\gamma\gamma}}{(\sigma v)_{\rm tree}}$	$\frac{\Im(\sigma v)_{\gamma Z}}{(\sigma v)_{\rm tree}}$
$\chi\chi \to \bar{f}f$	$(1,1)$	$\frac{N_c Q^4 \alpha_{\rm em}^2 m_f^2}{2m_\chi^2}\beta_X[\tanh^{-1}\beta_X]^2$	$\frac{N_c Q^2 \alpha_{\rm em}\alpha m_f^2}{\cos^2\theta_W \beta_f \beta_X m_\chi^2}\left[\frac{T_3}{2} - Q\sin^2\theta_W\right]^2 \times$ $\times\Bigg[\beta_X \tanh^{-1}\beta_X -$ $-(1-\beta_f)\left(\frac{\tanh^{-1}\beta_X}{\beta_X} - 1\right)\Bigg]^2$
$\chi\chi \to W^+W^-$	$\lvert t\rangle \equiv \sqrt{\frac{2}{3}}\lvert 0,0\rangle$ $+\frac{1}{\sqrt{3}}\lvert 2,2\rangle$	$\alpha_{\rm em}^2 \frac{\left(1+\beta_X^2\right)^2}{2\beta_X}[\tanh^{-1}\beta_X]^2$	$\frac{\alpha_{\rm em}\alpha\cos^2\theta_W}{\beta_X\beta_f}\Bigg[(\beta_f^2+\beta_X^2)\tanh^{-1}\beta_X$ $+\frac{(\beta_f-\beta_X^2)}{\beta_X}(1-\beta_f)\left(\frac{\tanh^{-1}\beta_X}{\beta_X}-1\right)\Bigg]^2$
	$\lvert l\rangle \equiv \sqrt{\frac{2}{3}}\lvert 2,2\rangle$ $-\frac{1}{\sqrt{3}}\lvert 0,0\rangle$	$\alpha_{\rm em}^2 \frac{\left(1-\beta_X^2\right)^2}{4\beta_X}[\tanh^{-1}\beta_X]^2$	$\frac{\alpha_{\rm em}\alpha\cos^2\theta_W}{2\beta_X\beta_f}\frac{m_W^4}{m_\chi^4}\Bigg[\left(1-\frac{m_Z^2}{4m_W^2} - \frac{m_Z^4\beta_X^2}{8m_W^4}\right)\tanh^{-1}\beta_X - \frac{m_Z^2}{4\beta_X m_W^2}\times$ $\times\left(2-\beta_X^2-\frac{m_Z^2}{2m_W^2}\right)\left(\frac{\tanh^{-1}\beta_X}{\beta_X}-1\right)\Bigg]^2$

Table 5.2: Same as Tab. 5.1, but for scalar DM. In the case that $|X\rangle$ is a W-pair, we report our results in the $\{|t\rangle, |l\rangle\}$ basis.

WW intermediate state

The total amplitude for the processes $\gamma\gamma \to WW$ or $\gamma Z \to WW$ can be computed using any basis. Actually, the fact that

$$|\langle X_S^1|T|f_S\rangle|^2 = |\langle L=0,S=0|T|f_S\rangle|^2 + |\langle L=2,S=2|T|f_S\rangle|^2 = |\langle t|T|f_S\rangle|^2 + |\langle l|T|f_S\rangle|^2 \,,$$

serves as a cross-check of our calculations. In the case of $\gamma\gamma \to WW$ total amplitude reads

$$\langle X_S^1|T|f_S\rangle = 16\pi\sqrt{4\beta_X^2 + \frac{3}{2}\gamma_X^{-4}}\frac{\tanh^{-1}\beta_X}{\beta_X} \,, \tag{5.18}$$

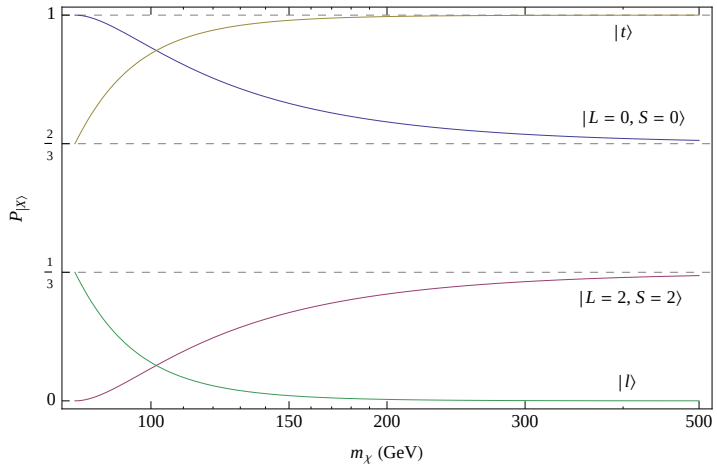

Figure 5.2: Relative contribution from partial waves, transverse and longitudinal internal components to $\langle WW|T|\gamma\gamma\rangle$ as a function of the mass of the DM particle.

where the state $|X_S^1\rangle$ can be represented in both basis as

$$|X_S^1\rangle = \frac{1}{\sqrt{3}}\frac{3+\beta_X^2}{\sqrt{8\beta_X^2+3\gamma_X^{-4}}}|L=0,S=0\rangle + \sqrt{\frac{2}{3}}\frac{2\beta_X^2}{\sqrt{8\beta_X^2+3\gamma_X^{-4}}}|L=2,S=2\rangle \tag{5.19}$$

$$= \frac{\sqrt{2}(1+\beta_X^2)}{\sqrt{8\beta_X^2+3\gamma_X^{-4}}}|t\rangle - \frac{1}{\gamma_X^2\sqrt{8\beta_X^2+3\gamma_X^{-4}}}|l\rangle \ . \tag{5.20}$$

Fig. 5.2 shows how the different components of $|X_S^1\rangle$ are distributed as a function of the mass of the DM particle. Notice that according to our assumptions $\gamma_X = m_\chi/m_W$ and therefore, $\beta_X = \sqrt{1-(m_W/m_\chi)^2}$.

As expected, at small β_X ($m_\chi \approx m_W$), the state is dominated by $|L=0,S=0\rangle$, whereas in the ultrarelativistic limit, it is the transverse component $|t\rangle$ the one that dominates. The asymptotic values 1/3 and 2/3 reflect the fact that

$$|t\rangle = \sqrt{\frac{2}{3}}|L=0,\ S=0\rangle + \frac{1}{\sqrt{3}}|L=2,\ S=2\rangle \text{ and } |L=0,S=0\rangle = \sqrt{\frac{2}{3}}|t\rangle - \frac{1}{\sqrt{3}}|l\rangle \ .$$

We notice that the shown computations agree with previous studies [121] and by including the γZ final state, we extend them. The case where the DM particle is scalar and the loop amplitude is dominated by W running on the loop, was studied just in the limiting cases where $m_\chi \approx m_W$ ($\beta_X \to 0$) and when $m_\chi \gg m_W$ ($\beta_X \to 1$). Here we obtained a formula that is valid for all DM masses and of course reaches asymptotically the values already reported in Ref. [121], as easily verified by exploiting the properties of $\tanh^{-1}\beta_X$:

- **Low energy limit:** at first order in β_X we can take $m_\chi = m_W$ and $\tanh^{-1}\beta_X \approx \beta_X$. Therefore,

$$\frac{\mathrm{Im}[\sigma v]_{\gamma\gamma}}{(\sigma v)_{WW}} = \frac{3e^4\beta_X}{64\pi^2} \ .$$

- **High energy limit:** in this case we can neglect all m_W/m_χ rational terms and take $\beta_X = 1$ everywhere but in $\tanh^{-1}\beta_X$. We treat this function in its alternative definition ($\frac{1}{2}\ln[(1+\beta_X)/(1-\beta_X)]$) and expand β_X as $1 - \frac{1}{2}(m_W/m_\chi)^2$, which implies $(1+\beta_X)/(1-\beta_X) \approx 4m_\chi^2/m_W^2$ and therefore

$$\frac{\mathrm{Im}[\sigma v]_{\gamma\gamma}}{(\sigma v)_{WW}} = \frac{e^4}{32\pi^2}\left[\log\left(\frac{4m_\chi^2}{m_W^2}\right)\right]^2 \ .$$

5.3 Application: The 130 GeV line

After analytically computing the several cross sections that we tabulated in table 5.1, the missing ingredients for formulas like (5.11) to be applicable, are the constraints on leading annihilation rates from indirect detection experiments (e. g. $(\sigma v)_{\chi\chi\to WW}$ in eq. (5.11). In this section we adapt, in a channel-by-channel the general methods outlined in chapters 2-4 to the 130 GeV case so as on the one hand to obtain general limits on such annihilation cross sections, while on the other hand to constrain the imaginary part of the amplitude associated to the 130 GeV line by means of the optical theorem. Consistently with Ref. [15] we shall asume the galactic halo to have a DM density given by an Einasto profile

$$\rho_{130\mathrm{GeVline}}(r) = \rho_0 \exp\left(-\frac{2}{\alpha}\frac{r^\alpha}{r_s^\alpha}\right) \ , \tag{5.21}$$

with $\alpha = 0.17$, $r_s = 20\,\mathrm{kpc}$ and $\rho_0 = 1.05\,\mathrm{GeV/cm^3}$ which results from $\rho(r = 8.5\,\mathrm{kpc}) = 0.4\,\mathrm{GeV/cm^3}$. The mass of the WIMP explaining the line is given by $m_\chi = 130\,\mathrm{GeV}[1 + \sqrt{1 + (m_X/130\,\mathrm{GeV})^2}]/2$, where $m_X = 0, m_Z$ or m_H depending on the interpretation (model).

general WIMP	cont. gamma (dwarfs)	cont. gamma (GC)	antiprotons (KRA)	antiprotons (CON)	synchrotron (full cone)	synchrotron ($r < 1\,\mathrm{pc}$)
$b\bar{b}$	7.6 (8.1, 8.6)	21 (22, 23)	10.4 (11.6, 11.5)	4.2 (4.7, 4.7)	27.5 (29.6, 31.2)	89 (101, 110)
$\tau^+\tau^-$	16 (18, 20)	14 (15, 16)	—	—	25.8 (29.6, 32.7)	369 (441, 500)
$\mu^+\mu^-$	145 (168, 190)	28 (28, 29)	—	—	18.2 (21.8, 24.7)	427 (515, 589)
e^+e^-	89 (104, 118)	14 (11, 13)	—	—	16.1 (19.4, 22.2)	419 (506, 579)
W^+W^-	11 (12, 12)	24 (24, 26)	9.3 (9.5, 9.8)	3.8 (3.9, 4.0)	29.7 (32.5, 34.7)	122 (139, 152)

Table 5.3: Limits on the WIMP annihilation rates (in units of $10^{-26}\mathrm{cm^3 s^{-1}}$) for DM models explaining the 130 GeV line.

5.3.1 Continuum gamma rays

In chapter 3 we explained in some detail how we can in a model-independent way search for DM by analyzing the gamma-ray spectra of targets where we believe the DM signal can be important. Here, we make a concrete use of them by e. g. setting a definite value for the mass of the DM and selecting specific targets.

In Ref. [122] the Fermi-LAT collaboration investigated a catalogue of dwarf spheroidal galaxies in the context of indirect searches for DM. We consider the bounds on the annihilation rates of DM pairs that they obtained and evaluate them at the DM masses required for the 130 GeV excess to be interpreted of DM origin. These values are shown in Table 5.3. Even though Fermi-LAT did not report any limits on annihilation rates where the DM particles mainly annihilate into an electron/positron pair, we make an educated guess by rescaling the limits on DMDM$\to \mu^-\mu^+$ with the appropriate number of photons produced per annihilation $N_\gamma = \int_{m_e}^{m_{\mathrm{DM}}} \frac{\mathrm{d}N}{\mathrm{d}E}\,\mathrm{d}E$.

Model	L(kpc)	δ	$D_0(10^{28}\mathrm{cm}^2/\mathrm{s})$	v_A(km/s)	γ	$\mathrm{d}v_c/\,\mathrm{d}z$(km/s/kpc)	Φ (GV)
KRA	4	0.50	2.64	14.2	2.35	0	0.67
CON	10	0.6	0.97	38.1	1.62/2.35	50	0.21

Table 5.4: Parameters of the CR propagation models used in our reference model [29]

A central assumption in the analysis of Ref. [122] was that the DM halo for each dwarf galaxy follows an NFW profile. This certainly renders the limits stronger than had we taken a shallower profiles like (5.21). In order to also present a conservative angle, we complement Table 5.3 with another set of continuum gamma-ray limits from Ref. [123], where the galactic center is targetted. In that work the authors also make use of a different profile than eq. (5.21) but owing to the property that the DM-induced gamma-ray flux can be expressed as the product of an astrophysical J-term and a term containing the particle physics information, we rescale their limits by the correct J-factor.

As a final comment, notice that the latter constraints on light leptonic channels are stronger than the ones encountered in the former. This is because Ref. [123] included the effects of inverse Compton scattering in their analysis as the amount of radiation density around the GC is huge.

5.3.2 Antiprotons

DM annihilation into hadronic channels (for instance $\bar{b}b$) are better constrained by antiproton data. In our analysis we consider the two reference set of parameters "KRA" and "CON" introduced in Ref. [29] –see Table 5.4–. They respectively provide the weakest and the strongest constraints on σv for a DM mass consistent with the 130 GeV-line interpretation.

The resulting limits on the annihilation rates of DM pairs into $\bar{b}b$ and WW are also reported in Table 5.3. The dataset that the authors of Ref. [29] used, was the one reported by the PAMELA collaboration in Ref. [73] and the criterion to set such limits was demanding that the minimally expected astrophysical background of secondary antiprotons –as extracted from Ref. [30]– plus the DM signal –computed by using DarkSUSY[68]– do not overshoot the PAMELA antiproton measurements.

Although it is not apparent in Table 5.3, our antiproton limits are only mildly sensitive to solar modulation (Φ parameter in Table 5.4) and to convection (parametrized by $\mathrm{d}v_c/\,\mathrm{d}z$) since the antiproton kinetic energies that are relevant to this particular analysis lie in the $\sim 7-26\,\mathrm{GeV}$ region.

5.3.3 Radio

In table 5.3 we also report radio limits based on the 408 MHz measurement discussed in section 4.4.1. As customarily done, we assumed no background and magnetic equipartition –eq. (4.46)– when modelling the DM-induced synchrotron flux. We also assumed that the synchrotron emission of a single electron (positron) is monochromatic, in such a way that we could use formula (4.50):

$$F_\nu \equiv \frac{1}{4\pi R_\odot^2}\frac{\mathrm{d}W_{\mathrm{syn.}}}{\mathrm{d}\nu} \approx \frac{(\sigma v)}{8\pi\nu R_\odot^2 M_\chi^2}\int E_p \rho_\chi^2(r) N_e(E_p)\,\mathrm{d}V \ , \tag{5.22}$$

where we used DarkSUSYto obtain $N(E)$ numerically.

The integration region is defined as the intersection of a cone of half-apperture $4''$, associated to the 408 MHz measurement and a sphere of 1 pc centered at the GC inside

which, neglecting diffusion effects is valid. The 1 pc estimate of such "validity sphere" was obtained by means of eq. (4.44), where the typical length scale l is $(r_s/2)(r/r_s)^{1-\alpha}$ for an Einasto profile (5.21). By plugging the "equipartition" magnetic field ansatz defined by (4.46) into eq. (4.44) we obtain the desired estimate

$$\frac{t_{\rm loss}^{-1}}{t_{\rm diff}^{-1}} \simeq 3 \left(\frac{r}{\rm pc}\right)^{-4-2\alpha} , \tag{5.23}$$

In Sec. 5.4.3 we comprehensively revisit and scrutinize the method just considered. In particular, we notice that even qualitative modifications of the magnetic field's profile lead to little changes in the results shown in Table 5.3.

In table 5.3 we also include the "full-cone" radio bounds on the annihilation rates. These are obtained by using eq. (5.22) but by integrating over the full cone. Such a practice is customary in the literature: see e. g. Refs. [114, 119].

Finally, assuming that the 130 GeV gamma-ray feature is caused by Majorana DM annihilation[4], we report in table 5.5 our (model-building) constraints on the imaginary part of the $\chi\chi \to \gamma\gamma$ (γZ) amplitudes. They are obtained by using formulas and indirect detection constraints like the ones tabulated in 5.1 and 5.3 respectively. In the next section we will make sense of such constraints by comparing them to some families of models that could explain the 130 GeV line as DM.

Majorana WIMP	cont. gamma *limit* (GC)	antiproton *limit* ('KRA', $L = 4$ kpc)	synchrotron *limit* (full cone)
$b\bar{b}$	1.0×10^{-5} (3.1×10^{-6})	5.1×10^{-6} (1.6×10^{-6})	1.4×10^{-5} (4.2×10^{-6})
$\tau^+\tau^-$	4.9×10^{-5} (2.0×10^{-7})	—	9.1×10^{-5} (4.0×10^{-7})
$\mu^+\mu^-$	8.7×10^{-7} (3.3×10^{-9})	—	5.7×10^{-7} (2.6×10^{-9})
e^+e^-	2.9×10^{-11} (8.7×10^{-14})	—	3.3×10^{-11} (1.5×10^{-13})
W^+W^-	0.037 (0.21)	0.014 (0.083)	0.046 (0.28)

Table 5.5: Constraints on the ratio of the imaginary part of the squared $\chi\chi \to \gamma\gamma$ (γZ) amplitude to the total annihilation rate of Majorana DM particles into $\gamma\gamma$ (γZ) in the DM interpretation of the 130 GeV line.

5.3.4 Discussion

The resulting limits displayed in table 5.5 are apparently rather stringent. Particularly constrained are the models which fermionic loops dominate the line's amplitude. This is due to the helicity suppression in the SM processes $\gamma X \to \bar{f} f$ and $\gamma X \to W_t W_t$ that are relevant for the optical theorem.

To get a feeling of what our limits mean, we performed a scan over the parameter space of the constrained MSSM and a 7-parameter phenomenological variation: the constrained MSSM. As briefly discussed in Sec. 1.3 such models can offer a suitable WIMP candidate: the lightest supersymmetric neutralino which is constructed by the superpartners of the gauge bosons and the two physical Higgs bosons apparent in the MSSM.

Fig. 5.3 displays the resulting imaginary part relative contributions to the total gamma-ray-line amplitudes for such a scan. The color code indicates how large the coefficients in eq. (1.7) are. More specifically, the neutralino is mostly Bino if $Z_{\tilde{B}} \equiv |N_{11}|^2 > 0.9$), Higgsino if $Z_{\tilde{H}} \equiv |N_{13}|^2 + |N_{14}|^2 > 0.9$. We indicate whether thermal production leads to the correct relic density by shape coding.

[4]The corresponding constraints for scalar DM were also obtained in Ref. [III]

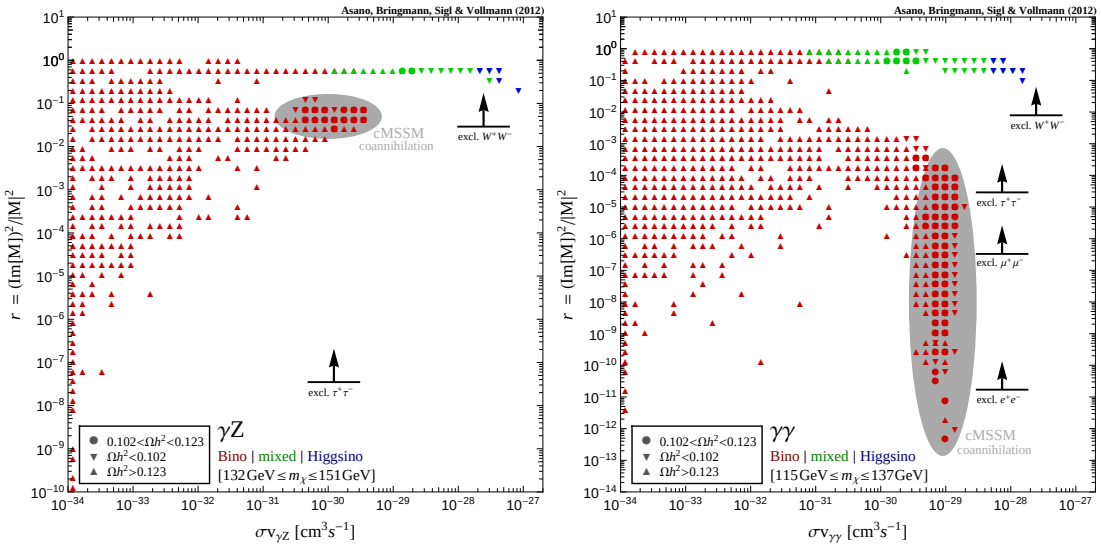

Figure 5.3: Left: scan over MSSM and cMSSM models by which neutralino annihilation into a γZ state gives rise to a gamma-ray line. In the figure we compare the total annihilation rate vs. the squared imaginary part of the amplitude of the $\chi\chi\gamma Z$ process. Models where the neutralino is dominantly a Higgsino (Bino) are indicated by blue (red) symbols; green symbols refer to mixed neutralino DM. Models indicated with circles reproduce the correct DM density today, while upper (lower) triangles indicate larger (smaller) relic densities. Models inside the shaded area are discussed in the text. We also include some of the most relevant limits from Tab. 5.5. Right: Same, for neutralino annihilation into $\gamma\gamma$.

Note first that in the scan models reproducing the correct DM density at the present time are unable to attain the rather large cross section associated to the 130 GeV line, namely $\langle\sigma v\rangle_{\gamma\gamma} \sim 1.27 \times 10^{-27}\,\mathrm{cm}^3/\mathrm{s}$ ($\langle\sigma v\rangle_{\gamma Z} \sim 3.14 \times 10^{-27}\,\mathrm{cm}^3/\mathrm{s}$). Second, the imaginary parts of the loop amplitude for models with large line cross sections are always sizeable compared with the limits we obtained. The only exceptions are found in the so-called co-annihilation regime for annihilation into two photons (shaded area in fig. 5.3) [124]. There, the neutralino is almost a pure Bino (red coloured in fig. 5.3) and its mass is just slightly different than the light $\tilde{\tau}$-slepton.

The loop amplitude for models in this coannihilation regime is roughly the sum of the two Feynman diagrams shown in figure 5.4 [22], where only the first one participates in the optical theorem's decomposition illustrated in figure 5.1 while the second does not have an imaginary part. Owing to the aforementioned mass degeneracy, diagram (b) gets strongly enhanced[5] and the imaginary part of the amplitude gets suppressed as apparent in the left panel of figure 5.3.

Our results therefore severely challenge the model-building associated to the line interpretation of the 130 GeV excess, allowing only models with properties that tend to be too peculiar: accidental cancelations, mass degeneracies.

Such challenges would then favour the original [16] interpretation of the excess as consequence of *internal bremmstrahlung* in DM annihilations into fermionic pairs. Notice that this holds even in the case that we just discussed where IB process is enhanced in exactly the same way as diagram (b) in fig. 5.4 got enhanced by virtue of mass degeneracies between $\tilde{\tau}$ and $\tilde{\chi}^0 \approx \tilde{B}$.

[5]The topology of diagram (b) as most of its properties are similar to the VIB diagrams discussed in chapter 3.

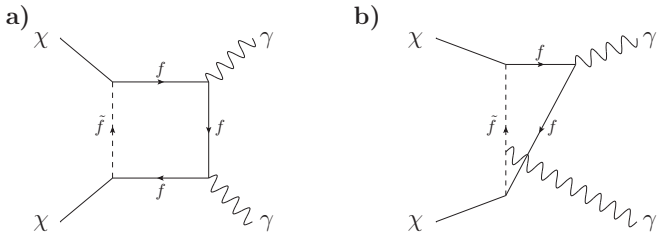

Figure 5.4: Leading diagrams in neutrino annihilation into monochromatic photons [22]. Diagram (*b*) completely dominates the process for almost degenerate sfermions $\tilde{f}$ and Bino-like neutralinos χ.

5.4 Constraints on the GeV excess

In this part we turn our attention to a different, if somehow related, problem. In the previous part we were primarily interested in constraining DM models that could accommodate for a gamma-ray line at the energy of 130 GeV through consideration of the imaginary part associated to such process. Here, the strategy will be quite different. We will instead make some sort of "consistency check" where we confront the claim of the gamma-ray GeV *excess* with the information provided by complementary observation channels. In particular, we consider antiprotons, positrons and radio waves.

In section 3.5 we discuss in quite some detail what the main features of the GeV excess are. Just to briefly recapitulate, a recent analysis [24] of the FERMI-LAT [125] data revealed the existence of an apparent signal around the GC that can not be accommodated within the astrophysical models adopted there. The spatial morphology and energy spectrum of such an excess can then in principle be explained in terms of thermally produced WIMPs with masses 10–40 GeV annihilating in the galactic DM halo.

If such a claim is true, then complementary signals in other *indirect detection* channels are expected[6]. Before discussing this in a channel-by-channel basis, let us first make some considerations on the general assumptions that we can make when confronting the excess hypothesis with other indirect detection channels.

In the same way that the DM interpretation of the 130 GeV excess fixes several parameters of the theory, for instance, along our discussion of the 130 GeV line we assumed a given set of DM masses and an Einasto profile (5.21). Analogously, according to the original publication[7], the DM interpretation of the GeV excess requires that the DM profile should have a standard cuspy feature $\rho \propto r^{-\gamma}$ ($\gamma \approx 1.04 - 1.24$) for $r \lesssim 1\,\mathrm{kpc}$. We use this information as an input for our theoretical models of the cosmic-ray antiproton, positron and synchrotron fluxes discussed in the previous chapters. By regarding the annihilation rate as a free parameter (and the mass in our positron study) we then obtain constraints that can immediately be confronted to the DM interpretation of the GeV excess.

[6] In principle, also related signals in direct and collider experiments could be observed. The likeliness of such complementary detections is however highly model dependent.

[7] As mentioned in chapter 3, a newer version improved their analysis and included updated best-fit values for γ.

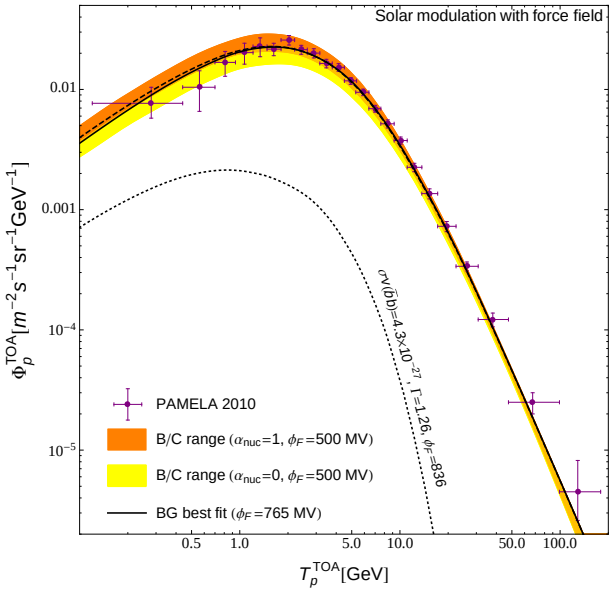

Figure 5.5: PAMELA antiproton flux measurements [23] as a function of their kinetic energy. The solid line is the best-fit model (with no DM) while the yellow and orange bands indicate the allowed predictions that are consistent with the B/C propagation model for the extreme values of the parameter $\alpha_{\rm nuc}$. The dotted and dashed lines show the contribution of a DM component.

5.4.1 Antiprotons

Following the directions given in section 2.3.2 and applied in the previous sections, we make a likelihood ratio test to obtain for each DM mass the maximally allowed annihilation rate that is compatible with the PAMELA dataset reported in Ref. [23]. This is a slightly different dataset than the one considered in the previous section [73]. It features a larger measurement span between June 2006 and January 2010.

There are, however, two main qualitative differences between this analysis and the one we performed in the above section. Since the DM masses at play in this case are one order of magnitude smaller than the ones considered there and therefore comparable to the proton mass $\sim 1\,\mathrm{GeV}$, the biggest sources of uncertainties in the antiproton analysis discussed in Sec. 2.3.2 such as solar modulation and non perturbative QCD come into play.

We take these effects into account and consider additionally statistical uncertainties in the B/C propagation model. All this by introducing three free parameters ϕ_F, $\alpha_{\rm prop.}$ and $\alpha_{\rm nuc.}$. The first one is the Fisk potential introduced in chapter 2, while the other two are defined in such a way that the linearly interpolate between the minimal and maximal predictions of Ref. [30] for the secondary flux associated to propagation and nuclear uncertainties [69] respectively.

As done in the previous section, we adopt the reference model "KRA" featured in Ref. [29] and defined by the parameters shown in Table 5.4. Fig. 5.5 shows the 3-parameter background (BG) fit to the (updated) PAMELA dataset [23]. The results of adding a DM component to the fit and performing a four-parameter likelihood test are shown in Fig. 5.6, where our exclusion criterion was varying the parameters (increasing σv) until the best-fit value $-2\ln\mathcal{L}$ changed by 2.71.

Although reference model *KRA* is the more realistic as far as constraints from differ-

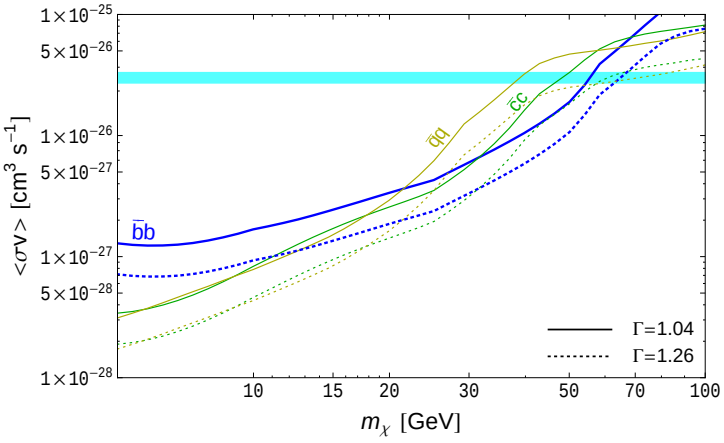

Figure 5.6: Updated antiproton constraints on the annihilation rate of DM into quark final states from PAMELA data [23] assuming a generalized profile of –eq. (3.7)– with $\Gamma = 1.04$ (solid lines) and $\Gamma = 1.26$ (dotted lines).

case	δ	D_0 (kpc^2/Myr)	L (kpc)	V_c (km/sec)	V_a (km/sec)
MAX	0.46	0.0765	15	5	117.6
MIN	0.85	0.0016	1	13.5	22.4
MIN′	0.85	0.0032	2	13.5	22.4

Table 5.6: Antiproton propagation parameters compatible with B/C analysis [30].

ent astrophysical observations on propagation parameters are concerned –see Sec. 2.3.2 for details–, in order to get a broader picture we also considered further propagation parameter sets compatible with the B/C analysis. Particularly, we studied the extreme cases *MAX* and *MIN'* parametrized in Table 5.6. Parameter sets *MAX* and *MIN* had been introduced in 2003's Ref. [126] while the model *MIN'* is an educated variation of the rather outdated *MIN* model that is both consistent with current constraints on the diffusion's zone height L and with the B/C analysis.

Fig. 5.7 shows how the constraints of DM annihilations into b-quark pairs featured in Fig. 5.6 can change by varying the reference propagation model in a reduced –but interesting in terms of the GeV excess– mass interval.

5.4.2 Positrons

As mentioned earlier, the method by which we confront the DM interpretation of the GeV excess with positron data is different than the one we have just applied in the case of antiprotons. Namely, for a given set of branching ratios into leptonic states and $\bar{b}b$, we refit –when sensible– the energy spectrum from Ref. [24]'s fig. 3.8 with the mass and the annihilation rate of the DM as fitting variables. We then compare the resulting rates with the central values of the AMS-02 positron constraints on DM by [10] displayed in fig. 2.5 and discussed in section 2.3.2.

The reason why we mainly consider DM annihilation into leptons in this section is because of the usefulness of positron data in constraining leptophilic models. However, we also study cases where annihilation into b-quark pairs contribute. We assumed an

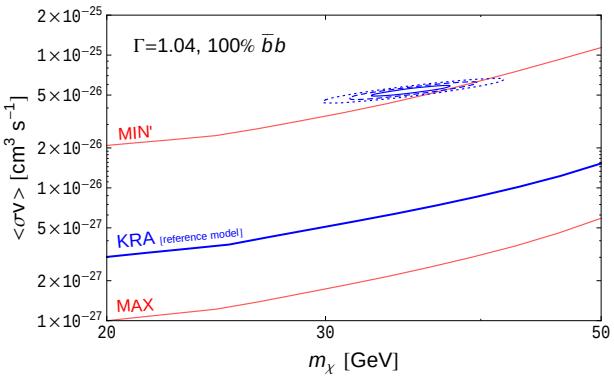

Figure 5.7: Limits on the annihilation of DM into $b\bar{b}$ that result from using the "MAX", "KRA" and "MIN"' propagation models as reference models. For comparison, we also include the preferred region inferred by the inner Galaxy analysis in [24] ($\Gamma = 1.04$).

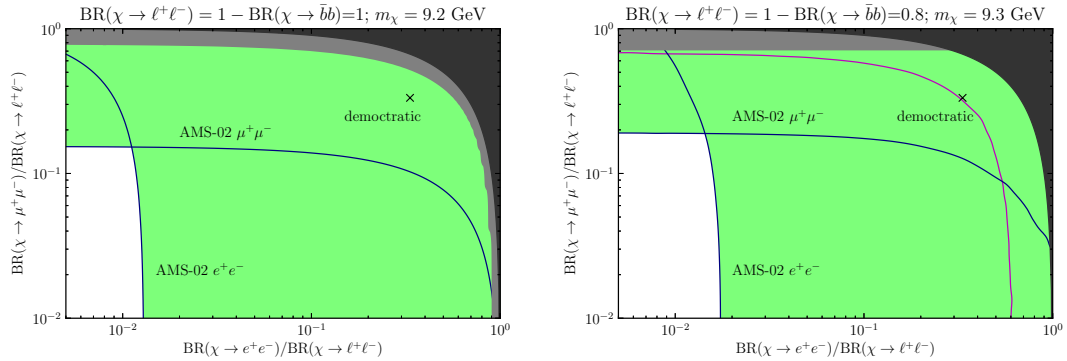

Figure 5.8: Left: positron limits on the relative branching ratios of charged leptons in the leptophilic DM interpretation of the GeV excess. Green regions are excluded, while the spectral fit to the GeV excess "fails" ($\Delta\chi^2 \gtrsim 25$) in the gray region. Right: same as left but with a small admixture of $\bar{b}b$ annihilation.

inner slope $\gamma = 1.26$ in formula (3.7) and during the fit we constrained the DM mass to be larger than 9.2 GeV so as to bypass the unaccounted effects of bremsstrahlung and inverse Compton scattering that are expected to contribute at low energies [127].

For several values of the two independent leptonic branching ratios BR($\chi\chi \to e^+e^-$) and BR($\chi\chi \to \mu^+\mu^-$), we draw allowed and excluded regions by the AMS-02 analysis in fig. 5.8.

5.4.3 Synchroton radiation

The 408 MHz upper limit analysis introduced in Sec. 4.4.1 and applied in the previous one will also prove useful for testing the consistence of the DM interpretation of GeV excess with radio observations at the GC. As done with antiprotons, we keep the annihilation rate as a free parameter that we constrain by means of null DM searches in the radio band at the GC. The main difference between this case and the previous one is that the DM distribution considered above is shallower than the type of distributions considered here. Owing to the strong dependence of the DM-induced radio signal on the DM distribution –in contrast to the magnetic field profile– this will turn out to make a huge difference and render the radio limits reported in this section rather strong.

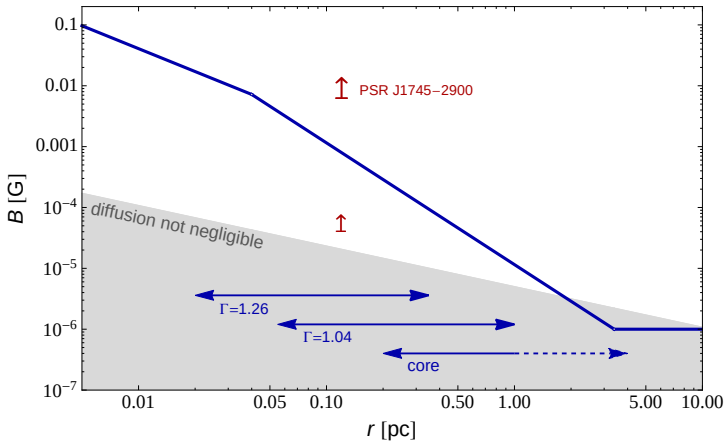

Figure 5.9: *Solid line*: equipartition magnetic field (4.46). Magnetic fields within the gray region are not strong enough for diffusion to be neglected (as assumed in our analysis, *cf.* Eq. (5.24)). Lower limit arrows (in red) refer to respectively "ultra-conservative" and "realistic" field inferred values from the recently discovered magnetar PSR J1745-2900 [25] (see section 4). Horizontal arrows indicate the ranges that are interesting for the calculation of the annihilation signal.

A naïve application of formula (5.22) in modelling the 408 MHz measurement [115] will put too strong constraints on the annihilation rates for the masses considered here. Although the applicability of the formula is not questioned provided the conditions discussed in section 4.4.1 are fulfilled, N-body simulations can not resolve the radial dependence of the DM profile in the inner 5 pc. It is precisely in this region that most of the synchrotron signal as portrayed in fig. 5.9 is originated and such uncertainties certainly represent a limiting factor in our analysis. In the same way as we did before, we integrate the flux (5.22) only in those regions where the magnetic field is stronger than a critical one

$$B_{\rm crit.}(r) \gtrsim 4\,\gamma^{2/3}\left(\frac{\rm pc}{r}\right)^{2/3}\mu{\rm G}\ , \tag{5.24}$$

which is defined by eq. (5.23) and the DM scale height corresponds to a generalized NFW profile with inner slope γ.

In order to quantify the propagated uncertainties on the radio flux due to not knowing the radial dependence of the DM profile inside the region defined by $r \lesssim 5$ pc, we consider modifications in the inner DM profile in a way that is still consistent with both the GeV excess' DM interpretation and N-body simulations. Specifically, we introduce a core radius below which the DM density remains constant and whose magnitude we take as a variable. For several core radii the associated radio limits on τ (80%) and b-quark (20%) pairs that we obtain by applying formula (5.22) in Fig. 5.10, where we used the equipartition magnetic field profile (4.46) introduced in Sec. 4.4.1.

Notice that the existence of such DM core is expected if one takes into account three effects that become important in regions where the DM density is large. Namely, self-scattering, annihilations and the presence of a super massive black hole (SMBH) at the center of our galaxy [128]. The scale at which this flattening is expected to occur is however orders of magnitude smaller than the core radii that we consider here. In some extreme cases [129, 130], though, partial flattening can occur at the 1 pc scale.

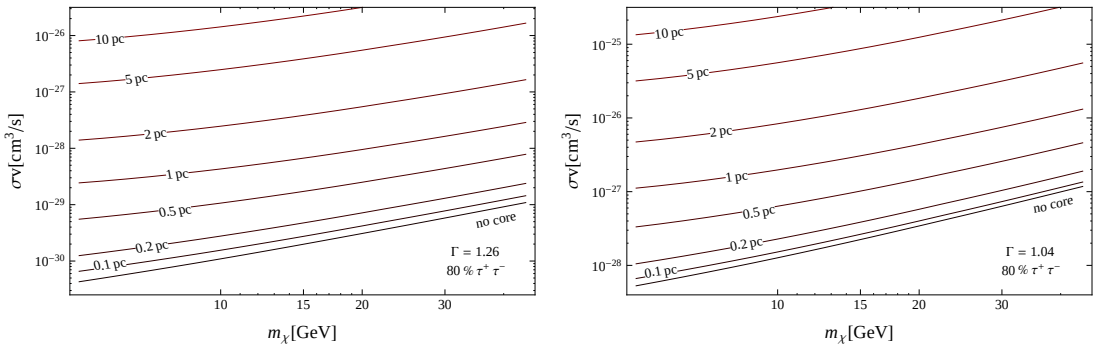

Figure 5.10: *Left*: Radio limits on DM annihilation into 80% $\tau^+\tau^-$ and 20% $\bar{b}b$ for a generalized NFW profile with $\gamma = 1.26$ (lowest line). The rest of the curves correspond to the same limits but for a NFW profile with an artificial core of size r_c as indicated. *Right*: same as left but with an inner slope of $\Gamma = 1.04$.

5.4.4 Discussion

Careful investigation of the consequences of claiming that the apparent GeV excess is originated from DM annihilations led to the interesting results that we outlined in figs. 5.5, 5.8 and 5.10. Notice that depending on the messenger, some regions turn out to be more relevant than others when estimating their associated fluxes. For instance, high energetic cosmic-ray positrons probe only regions close to the solar system while synchrotron signals from DM are expected to be mainly produced close to the GC.

This is better visualized in Fig. 5.11 where for an interesting set of annihilation channels we show our limits as compared to the central values of the best-fit annihilation rates. We also include the positron limits from Ref. [10] in the last panel. For $\gamma = 1.26$ vanishing branching ratios for DM annihilation into light leptons passed the test performed in our analysis as apparent in the left panel of fig. 5.8, whereas for the scenario of a less pronounced r-dependence close to the GC $\gamma = 1.04$, the limits become more stringent and are in tension with the GeV excess interpretation. This behaviour is exactly the opposite to what occurs with our radio constraints. This is of course a manifestation of the previous paragraph's point. Namely, DM-induced positron fluxes are originated in nearby regions and scale almost exclusively with the annihilation rate (independent of the DM profile) whereas synchrotron fluxes come from the inner few pc of the galaxy and mostly depend on the DM profile, as stressed before.

The thorough analysis of PAMELA antiproton data where a novel strategy in accounting for the uncertainties from nuclear and propagation effects proved to be quite successful in constraining DM annihilations at the mass range relevant to the GeV excess. We were able to fit the data nicely with our three-parameter model and consequently to obtain strong bounds on the DM signals.

We additionally performed several checks in order to better interpret the "strength" of our antiproton results. For instance, we re-performed the same analysis to various subsets of data points in order to find out which data points are the most relevant. We observed that even data points corresponding to energies as high as 20 GeV turn out to be important. This is a bit counterintuitive since data points with energies larger than ~ 10 GeV are only mildly affected by the DM signal –see Fig. 5.5–. On the other hand, cutting out several lower energy bins (with energies up to ~ 1 GeV) also lead to strong bounds for DM masses larger than ~ 10 GeV. This reflects the fact that

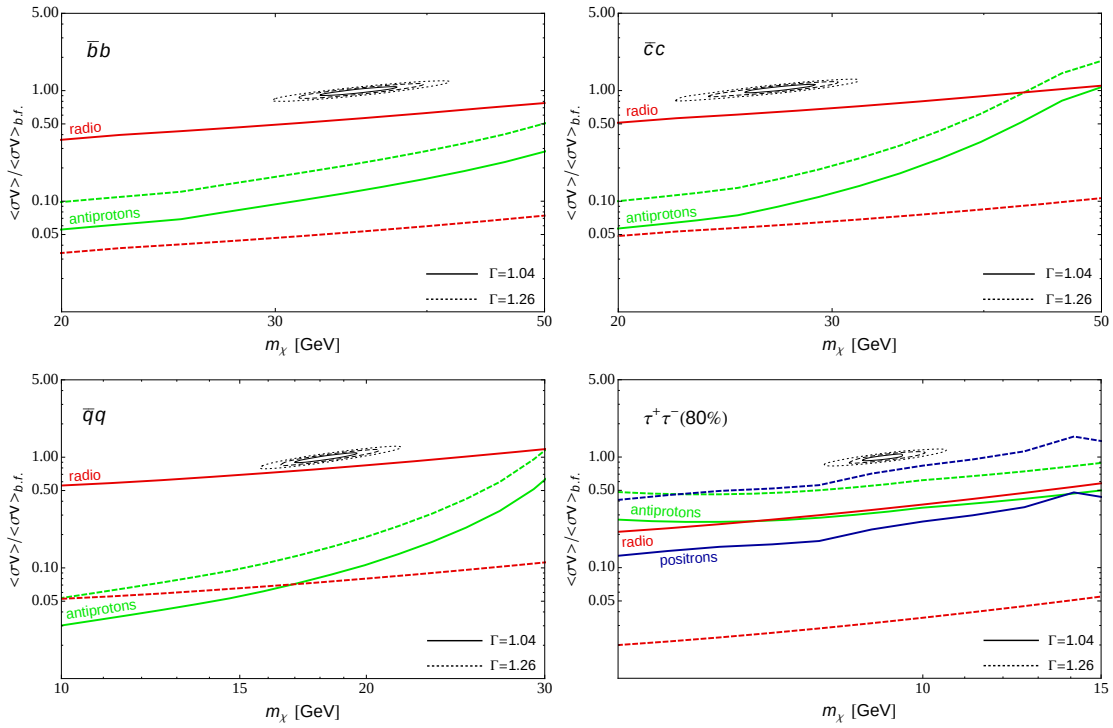

Figure 5.11: Summary of our updated constraints for various annihilation channels. Conveniently the *ratio* of the our limits on $\langle\sigma v\rangle$ and the corresponding one as inferred form the DM interpretation of the GeV excess. Dashed (solid) correspond to a slope $\gamma = 1.26$ ($\Gamma = 1.04$).

the PAMELA [23] measurements of antiprotons with "intermediate" energies are quite accurate. We also tested –and found an excellent agreement– our analytical treatment of solar modulation against a more sophisticated numerical one. Namely, the code HelioProp [74] which basically solves the 4D propagation equations that describe the diffusion and drift motion along the large scale gradients of the spiralling solar magnetic field, the heliospheric current sheet, and the radially expanding solar wind.

Our positron bounds on the model-building for the GeV excess exclude well-motivated scenarios where the branching ratios of DM annihilation into electron-positron and muon pairs are sizeable. In fact, 100% leptonic channels do not fit well the GeV excess' spectrum: points sitting in the allowed white region in the left panel of figure 5.8 feature $\Delta\chi^2 \sim 130$. Adding sizeable branching fraction to hadronic channels such as $\bar{b}b$ improves this. However the constraints shown in the right panel of the same figure still pose strong challenges on the model-building.

Our radio limits serve as an example of how strong the DM signal depends on the DM distribution. Fig. 5.10 demonstrate how radio limits span four orders of magnitude when we only consider core radii of the DM distribution that are smaller than 10 pc.

This property fortunately does not apply to the rather uncertain magnetic field. We tested this by considering different magnetic field models. In figure 5.12 we show the resulting radio limits on (80%) τ pairs from considering two alternative models of constant magnetic field. The field's strength in such models correspond to conservative and agresive lower limits on the GC's inner 0.12 pc magnetic field as estimated by Ref. [25] in the context of the recent discovery of a magnetar sitting in that region and was also claimed in that reference.

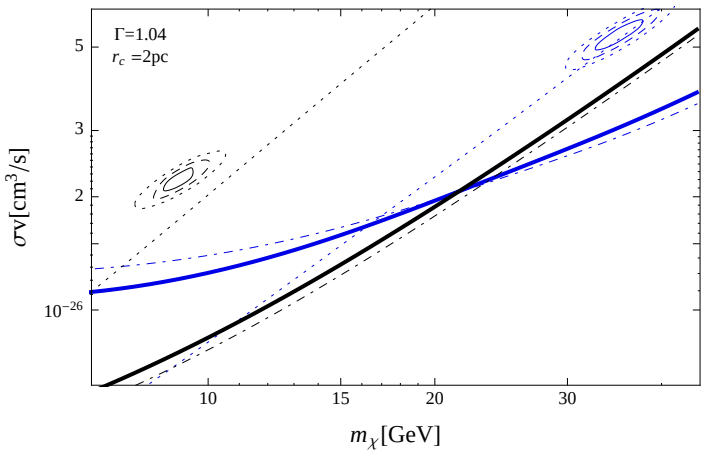

Figure 5.12: Radio constraints for a constant magnetic (instead of the equipartition magnetic field). Dot-dashed lines refer to $B = 50\,\mu$G and dotted lines $B = 8\,$mG (dotted lines).

The results from this test are clear: radio limits are almost insensitive to changes in the magnetic profile, provided this is strong enough (i.e. it fulfills condition (5.24)). One can see this analytically by taking a closer look at formula (5.22). The dependence of the flux on B comes only from the product $EN(E)$, let us now assume constant B so that such a term can be pulled out of the integral. Now, observe that for all annihilation channels considered the energy dependence of $N(E)$ is weak if $E \ll m_\chi c^2$, meaning that the B-dependence in formula (5.22) is exactly the same of E –the electron's energy emitting frequency ν–, namely $B^{-0.5}$.

Limitations in our method may then arise from non consideration of other processes responsible for the electrons' energy losses (ICS, bremsstrahlung). For a discussion on these possible caveats, we refer to Ref. [131] where not only other sources of energy loss were discussed, but also they considered advection and convection. See also [132]. A recent study [133], however, reevaluated our radio limits on the GeV excess with the only difference that they included electron energy losses due to inverse Compton scattering in a point-source like radiation field. They also estimate spherical convection effects and used a weaker magnetic field normalization. Their results are up to three orders of magnitude less stringent. In any case, as stressed before and made clear by fig. 5.10, most of the uncertainties in GC radio limits stem from the corresponding uncertainty of the inner structure of the DM distribution.

Chapter 6

Effects of non-vanishing relative speeds

Most of the results discussed so far are based on the assumption that the relative speed of annihilating WIMPs is negligibly small, or equivalently, the 2-WIMP initial state is an s-wave. This is of course well justified by the fact that DM particle speeds are typically of the order of $100\,\mathrm{km/s}$[1], less than 1% of the speed of light. In this chapter we will discuss several cases where relaxation of the $v = 0$ condition leads to even qualitative differences in the theoretical prediction signals relevant to indirect searches for DM. We will then focus on gamma rays signals from the model with universal extra dimensions introduced in section 1.3.1, where a detailed study of resonant processes that could potentially enhance the associated line signals is given. In the last section we introduce the rather interesting Bañados-Silk-West effect and discuss scenarios where such an effect can lead to unique signatures in the high-energy gamma-ray sky. The essential points of the following discussion were included in my publication [I].

6.1 Enhanced annihilation rates

In this section we shall pay special attention to the velocity dependence of the annihilation rate. In particular, we discuss a number non-trivial observable effects such as *Sommerfeld ennhancement*, *thresholds* and *resonances*, that in one way or another affect the annihilation rates of WIMPs.

6.1.1 Sommerfeld enhancement

An interesting situation that we have not discussed so far is the possibility that DM particles form bound states due to Coulomb-like interactions amongst them. Motivated by several reasons –e. g. explaining the positron excess [134] discussed in sec. 2.3.2– several models with this property have been put forward. Such a scenario requires though a massless (or light) mediator that only couples to the DM particle.

The impact on the annihilation cross sections of the effectively long-range interaction can be sizeable. This phenomenon, known as the *Sommerfeld enhancement*, is a fascinating topic which unfortunately remains beyond the scope of this manuscript. Following Ref. [134], we will motivate the idea behind the Sommerfeld enhancement with a simple classical example: consider the scattering of a sphere of radius R and mass M

[1]The reader can estimate such speeds by considering, for instance, the maximum escape velocity of a DM particle in an NFW-like DM halo of our galaxy size. A rough estimate yields $v_{\mathrm{max}} \sim 500\,\mathrm{km/s}$

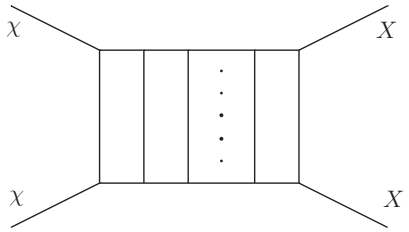

Figure 6.1: Graphical representation of the Sommerfeld enhancement in terms of Feynman diagrams in the particular case of DM neutralino annihilating into a two-vector state [26].

at rest and a test particle with velocity v at infinity and impact parameter b. In the absence of long-range interactions, the cross section is simply $\sigma_0 = \pi R^2$ as the can only collide if $b < R$. If they, in turn, interact gravitationally they will collide even if the test particle $R < b < b_{\max}$, where $b_{\max}$ is the (critical) impact parameter at which the test particle collides with the sphere. The cross section is therefore enhanced

$$\sigma = \sigma_0 \left(1 + \frac{v_{\rm esc}^2}{v^2}\right) > \sigma_0 \ ,$$

where $v_{\rm esc}^2 = 2GM/R$ is the escape velocity from the surface of the sphere. Notice that for small speeds ($v \ll v_{\rm esc}$) the cross section diverges as v^{-2}.

A similar phenomenon occurs when instead of classical objects we consider quantum particles. There, the Sommerfeld effect starts to become important when the de Broglie wavelength $\lambda_{\rm dB} \sim 1/m_\chi v$ is comparable to the Bohr radii of the coupled states $a_o \sim (\alpha_\phi m_\chi)^{-1}$ ($\alpha_\phi = g_\phi^2/4\pi$), where g_ϕ is the coupling constant between the DM particles and the mediator and we neglect for the moment the mass of the mediator. Defining the parameter $\epsilon_v = \lambda_{\rm dB}/a_0 = \alpha_\phi/v$, the Sommerfeld factor $S(v) \equiv \sigma/\sigma_0$ can be computed analytically, yielding

$$S(v) = \frac{\pi/\epsilon_v}{1 + {\rm e}^{-\pi/\epsilon_v}} \ . \tag{6.1}$$

Since this is a low energy effect, non-relativistic quantum mechanics applies. In fact, Sommerfeld's original results [135] are based on a quantum mechanics calculation of a spinless electron subject to a Coulomb potential. A full quantum field theoretical account for this effect correspond to summing over all ladder diagrams such as the ones displayed in figure 6.1. Such a tedious computation is equivalent to solving the radial Schrödinger equation for the two-body (s-)wave function imposing the appropriate boundary conditions [134].

6.1.1.1 Saturation

By taking into account the mass of the mediator, we introduce a new length scale (m_ϕ^{-1}) into the problem. Since the scale defined by m_ϕ^{-1} determines ϕ's range of interaction, the Sommerfeld enhancement saturates for sufficiently small speed: when $\lambda_{\rm dB} \gg m_\phi^{-1}$ or $\epsilon_v \ll \epsilon_\phi$, by defining $\epsilon_\phi = m_\phi/\alpha_\phi m_\chi$. Under this conditions $S(v) \sim 1/\epsilon_\phi$, which is constant. Rather interestingly, for a scalar mediator (Yukawa) bound states develop giving rise to resonances at specific values (discrete spectrum) of ϵ_ϕ. This is summarized in fig. 6.2

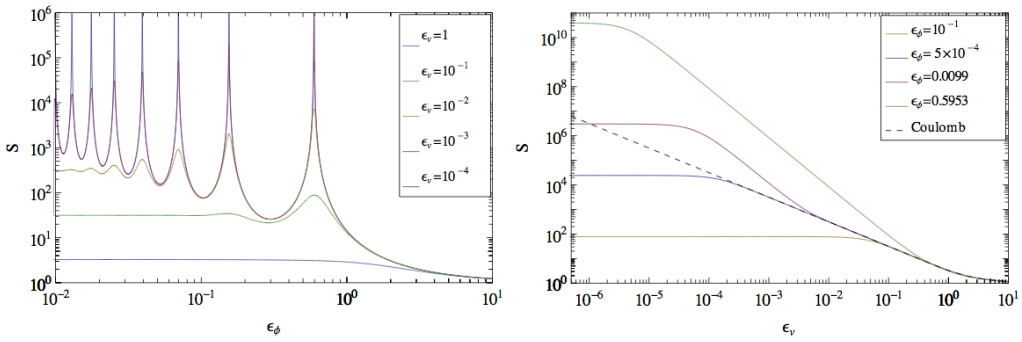

Figure 6.2: Sommerfeld enhancement as a function of ϵ_v and ϵ_ϕ. Images courtesy of L. van den Aarsen [27]

In Fig. 6.2 it is apparent that by varying ϵ_v while keeping ϵ_ϕ constant close to threshold, $S(v)$ follows the following dependence $S(v) \propto v^{-2}$ for sufficiently large v. Far from a threshold, $S(v)$ follows the behaviour determined by eq. (6.1): $S(v) \propto v^{-1}$.

6.1.2 Resonances

In the most general sense, when the physical conditions of a system (e. g. a two-particle initial state) are in tune with the ones defining a quantum excitation (bound state or particle) in the theory, then resonant phenomena are expected. These typically manifest themselves as enhancements in the interaction probability (cross section) of certain processes, e. g. the peaks in Fig. 6.2.

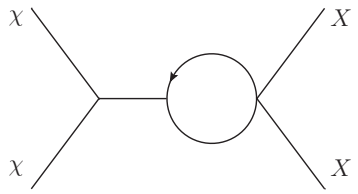

Figure 6.3: Resonance by creating a bound state close to threshold.

Although we will mainly be interested in the so-called *Breit-Wigner* resonances, it is worth mentioning other types of resonant effects that could potentially have an impact on indirect DM searches. One example is the creation of a bound state of two particles, such as quarkonia, close to the energy threshold (minimum energy required to create them). Such bound state (resonance) then decays producing in this way a resonating effect quite similar to the Sommerfeld enhancement. The theoretical treatment of this problem is actually identical: non-relativistic quantum mechanics is equivalent to adding an infinite number of Feynman diagrams.

6.1.2.1 Breit-Wigner resonances

Although the original work by Breit and Wigner [136] on resonances was concerned with nuclear excitations, i. e. bound states, the term Breit-Wigner resonance in relativistic quantum field theory is associated to s-channel processes like the one depicted in fig. 6.4.

The center-of-mass energy can "resonate" with the mass of the virtual particle occurring in the Feynman diagram and since the propagator in momentum space diverges, the full amplitude also diverges at tree-level. This is of course a consequence of not considering further terms in the perturbation series and using a propagator with bare parameters.

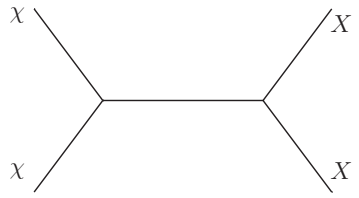

Figure 6.4: Feynman diagram of a general Breit-Wigner resonance.

Owing to the optical theorem discussed in the previous chapter, full computation of the renormalized propagator is possible at all orders of perturbation theory [40]. The resulting cross-section close to resonance has the following shape

$$\sigma \propto \left| \frac{1}{p^2 - m_{\text{res.}}^2 + i m_{\text{res.}} \Gamma_{\text{res.}}} \right| , \tag{6.2}$$

where $\Gamma_{\text{res.}}$ is the decay width of the resonance. Eq. (6.2) resembles the resonant scattering amplitude of neutrons with nucleons studied by Breit and Wigner close to the resonance energy E_0 at which nuclear excitations are created

$$f(E) \propto \frac{1}{E - E_0 + i\Gamma/2} ,$$

where E is the energy of the system and Γ is the decay width of the excitation. Since our focus will be on this type of resonances we will omit the Breit-Wigner suffix and name them henceforth just resonances.

Before running into the particular example of Breit-Wigner resonances in the context of Universal Extra Dimensions, we would also like to point out that there can be more exotic situations where resonance effects can come about. For instance, consider a theory where DM bound states and at the same time Breit-Wigner resonances can be formed. In such cases re-scattering diagrams as the one shown in figure 6.5 are of the same order of tree-level diagrams and should therefore be included in the calculation.

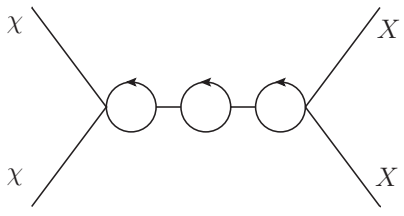

Figure 6.5: Rescattering diagram in a Breit-Wigner resonance.

6.2 UED resonances

Let us now consider the concrete case of Universal Extra Dimensions introduced in section 1.3.1. The particle spectrum obtained there is determined by the different modes

that arise in the Fourier expansion of the 5D fields occurring in the model. As shown in section 1.3.1 the bare masses of such modes are approximately integral multiples of the compatification's mass scale R^{-1}, rendering radiative corrections essential in e. g. determining what the lightest Kaluza-Klein particle (LKP) is.

An interesting consequence of this "ladder structure" of the UED particle spectrum is the fact that owing to the particularity that mode-2 particles ($\mathrm{KK}^{(2)}$) are roughly twice as heavy as mode-1 particles ($\mathrm{KK}^{(1)}$), the center of mass energy of two slow-moving LKP's ($\sim 2m_{\mathrm{KK}^{(1)}}$) is numerically close to the rest energy (mass) of mode-2 particles ($m_{\mathrm{KK}^{(2)}}$). Specifically, the difference $m_{\mathrm{KK}^{(2)}} - 2m_{\mathrm{KK}^{(1)}}$ is essentially proportional to the radiative corrections determining the model's actual masses. Since annihilations of slow-moving WIMPs are precisely the processes relevant for indirect DM detection, we shall study in detail the impact of this property in that context.

We already identify mode-2 particles in the UED model as potential Breit-Wigner resonances for the annihilation rate of LKP pairs. As a next step, we shall identify which ones of such mode-2 particles are allowed by the symmetries of the model (spin, charges, etc.) to resonate with the initial two-LKP particle state. Then we will focus on the decay widths of such resonances. Decay widths are essential in determining whether a certain resonance is important or not. Most of the following discussion will be concerned with the minimal UED –also introduced in section 1.3.1– however, our results can easily be generalized for non-minimal (next-to-minimal) scenarios where the LKP is the first excitation of the 5D photon field $B^{(1)}$.

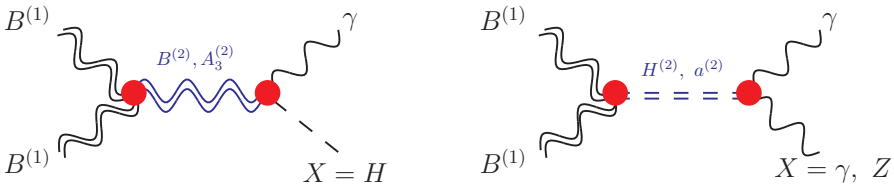

Figure 6.6: Relevant Breit-Wigner resonant diagrams for LKP annihilation in the UED model.

Charge conservation only allows mode-2 particles $B^{(2)}$, $A_3^{(2)}$, $H^{(2)}$ and $a_0^{(2)}$ to potentially resonate with a $B^{(1)}B^{(1)}$ initial state producing gamma-ray lines as depicted in figure 6.6. Notice that we neither drew diagrams where a vector resonance is connected to a vector-vector final state nor scalar particles connected to scalar-vector final states and no fermions occur in any of the final states. The former case is forbiden by the Landau-Yang theorem [137, 138] if the final state is composed by two gamma rays while the latter are forbidden by helicity conservation. Vector resonances with a γZ final state and $a_0^{(2)}$ resonances turn out to give no contribution owing to the anomaly cancellation property of the SM which is also applicable in UED[2]. Refer to appendix D for more details on such fascinating topics.

Let us now take a closer look at the mass spectrum of mode-1 and -2 Kaluza-Klein particles in the minimal UED (mUED) model so as to discriminate which decay channels are available for $B^{(2)}$, $A_3^{(2)}$ and $H^{(2)}$. Figure 6.7 displays the masses in units of the inverse compatification radius of both the relevant resonances (left bars) and mode-1 particles (dashed bars). The continous arrow indicate the dominant tree-level decay

[2]The $a_0^{(2)}$ is a linear combination of the fifth component of the 5D $Z^{(2)}$ boson and (predominantly) the imaginary part of the Higgs-doublet lower component $\chi_3^{(2)}$, both of which participate in the anomaly cancelation theorem ($\chi_3^{(0)}$ is the Goldstone boson absorbed by Z-boson's longitudinal degree of freedom)

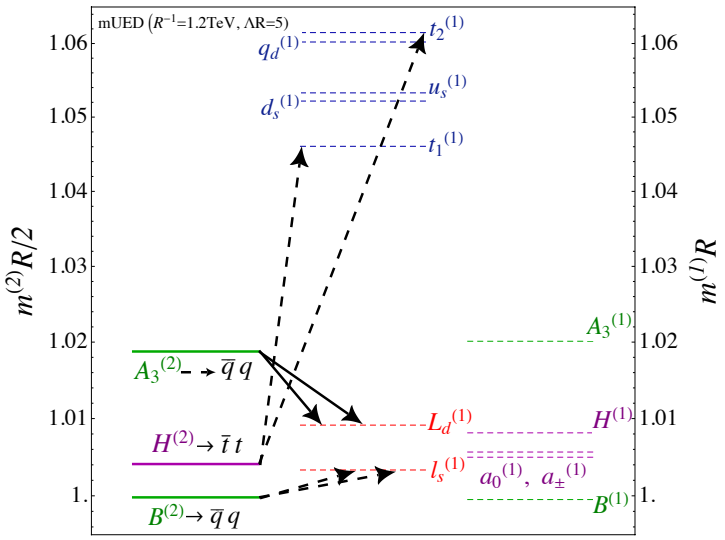

Figure 6.7: Mass spectrum of relevant 2nd-mode KK particles in the mUED scenario, in units of the inverse compactification scale R^{-1} (left column and axis). The middle and right columns display the mass spectrum of KK(1) states. The decay channels in the minimal scenario are displayed by solid arrows. Dashed arrows indicate the dominant decay process in non-minimal regimes.

mode of $A_3^{(2)}$ while the dashed ones corresponding dominant modes in non-minimal scenarios –if kinematics allow–. In the mUED model both $B^{(2)}$ and $H^{(2)}$ decay through loop-suppressed KK-number violating vertices into SM particles, rendering their decay widths rather width, potentially enhancing the cross section on resonance.

6.2.1 Decay witdhs

As discussed in section 1.3.1.1, stability of the electroweak vacuum and thermally produced abundance of DM can be achieved in a rather narrow parameter space in the UED model [44]. As a benchmark, we use

$$\Lambda R = 5, \qquad R^{-1} = 1.2\,\text{TeV} \tag{6.3}$$

whenever we state numerical results.

In the UED model tree-level couplings preserve KK number and can easily be derived from the 5D picture (see, e. g., Refs. [43, 139] for a list of Feynman rules). KK-number violating effective couplings are however more involved. In general, these are of radiative origin as they counterterms located on the orbifold fixed points are KK-number violating. Besides calculating the radiative corrections to the vertex on the brane, we will have to take into account kinetic and mass mixing effects between states of different KK number. For instance, in the mUED case the coupling of a generic gauge field A_μ to chiral SM fermions f,

$$\mathcal{L}_{\text{eff}} \supset g_{\text{eff}}^{A\bar{f}f}\, A_\mu^{(2)}{}_a \bar{f}^{(0)} \gamma^\nu T^a \frac{1 \pm \gamma^5}{2} f^{(0)}\,, \tag{6.4}$$

is given by

$$g_{\text{eff}}^{A\bar{f}f} = \frac{g}{\sqrt{2}} \left[\frac{\bar{\delta}(m^2_{A^{(2)}})}{m_2^2} - 2\frac{\bar{\delta}(m_{f^{(2)}})}{m_2} \right], \tag{6.5}$$

where g is the corresponding coupling between zero modes, $m_n \equiv n/R$ and $\bar{\delta}(m)$ refers to radiative mass corrections due to terms localized on the brane.

6.2.1.1 $B^{(2)}$ decay

In the mUED model the $B^{(2)}$ is the lightest of all level-2 KK particles. Its only kinematically possible decay is directly into SM particles and it's described by KK-number violating effective vertices. The leading decay channel is $B^{(2)} \to \bar{q}q$ has a branching ratio of around 99% [140]. The mass corrections of $B^{(2)}$ and $f^{(1)}_{s,d}$ are given by [4, 140]

$$\frac{\bar{\delta}m^2_{B^{(2)}}}{m_2^2} = -\frac{g'^2}{6}\frac{\log\frac{\Lambda^2}{\mu^2}}{16\pi^2}\,, \tag{6.6}$$

$$\frac{\bar{\delta}m_{f_s^{(1)}}}{m_2} = \left(\frac{9}{4}Y^2_{f_s}g'^2 + 3g_s^2 - \frac{3}{2}y_f^2\right)\frac{\log\frac{\Lambda^2}{\mu^2}}{16\pi^2}\,, \tag{6.7}$$

$$\frac{\bar{\delta}m_{f_d^{(1)}}}{m_2} = \left(\frac{9}{4}Y^2_{f_d}g'^2 + \frac{27}{16}g^2 + 3g_s^2 - \frac{3}{4}y_f^2\right)\frac{\log\frac{\Lambda^2}{\mu^2}}{16\pi^2}\,, \tag{6.8}$$

where Y refers to the hypercharge, g' [g] denotes the $U(1)$ [$SU(2)$] coupling constant and y the Yukawa coupling. The term proportional to the strong coupling constant g_s only appears for quarks. Using eq. (6.5), this translates into the vertex relevant for $B^{(2)} \to \bar{f}f$ (as reported in Ref. [140])

$$\mathcal{L}_{\text{eff}} \supset -\bar{f}\gamma^\mu\left(g^L_{\text{eff}}\frac{1-\gamma_5}{2} + g^R_{\text{eff}}\frac{1+\gamma_5}{2}\right)fB^{(2)}_\mu\,, \tag{6.9}$$

$$g^L_{\text{eff}} = \frac{g'Y_{f_d}}{\sqrt{2}}\left[\frac{g'^2}{6}(1{+}27Y^2_{f_d}) + \frac{27}{8}g^2 + 6g_s^2 - \frac{3}{2}y_f^2\right]\frac{\log\frac{\Lambda^2}{\mu^2}}{16\pi^2}\,, \tag{6.10}$$

$$g^R_{\text{eff}} = \frac{g'Y_{f_s}}{\sqrt{2}}\left[\frac{g'^2}{6}(1{+}27Y^2_{f_s}) + 6g_s^2 - 3y_f^2\right]\frac{\log\frac{\Lambda^2}{\mu^2}}{16\pi^2}\,. \tag{6.11}$$

The decay rate is then

$$\frac{\Gamma_{B^{(2)}\to\bar{f}f}}{m_{B^{(2)}}} = \frac{1}{12\pi}\left(1-\frac{4m_f^2}{m^2_{B^{(2)}}}\right)^{\frac{1}{2}}\times \times\left[\left(1+\frac{2m_f^2}{m^2_{B^{(2)}}}\right)g_V^2 + \left(1-\frac{4m_f^2}{m^2_{B^{(2)}}}\right)g_A^2\right]\,, \tag{6.12}$$

where $g_V \equiv (g^R_{\text{eff}}+g^L_{\text{eff}})/2$ and $g_A \equiv (g^R_{\text{eff}}-g^L_{\text{eff}})/2$. Adopting the values stated in eq. (6.3) $g^L_{\text{eff}} = 0.09$ and $g^R_{\text{eff}} = 0.11$, and the decay rate amounts to $\Gamma_{B^{(2)}} \approx 0.813\text{GeV}$.

When allowing for arbitrary mass splittings on the other hand $B^{(2)}$ would instead mainly decay into a pair of first-KK-level charged leptons; the corresponding rate is then given by

$$\frac{\Gamma_{B^{(2)}\to\bar{l}_s^{(1)}l_s^{(1)}}}{m_{B^{(2)}}} = \frac{Y^2_{l_s}g'^2}{4\pi}\left(1-\frac{4m^2_{l_s^{(1)}}}{m^2_{B^{(2)}}}\right)^{\frac{1}{2}}\left(1+\frac{2m^2_{l_s^{(1)}}}{m^2_{B^{(2)}}}\right)\,. \tag{6.13}$$

In such case, the existence of a tree-level rather than loop-suppressed coupling typically over-compensates the additional phase-space suppression, and the decay happens considerably faster (with $\Gamma \sim 10\text{GeV}$).

6.2.1.2 $A_3^{(2)}$ decay

In the mUED model, $A_3^{(2)}$ is considerable more massive than $B^{(2)}$. As a result, kinematics allows for six different decay dominant channels into first-level leptons $\bar{\ell}_{s,d}^{(1)}\ell_{s,d}^{(1)}$. By making the identification $Yg' \to g/\sqrt{2}$, the corresponding decay rate is described by Eq. (6.13). The total decay rate is $\Gamma_{A_3^{(2)}} \approx 70\,\mathrm{GeV}$.

In non-minimal scenarios, mass splittings may kinematically not allow the $A_3^{(2)}$ to decay into first-KK-level states, but only into SM particles. Assuming that non-trivial mass and kinetic boundary terms are added at the cut-off scale, in analogy to Eq. (6.9), the radiative vertex that couples $A_3^{(2)}$ to SM fermion is given by

$$\mathcal{L}_{\text{eff}} \supset -g_{\text{eff}}^L \bar{f}\gamma^\mu \frac{1-\gamma_5}{2} f A_{3\mu}^{(2)}\,, \tag{6.14}$$

$$g_{\text{eff}}^L = \frac{gT_{3f}}{\sqrt{2}}\left[\frac{9Y_{f_L}^2}{2}g'^2 - \frac{33}{8}g^2 + 6g_s^2 - \frac{3}{2}y_f^2\right]\frac{\log\frac{\Lambda^2}{\mu^2}}{16\pi^2}\,, \tag{6.15}$$

where T_{3f} is the fermion weak isospin charge. In deriving this, we used again formula (6.5) and also [4]

$$\frac{\bar{\delta}m_{W^{(2)}}^2}{m_2^2} = \frac{15}{2}\frac{g^2}{16\pi^2}\log\frac{\Lambda^2}{\mu^2}\,. \tag{6.16}$$

The total width becomes numerically $\Gamma_{A_3^{(2)}} \approx 0.8\,\mathrm{GeV}$, with branching ratios of 11.2% for $\bar{t}t$, 11.4% for $\bar{b}b$, 18.0% for other quark-antiquark pairs and 0.9% for every lepton pair.

6.2.1.3 $H^{(2)}$ decay

If we assume minimality, the only possible tree-level decay of the second KK-level Higgs is $H^{(2)} \to a_0^{(1)}B^{(1)}$. This decay is kinematically forbidden for $R^{-1} \lesssim 1\,\mathrm{TeV}$. Therefore, $H^{(2)}$ is also metastable and decays predominantly into top anti-top pairs due to a radiatively generated vertex $\mathcal{L}_{\text{eff}} \supset g_{\text{eff}}H^{(2)}\bar{t}t$, where ($\lambda_h$ being the quartic coupling of the Higgs potential) [3] [140]

$$g_{\text{eff}} = \frac{y_t}{12}\left[16g_s^2 + \frac{33}{4}g^2 + \frac{23}{6}g'^2 - 9y_t^2 + 3\lambda_h\right]\frac{\log\frac{\Lambda^2}{\mu^2}}{16\pi^2}\,.$$

From this, the decay rate follows as

$$\frac{\Gamma_{H^{(2)}\to\bar{t}t}}{m_{H^{(2)}}} = \frac{3g_{\text{eff}}^2}{8\pi}\left(1 - \frac{4m_t^2}{m_{H^{(2)}}^2}\right)^{\frac{3}{2}}\,.$$

The factor 3 accounts for the number of colors. Numerically, we find $g_{\text{eff}} = 0.0189$ and thus a decay rate of $\Gamma_{H^{(2)}} \approx 0.383\mathrm{GeV}$.

In non minimal scenarios, if $H^{(2)}$ has a sufficiently large it will mainly decay into $\bar{t}_s^{(1)}t_d^{(1)}$ and $\bar{t}_d^{(1)}t_s^{(1)}$ pairs. In this case, one has an *axial* scalar coupling with

$$g_{\text{eff}} = 2g\frac{m_f}{m_W}\,. \tag{6.17}$$

Numerically, this gives $\Gamma_{H^{(2)}} \sim 160\mathrm{GeV}$, i.e. a much faster decay than in the mUED scenario.

[3] Here, we corrected a similar formula found in [140] by including scalar-vector-fermion loops.

6.2.2 Vertices

The blobs in figure 6.6 refer to all possible Feynman diagrams connecting the particles attached to them. While we provide in appendix D a detailed account for these, it is instructive to make some general comments about their computation.

We first notice that we can decompose the computation of the diagrams 6.6 into two decoupled parts (blobs) according to the following formulas for the amplitudes

$$i\mathcal{M}_{\rm Vec} = \epsilon_1^\mu \epsilon_2^\nu L^\rho_{{\rm Vec}\mu\nu} \frac{-\eta_{\rho\sigma} + \frac{P_\rho P_\sigma}{m^2_{\rm Vec}}}{s - m^2_{\rm Vec} + i m_{\rm Vec}\Gamma_{\rm Vec}} R^\sigma_{{\rm Vec}\alpha} \epsilon_\gamma^\alpha \ , \tag{6.18}$$

$$i\mathcal{M}_{H^{(2)}} = \epsilon_1^\mu \epsilon_2^\nu L_{H^{(2)}\mu\nu} \frac{1}{s - m^2_{H^{(2)}} + i m_{H^{(2)}}\Gamma_{H^{(2)}}} R_{H^{(2)}\alpha\beta} \epsilon_\gamma^\alpha \epsilon_X^\beta \ . \tag{6.19}$$

In contrast to the blobs on the left hand side of the diagram, the right blobs are KK-number violating. As mentioned in section 1.3.1 –and used in the last section– such symmetry is broken by the orbifold's compactification and it does not manisfest itself at tree-level but at the loop-level. In the appendix (D) we specify which Feynman diagrams participate in the computation of $R^{\gamma X}_{H^{(2)}\alpha\beta}$ $(X = \gamma, Z)$ and $R^{\gamma H}_{{\rm Vec}\alpha\beta}$ and in table 6.1 we indicate their relative strength by calculating the decay widths associated to such blobs. Concretely, we square decay amplitudes such as for example $\mathcal{M}_{H^{(2)}\to\gamma\gamma} = R^{\gamma H}_{H^{(2)}\alpha\beta}\epsilon_1^\alpha\epsilon_2^\beta$ and average over photons' helicities.

Resonance $Y^{(2)}$	$\boldsymbol{B^{(2)}}$	$\boldsymbol{A_3^{(2)}}$	$\boldsymbol{H^{(2)}}$
$Y^{(2)} \to \gamma X$	γH $(\Gamma \sim 10^{-4})$	γH $(\Gamma \sim 10^{-4})$	$\gamma\gamma$, γZ $(\Gamma \sim 10^{-4}, 10^{-3})$
$\Gamma^{\rm main}_{Y^{(2)}}$ (mUED)	$\bar{f}_{\rm SM} f_{\rm SM}$ $(\Gamma \sim 0.8)$	$\bar{l}^{(1)}_d l^{(1)}_d$ $(\Gamma \sim 70)$	$\bar{t}t$ $(\Gamma \sim 0.1)$
$\Gamma^{\rm main}_{Y^{(2)}}$ (non-mUED)	$\bar{f}^{(1)}_{d,\ s} f^{(1)}_{d,\ s}$ $(\Gamma \sim 15)$	$\bar{f}_{\rm SM} f_{\rm SM}$ $(\Gamma \sim 0.8)$	$\bar{t}^{(1)}_{d,s} t^{(1)}_{s,d}$ $(\Gamma \sim 160)$
$B^{(1)}B^{(1)}Y^{(2)}$	$\sim g'^3 m_t$	$\sim g'^2 g\, m_t$	$\sim g'^2 v$

Table 6.1: Decay channels and couplings for the resonances shown in Fig. 6.6. The decay rates are in GeV.

Left blobs preserve KK-number and as a matter of fact for the diagram with the $H^{(2)}$ s-channel there exists an EW symmetry-breaking tree-level coupling ($iL_{H^{(2)}\mu\nu} = ig'^2 v\eta_{\mu\nu}/2$) that connects the resonance with the two inital LKPs. In the case of the vector s-channel diagram, there are no tree-level BBB (or BBA_3) couplings as they would violate 5D gauge invariance. Nevertheless, the fermion loop diagrams connecting the $B^{(2)}$ and $A_3^{(2)}$ with the two $B^{(1)}$s are finite and were computed in the appendix with the aid of the computer software package FeynCalc [141]. For the LKP masses we are considering here, the resulting $L^\rho_{\mu\nu}$ tensors defined in eq. 6.18 are approximately proportional to m_t and, as expected, they vanish once EW symmetry is restored[4]. Last

[4]In 4D fermion loops with three gauge bosons lead to anomalous (gauge-symmetry violating) cou-

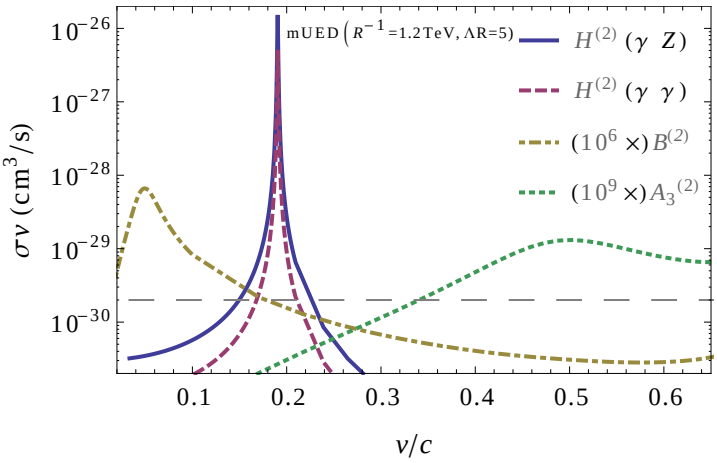

Figure 6.8: Resonant-diagram contributions to the $B^{(1)}B^{(1)} \to \gamma X$ annihilation rates in the minimal regime of the UED model as a function of the relative speed of the WIMPs (the curves associated with the $B^{(2)}$ and $A_3^{(2)}$ resonances are multiplied by factors 10^6 and 10^9 respectively). The horizontal dashed line indicates the value of $\sigma v_{\gamma\gamma}$ in the zero-velocity limit.

row of table 6.1 indicates for each resonance a rough estimate of the corresponding left blobs numerical value in terms of the relevant coupling constants.

6.2.3 Evaluation of the cross sections

Figure 6.8 graphically summarizes the results of the resonant cross section calculations we performed in the appendix D [142] and numerically evaluated with LoopTools [143]. The $H^{(2)}$ resonance is clearly the most prominent in light of its "metastability" (small width) and its tree-level coupling to the initial two-particle state. We observe a $\sim 10^{-8}$ and $\sim 10^{-11}$ relative suppression of respectively the $B^{(2)}$ and $A_3^{(2)}$ resonances respect to $H^{(2)}$. This can easily be explained in terms the elements of table 6.1. We observe that right blobs are roughly of the same order in all cases while the decay widths differ and specially the left blobs substantially and for instance the ratio between $B^{(2)}$ and $H^{(2)}$ peak-values can be correctly estimated as $(\Gamma_{B^{(2)}}/\Gamma_{H^{(2)}})^{-2}(g'^2/4\pi)(4\pi)^{-2}Y_{t_R}^6 \sim 10^{-8}$ (the $(4\pi)^{-2}$ is a standard estimate of the 1-loop integration prefactor which affects only the $B^{(2)}$-resonance).

For the Higgs resonance it is the γZ channel the dominant one in accordance to the numerical values on the first row of table 6.1. Comparing the computed values of the annihilation rate on resonance with the ones that results from considering box diagrams in the $\gamma\gamma$ channel with $v = 0$ [12] (dashed line in fig. 6.8) we see a strong enhancement. Even at $v = 0$ the $H^{(2)}$ s-channel diagram contributes at the same order as other relevant diagrams for the γZ channel. Owing to the small branching ratio $\Gamma_{H^{(2)}\to\gamma Z}/\Gamma_{H^{(2)}} \sim 1\%$ no rescattering effects are present and unitarity is not compromised by such large enhancements. Related to this, in this model $\tau_s^{(1)}\tau_d^{(1)}$ bound states can be created close to threshold through a $H^{(0)}$ s-channel that could potentially be another source of enhancement due to the large probability of such state to decay into a γ pair. This interesting posibility remains beyond the scope of this thesis. Notice that in order to

plings in the presence of chirality. In 5D there is no such thing as chirality and no anomalous couplings: a BBB triangle-loop vanishes in the free theory unless, of course, the U(1)$_Y$ symmetry is spontaneously broken. We exploited this property when computing $L_{\mu\nu}^{\rho}$ in appendix D.

reach such threshold LKP need larger velocities (see e. g. fig. 6.7) than the ones required to excite the Breit-Wigner resonances investigated in this chapter ($\sim 20\%$ of the speed of light).

As a final comment on the extension of our results to more general cases, we observe that the *location* of the resonance is highly sensitive to the radiative corrections determining the mass spectrum of the particles in the model. Even small departures from minimality will slightly change the parameters (in particular, the masses) of the model which in turn might shift the characteristic relative speed at which the inital two LKP state resonates with mode-2 particles without changing too much the height of the peaks in e. g. fig. 6.8. The only exception is when the mixing angle between mode-1 top quarks $\alpha_t^{(1)}$ gets appreciably affected by non-minimal terms as it enters quadratically in the cross sections (D.3), (D.4).

6.2.4 Higher order resonances

In the last section of this chapter we will discuss the possibility that DM interactions occur with arbitrarily large center of mass energy. Such posibility makes it a bit more challenging to make predictions for signals that are relevant to indirect DM searches as it makes it more model-dependent. Universal extra dimension models bear special features at high energies that are specially interesting to be investigated. Specifically, the model has a sort of tower structure which –naïvely reasoning– should be reflected in, for instance, the associated gamma-ray flux from annihilations of relativistic LKP. This will indeed be the case as we will demonstrate below.

Let us for simplicity consider the already familiar $B^{(1)}$ annihilations into γZ as it was the channel that received the strongest enhancement in the previous section. There, we noticed that both the narrow width and the tree-level coupling to $B^{(1)}B^{(1)}$ of the $H^{(2)}$ resonance is responsible of such sizeable effect. It is then reasonable to assume that at higher energies similar resonances will play a major role. We show this figure 6.9 where we observe how $H^{(2k)}$ $(k = 1, 2, \ldots)$ resonances can affect the $B^{(1)}B^{(1)} \to \gamma Z$ cross section in the mUED model at higher energies. The figure illustrates a striking property that is particular to the UED model. Namely, the spectrum of the annihilation cross section is composed by multiple narrow peaks separated almost equidistant in energy, being $\Delta E_\gamma \simeq 2R^{-1}$ the separation.

Peak contributions from superior resonances $H^{((2k)}$ $(k > 1)$ are however a few orders of magnitude off the corresponding $H^{(2)}$ contribution. This reflects the fact that *(i)* decay widths for superior resonances become larger and larger as more and more possible decay channels become available: $\Gamma_{H^{(2k)}}/m_{H^{(2k)}} \gg \Gamma_{H^{(2)}}/m_{H^{(2)}}$ and *(ii)* $B^{(1)}B^{(1)}H^{2k}$ vertices are no longer KK-number conserving $(k > 1)$ and therefore, they only exist in the orbifold fixed points. In the minimal scenario they are determined by radiative corrections, introducing thus an extra suppression when compared to the tree-level $B^{(1)}B^{(1)}H^2$ coupling. Notice that owing to this property, diagrams with vector resonances $B^{((2k)}$ and $A_3^{((2k)}$ $(k > 1)$ are not allowed as $\Lambda \gg m_{\rm EW}$.

In appendix D we obtain for the cases that interested us a number of KK-number violating operators from radiative corrections in the 5D theory. Some of the expressions we obtained there have also been implicitely used in previous sections (e. g. when computing $H^{(2)}$'s life time). As a final comment, we remind the reader that these results can qualitatively change if the minimality assumption is broken. For instance by allowing larger KK-number violating vertices while making vertices of the type $H^{(2k)}\bar{t}t$ smaller would definitely boost such resonances in such a way that they are comparable

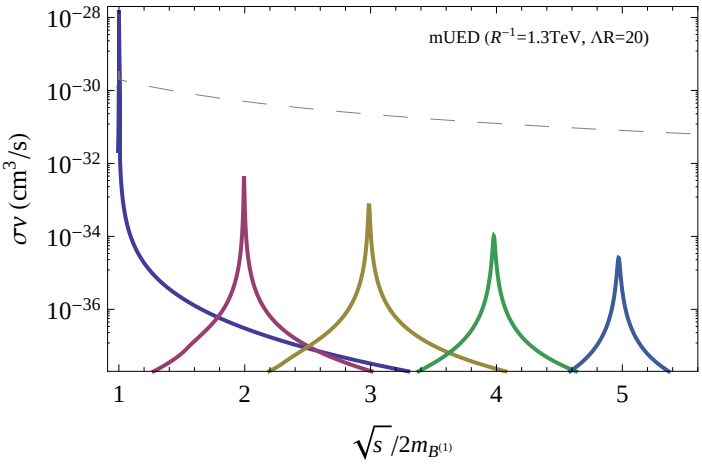

Figure 6.9: Contributions of the $H^{(2)}$ resonances ($k = 1, 2, \ldots$) to $\sigma v_{\gamma Z}$ as a function of $\sqrt{s}/2m_{B^{(1)}}$ in the mUED scenario. We take $\Lambda R = 20$ so as to allow for larger modes. The dashed line is an extrapolation ($\propto s^{-1}$) of the annihilation rate that results from neglecting resonances and $v \neq 0$.

to the corresponding $H^{(2)}$ resonance.

A more complete analysis should also include secondary photons from processes with larger branching ratios where the $H^{(2k)}$ resonances (and also possibly bound-states) can play a major role. Such secondaries are thus also expected, to a lesser extent though, to inherit the comb-like features encountered in fig. 6.9

6.3 Gamma-ray flux from slow-moving-DM annihilation

In order to account for the effects just discussed when making predictions of DM-induced gamma rays, we should unavoidably consider the velocity distribution $P_{\boldsymbol{r}}(\boldsymbol{v})$ of DM by averaging out the cross section –refer to appendix A–

$$\frac{\mathrm{d}\Phi}{\mathrm{d}E_\gamma}(E_\gamma, \psi) = \frac{1}{8\pi} \int \frac{\mathrm{d}\Omega}{\Delta\psi} \int_{\mathrm{l.o.s}} \mathrm{d}l(\psi) \rho^2(\boldsymbol{r}) \frac{1}{m_{\mathrm{DM}}^2} \left\langle \sigma v_{\mathrm{rel}} \sum_f \mathrm{BR}_f \frac{\mathrm{d}N_\gamma^f}{\mathrm{d}E_\gamma} \right\rangle_v , \tag{6.20}$$

where the bracket notation $\langle \ldots \rangle_v$ stands for relative-speed averaging; i. e. for a generic function $f(\boldsymbol{r}, \boldsymbol{v}_{\mathrm{rel.}})$

$$\begin{aligned} \langle f(\boldsymbol{r}, \boldsymbol{v}_{\mathrm{rel}}) \rangle_v &\equiv \int \mathrm{d}^3 v_1 \, \mathrm{d}^3 v_2 P_{\boldsymbol{r}}(\boldsymbol{v}_1) P_{\boldsymbol{r}}(\boldsymbol{v}_2) f(\boldsymbol{r}, \boldsymbol{v}_2 - \boldsymbol{v}_1) && (6.21) \\ &= \int \mathrm{d}^3 v_{\mathrm{rel}} P_{\boldsymbol{r},\mathrm{rel}}(\boldsymbol{v}_{\mathrm{rel}}) f(\boldsymbol{r}, \boldsymbol{v}_{\mathrm{rel}}) \\ &\equiv \int \mathrm{d}v_{\mathrm{rel}} \, p_{\boldsymbol{r},\mathrm{rel}}(v_{\mathrm{rel}}) f(\boldsymbol{r}, v_{\mathrm{rel}}) && (6.22) \end{aligned}$$

We implicitely assumed that center of mass velocities are sufficiently small so that the non-relativistic analysis is valid and by defining

$$P_{\boldsymbol{r},\mathrm{rel}}(\boldsymbol{v}_{\mathrm{rel}}) \equiv \int \mathrm{d}^3 v_{\mathrm{CM}} P_{\boldsymbol{r}}(\boldsymbol{v}_{\mathrm{CM}} + \boldsymbol{v}_{\mathrm{rel}}/2) P_{\boldsymbol{r}}(\boldsymbol{v}_{\mathrm{CM}} - \boldsymbol{v}_{\mathrm{rel}}/2) , \tag{6.23}$$

$$p_{\boldsymbol{r},\mathrm{rel}}(v_{\mathrm{rel}}) = 4\pi v_{\mathrm{rel}}^2 P_{\boldsymbol{r},\mathrm{rel}}(v_{\mathrm{rel}}) , \tag{6.24}$$

we are left with just one integral (6.22) out of the original six in eq. (6.21) if ergodicity ($p_{\boldsymbol{r}}(\boldsymbol{v})$ is isotropic in velocity space) is assumed. Otherwise, a $v_{\rm CM}$-dependent red shift factor would have to be taken into account[5] for E_γ.

By comparing formula (6.20) with (3.1), we immediately notice that the useful factorization property encountered for the DM-associated gamma-ray prompt emission (refer to section 3.3) is lost. This in turn means that the DM annihilation cross section spectral features will be distorted by the non-trivial velocity distribution in the gamma-ray flux.

6.3.1 Velocity distributions

Despite the N-body simulations great successes in describing the spatial structure of the DM halos in our Universe, more detailed refinements are still needed if one wants to obtain an accurate sample of the DM velocities at all possible positions in the halo. Some studies [144–146] have been however carried out in order to estimate such distribution at the **Sun's position** both numerically and observationally. Creators of the N-body simulation *Via Lactea II* performed in Ref. [144] an analysis of a one billion particle simulation to obtain such estimate while Ref. [145] used Rhapsody [147, 148] and Bolshoi [149] simulations. Ref. [146] in turn fitted galaxy rotation observations with an analytical (*King*) model.

Given a DM spatial profile assumed to bear spherical symmetry and ergodicity, Eddington's formula allows us to obtain the full phase-space distribution function (DF) $F(r,v)=\tilde{F}(\varepsilon)$, with $\varepsilon=v^2/2+\varphi(r)$ (energy per unit mass) and $\varphi(r)$ the gravitational potential. Concretely, after performing a change of variable $\varphi\to r$

$$\tilde{F}(\varepsilon)=\frac{1}{\sqrt{8}\pi^2}\int_\varepsilon^{\varphi_0}\frac{\mathrm{d}\tilde{\varphi}}{\sqrt{\tilde{\varphi}-\varepsilon}}\frac{\mathrm{d}^2\rho_\chi}{\mathrm{d}\tilde{\varphi}^2}\ .$$

For instance, solving this equation for a profile $\rho(r)\propto 1/r^2$ yields to

$$\tilde{F}(\varepsilon)=\frac{\rho(r)}{(2\pi\sigma_0^2)^{3/2}}\exp\left(-\frac{v^2}{2\sigma_0^2}\right)=\rho(r)p_{\rm MB}(v)\ ,$$

where $p_{\rm MB}(v)$ is the Maxwell-Boltzmann distribution with constant velocity dispersion σ_0, which of course can be identified with an r-independent temperature: $\sigma_0^2=kT/m$. This system is known as a *singular isothermal sphere* (SIS) and its associated DF resembles the DM ones (regardless their $r\to 0$ behaviour) at radii close to the scale radius: formally the SIS has a r^{-2} dependence while the "pseudo-isothermal sphere" that has been extensively used to describe the DM halo [1] satisfies $\rho(r)\to\rho_0$ when $r\to 0$.

Application of Eddington's formula to some cases of interest (NFW, Einasto and Burkert DM profiles) were computed in Ref. [150], finding that at radii far away from the scale radius, departures from the Maxwell-Boltzmann are apparent. Nevertheless, the Jeans analysis where the velocity distribution is taken to be maxwellian but with r-dependent dispersion

$$p_r(v)=\frac{1}{(2\pi\sigma_r^2)^{3/2}}\exp\left(-\frac{v^2}{2\sigma_r^2}\right) \tag{6.25}$$

proves to be accurate enough in a wide range of distances. Both methods however overlook non-spherical effects such as substructure and the gravitational potential of baryonic

[5] As discussed in appendix A in the relativistic case it is the Møller velocity the one that is relevant. The change of variables $(\boldsymbol{v}_1,\boldsymbol{v}_2)\to(\boldsymbol{v}_{\rm CM},\boldsymbol{v}_{\rm Møl.})$ is therefore different to the one adopted here.

matter, inducing uncertainties that overshoot the non-gaussianities encountered in the analysis carried out in [150]. We therefore only consider MB distributions in this work. Notice that interestingly for Maxwell-Boltzmann distributions, the associated relative velocity DF (6.23) is also maxwellian with dispersion $\sqrt{2}\sigma_v$.

6.4 Enhanced gamma-ray lines from Kaluza-Klein DM annihilation

From the discussion in the previous section we have learned that for some models there might exist several special situations where enhancement in the annihilation cross section is expected. In this section we will focus on the particular case where the annihilation proceeds into two-body states with one monochromatic gamma-ray photon. In the context of indirect DM searches such processes would give rise to gamma-ray lines and as discussed in chapter 2 they are the smoking-gun signatures for indirect DM searches. If in the model's particle spectrum there are new particles with masses resonating with available center of mass energies of the annihilating DM particles, then signals relevant for indirect DM detection and, particularly, line signals will be enhanced making it more feasible for gamma-ray astronomers to spot them.

We will find that in *Universal Extra Dimensional* (UED) models introduced in section 1.3.1, resonant effects of the Breit-Wigner type might be sizable depending on the UED model's parameters. We shall however particularly focus on the simplest one featuring one orbifold extra dimension for definiteness.

Before going into the details of how the Breit-Wigner resonances in the UED model can affect the relative strength of gamma-ray line signals in the sky, let us generally discuss how the gamma-ray-line flux is affected by such a resonance.

6.4.1 Enhanced gamma-ray line by a Breit-Wigner resonance

In section 3.3 we noticed that in the $v = 0$ approximation, spectral features apparent in the DM annihilation cross section –such as monochromaticity– remain unaltered in the associated gamma-ray flux owing to the factorization property in formula (3.1). As briefly mentioned before, considering a non trivial velocity DF can modify the flux spectrum when compared to the raw spectrum from the annihilation cross section. Of particular interest are monochromatic photons. At the cross section level these are characterized in spectral terms according to $\mathrm{d}N/\,\mathrm{d}E_\gamma = \delta(E_\gamma - \sqrt{s}/2)$, where $\sqrt{s}$ is the center of mass energy of the annihilating DM particles and for simplicity we neglect the mass of the second particle produced in the annihilation. In the $v = 0$ limit, $\sqrt{s} = 2m_\chi$ and the line signal remains monochromatic at the flux level[6] while in the general DF-dependent case the line will be smeared out by the DF[7]:

$$(\sigma_{\rm line} v)\delta(E_\gamma - m_\chi) \to \langle (\sigma_{\rm line} v)\delta(E_\gamma - \sqrt{s(v)}/2)\rangle_v \ .$$

Let us now consider the case where DM annihilation excites a Breit-Wigner resonance of mass $m_{\rm res}$ and decay width $\Gamma_{\rm res}$. We can decompose the cross section as $\sigma_{\rm line} = \sigma_0 + \sigma_{\rm res}$, with

$$\sigma_{\rm res} \simeq \frac{\tilde{\sigma}_{\rm res}\Gamma^2_{\rm res} m^2_{\rm res}}{(s - m^2_{\rm res})^2 + \Gamma^2_{\rm res} m^2_{\rm res}}$$

[6] Gamma-ray detectors of course do not measure exact monochromaticity but instead very pronnounced features with narrow energy widths determined by the detector's energy resolution.

[7] We will omit henceforth the subscript "res" when referring to relative speeds.

and σ_0 the non-resonant contribution. We assume $\sigma_{\rm res}|_{\sqrt{s}=m_{\rm res}} = \tilde{\sigma}_{\rm res} \gg \sigma_0|_{\sqrt{s}=m_{\rm res}}$ and also that $(m_{\rm res} - 2m_\chi)/m_{\rm res} \ll 1$ so that the non-relativistic approximation is valid ($\sqrt{s} = 2m_\chi$ if $v = 0$). Under such assumptions we can invert eq. (1.4) –Møller's velocity– and write $\sqrt{s}(= 2E_\gamma)$ in terms of v

$$\sqrt{s} \simeq 2m_\chi \left(1 + \frac{1}{8}v^2\right) \ . \tag{6.26}$$

Performing the velocity averaging by means of eq. (6.22) is trivial after making the identification $\delta(E_\gamma - \sqrt{s}/2) \to (4/mv)\delta(v - v_{\rm line})$, where $v_{\rm line} = \sqrt{8}\sqrt{E_\gamma/m_\chi - 1}$ is obtained from eq. (6.26). The gamma-ray line flux (6.20) then reads

$$\frac{{\rm d}\Phi_{\rm res}}{{\rm d}E_\gamma} \simeq \frac{\tilde{J}_{\rm line}(E_\gamma)}{8\pi m_\chi^3}\left[(\sigma_0 v_{\rm line}) + \frac{(\tilde{\sigma}_{\rm res} v_{\rm line})\,\Gamma_{\rm res}^2 m_{\rm res}^2}{(4E_\gamma^2 - m_{\rm res}^2)^2 + \Gamma_{\rm res}^2 m_{\rm res}^2}\right] , \tag{6.27}$$

$$\text{with } \tilde{J}_{\rm line}(E_\gamma) \equiv \frac{1}{\Delta\Omega}\int_{\Delta\Omega}{\rm d}\Omega \int_{\rm l.o.s.}{\rm d}l \int \rho^2(\boldsymbol{r})\frac{p_{\boldsymbol{r},{\rm rel}}(v_{\rm line})}{v_{\rm line}/4} \ . \tag{6.28}$$

Before entering into the concrete case of UED, let us make some general remarks on the previous equation:

1. For the singular isothermal sphere (SIS) introduced in section 6.3.1 the factor $\tilde{J}_{\rm line}$ is proportional to the usual J-factor encountered in the standard $v = 0$ analysis as the DF in such case does not have any r-dependence. For simplicity let us take a velocity distribution of a SIS with most probable speed v_0.

2. We observe that eq. (6.27) contains two multiplicative and competitive terms. The energy dependent part of the first term $\tilde{J}_{\rm line}$ peaks at a certain energy $E_{\rm MB} = m_\chi(1 + v_0^2/8)$ and for larger energies it falls off exponentially. The second one is the Breit-Wigner term which obviously peaks at the energy $E_{\rm res} = m_{\rm res}/2$ but falls off less drastically $\propto E_\gamma^{-4}$.

3. The effect of the resonance is maximal when $E_{\rm res} = E_{\rm MB}$, or equivalently

$$\frac{\Delta m}{m_{\rm res}} \simeq \frac{m_{\rm res} - 2m_\chi}{2m_\chi} = \frac{1}{8}v_0^2 \ . \tag{6.29}$$

4. As a consistency check we can prove that in general –i. e. DM models without the special properties discussed in section 6.1 in astrophysically understood environments (no DM acceleration by gravity)– the $v = 0$ approximation is very good. Namely, the theoretical width of a gamma-ray line due to uncertainties in the velocity DF can be estimated as $\Delta E_{\rm MB}/E_\gamma \approx v_0^2/8$ which for typical DM speed $v_0 \sim 1 \times 10^{-3}$ gives $\Delta E/E_\gamma \sim 10^{-7}$ which is negligible compared to the Doppler shift correction.

6.4.2 Gamma ray flux from Kaluza-Klein DM

Although this section will be mainly concerned with DM from Universal Extra Dimensions, the methodology and the results presented here are quite general. In section 6.2 we found $\sim 10^3$ enhancements in the *minimal* UED model's DM annihilation cross sections for relative speeds of the order of $10^{-1}c$. We pointed out there that even small departures from minimality can, to a great extent, affect the relative speed at which the

resonance becomes important without altering too much the resonance characteristic width.

Let us now compare at the flux level the impact of the $H^{(2)}$ resonance encountered in section 6.2 by using eq. (6.27). We shall henceforth consider generic $H^{(2)}$ resonances from not necessarily minimal UED models. This allows us to keep the mass differences between the resonance and the sum of the initial-state particle masses as a variable. Additionally and as anticipated before, we will simply consider maxwellian velocity distributions (6.25) with no r dependence.

In figure 6.10 we use formula (6.27) to obtain the ratio (flux enhancement) $\Phi_{\rm enh}/\Phi_0$ of the "peak" flux corresponding to the prediction that includes the $H^{(2)}$-resonance term to the flux without a resonance.

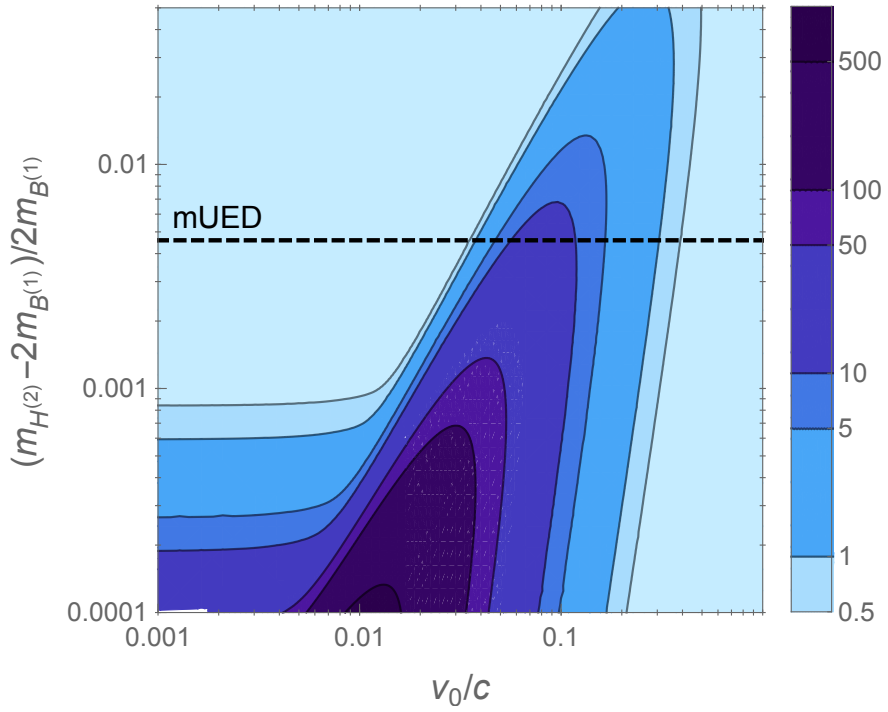

Figure 6.10: Taking the position of the $H^{(2)}$ resonance –parametrized by $(m_{H^{(2)}} - 2m_{B^{(1)}})/2m_{B^{(1)}}$– and the most probable DM velocity v_0 of a MB distribution as variables, we perform a contour plot of the enhancement factor in color scale.

We observe enhancements of more than one order of magnitude in the mUED model (dashed line) for DM velocity dispersions $\sigma_v \gtrsim .05c$. For smaller mass differences the enhancement is more pronounced, boosting the signal up to about a factor of 10^3. Notice that as expected the region where the enhancement is most efficient is defined by eq. (6.29) (straight line with slope 2 in the logarithmic scale of fig. 6.10).

On the other hand, since DM velocity dispersions in our galaxy are of the order of $v \sim 10^{-3}c$, there is little hope of observing this effect on the galactic scale. Even if the difference between the $H^{(2)}$ mass and the sum of the LKP masses is of the order of $10^{-3}m_{H^{(2)}}$ such that the line signal is optimally enhanced, current [151] and next-generation [152] experiments will not be able to easily spot such signal in our galaxy. At larger scales the situation is different, as larger velocity dispersions $v \sim 10^{-2}c$ in

for instance *galaxy clusters* are available. As discussed in chapter 2 galaxy clusters are promising targets for DM searches since enormous boost factors are expected due to their rich substructure hierarchy [153]. Moreover, In cosmological epochs when the temperature was large enough to excite these resonances, their effects also need to be taken into account [140].

6.5 DM acceleration mechanisms

The fact that DM particles do not interact too much makes them poorly capable of being accelerated by other mechanisms than gravity. However, the background gravitational potential (almost fully determined by the DM distribution) does not act as an efficient accelerator: the maximum allowed velocities remain non relativistic as inferred from N-body simulations. Different types of mechanisms, if any, would be necessary for accelerating DM particles in the cosmos. We discuss nextly an example where DM can be strongly accelerated by the gravitational field of a black hole.

6.5.1 Bañados-Silk-West effect

This effect occurs when DM particles that are very close to a rotating supermassive black hole (SMBH) annihilate. Since the trajectories (and velocities) of the interacting particles are affected by the gravitational pull of the SMBH, the center of mass energy of such interaction can be arbitrarily large.

The Bañados-Silk-West (BSW) effect [28] is restricted to a maximally rotating BH. However, it will be instructive to instead consider the also interesting case of a Schwarzschild BH .

According to our assumptions, DM particles are solely influenced by gravity. This means that their trajectories are those of the BH metric geodesics which are parametrized by the energy and angular momentum parameters ϵ and l respectively. We furthermore consider only in-falling geodesics that are at rest at infinity ($\epsilon = 0$).

Since we are interested in the annihilation of the DM particles, we shall consider two geodesics that meet at a given point. Particularly interesting will be the regions that are close to the horizon, as particle acceleration is expected to be optimized there. A careful computation of the center-of-mass energy of two colliding particles at a distance r from the BH yields

$$E^2_{\rm cm} = 2m^2_\chi \frac{r^2(2r - r_S) - l_1 l_2 (r - r_S) - \sqrt{r_S r^2 - l_1^2 (r - r_S)}\sqrt{r_s r^2 - l_2^2 (r - r_S)}}{r^2 (r - r_S)}\,, \tag{6.30}$$

where $r_S = 2GM_{\rm SMBH}$ is the Schwarzschild radius of the BH, m_χ the mass of the DM particle and l_1, l_2 are the angular momentum parameters of the two geodesics. The energy is maximized when $r \to r_S$ and $l_1 = -l_2 = \pm 2 r_S$ and it takes the value $E_{\rm max} = \sqrt{5}(2m_\chi)$.

Figure 6.11 shows the possible center-of-mass energies of colliding particles as a function of the distance to the BH for the Schwarzschild case as for a rotating one. The latter was investigated in Ref. [28], where it was noticed that if the BH is maximally rotating –its angular momentum parameter reaches the critical value $a = r_S$– then, the center-of-mass energy of two particles meeting close to the horizon can be arbitrarily large provided that the angular-momentum parameter of one of the particles is $l = r_S$. This is of course apparent in the left panel of fig. 6.11 (see blue line).

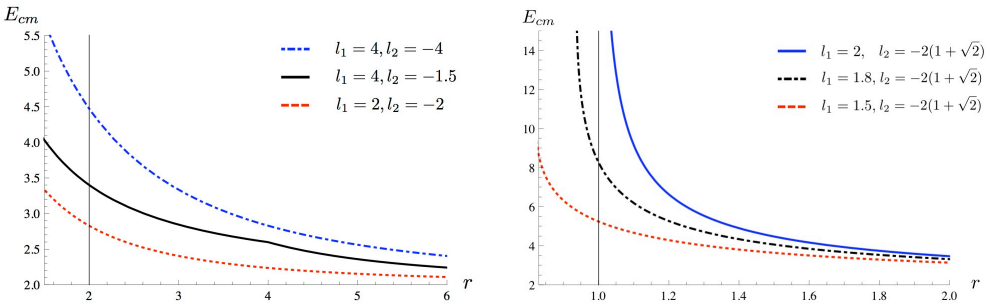

Figure 6.11: Center of Mass energies of two annihilating DM particles close to the horizon of a Schwarzschild black hole (left) and a maximally rotating Kerr black hole (right) [28].

Conclusions

One of the most puzzling enigmas in contemporary science was addressed in this thesis: the origin and nature of non-baryonic Dark Matter (DM). Guided by the successful Λ Cold Dark Matter (ΛCDM) cosmological model, we focused our attention on the phenomenology of a special family of theories for DM. Namely we assumed in this thesis that most of the DM in the Universe consists of Weakly Interacting Massive Particles (WIMPs).

Our studies primarily concentrated on the quantitative description of signals associated with DM in the electromagnetic (EM) spectrum of the sky. Since the WIMPs are expected to emit electromagnetic radiation in the radio and gamma frequency bands as the result of their self-annihilation, we focused on those ranges.

We showed how astronomical gamma ray observations are excellent probes for indirect detection of DM. Spefically, a positive DM signal would allow us to learn about both the spectral and spatial properties of the DM. We also provided a comprehensive overview of the synchrotron radiation in the general astrophysical context and in the context of DM annihilation.

The optical theorem proved useful in confronting the DM interpretation of the line-like 130 GeV excess at the Galactic Center with other signals of phenomenological relevance. This method is based on fundamental principles such as symmetry and unitarity which we also discussed in this thesis. As a spin-off, we derived a number of unprecedented analytical formulas of general applicability.

Non-detection limits of gamma-ray continuum and radio signals associated to DM enabled us to constrain the model building for the 130 GeV gamma-ray line. Complementarily, exclusion limits of charged cosmic-ray antiparticles (antiproton and positron) were considered as well. These proved to be particularly interesting in testing the DM interpretation of the GeV excess. We also included a fairly extensive review of the phenomenology of these messengers, focusing on the DM signals.

By taking into account the effects of the velocity dispersions of the DM distribution in halo, we showed that the spectral gamma ray line signal that is inferred from the annihilation of Kaluza-Klein (KK) DM pairs is enhanced. Since radiative effects needed to be considered, e.g. in order to consistently incorporate effective vertices localized at the orbifold's fixed points, some lengthy calculations were necessary. We were in addition able to correct some formulas previously reported in the literature. Finally, we discussed the interesting possibility that DM gets accelerated in the vicinity of supermassive black holes and showed that the associated annihilation cross section has a comb-like structure.

We seem to be on the verge of hopefully discovering the (microscopic nature of) DM in the next few years. The next generation of experiments searching for DM have a strong potential of being able to make this happen. They will otherwise be able to set stringent constraints on the WIMP annihilation cross sections and life times.

Appendix A

DM injection function

Consider a volume element δV with N DM particles moving at non-relativistic speeds. In the rest frame of one of the N-th particle, the rest of the particles will travel in many directions with velocity vectors $\{\boldsymbol{v}_i\}_{i=1}^{N-1}$. The probability that in a time interval δt the i-th and the N-th particle annihilate with each other is (by definition of the cross section) $\delta\mathcal{P}_{i\leftrightarrow N} = \sigma_{\text{ann}}/\delta A_{\perp\, i} = v_i \delta t \sigma_{\text{ann}}/\delta V$ where $\delta A_{\perp\, i}$ is the differential surface element that is perpendicular to the velocity vector $\boldsymbol{v}_i$. Summing over all $N-1$ particles with which the N-th particle can annihilate yields

$$\delta\mathcal{P}_N = \sum_{i=1}^{N-1} \mathcal{P}_{i\leftrightarrow N} = \frac{N-1}{\delta V}\langle\sigma_{\text{ann.}} v\rangle \delta t \ , \tag{A.1}$$

where the average $\langle\sigma v\rangle$ is defined as $\frac{1}{N-1}\sum \sigma_i v_i$. To obtain the total number of DM annihilations $\mathscr{N}$ within the volume δV we need to add all annihilation probabilities $\delta\mathcal{P}_{i\leftrightarrow j}$ making sure that we do not count twice:

$$\begin{aligned}\delta\mathscr{N} = \sum_{i<j} \delta\mathcal{P}_{i\leftrightarrow j} \times 1 &= \frac{N-1}{\delta V}\langle\sigma_{\text{ann.}} v_{\text{rel.}}\rangle \delta t + \frac{N-2}{\delta V}\langle\sigma_{\text{ann.}} v_{\text{rel.}}\rangle \delta t + \dots \\ &= \frac{(N-1)(N-2)}{2\delta V}\langle\sigma_{\text{ann.}} v_{\text{rel.}}\rangle \delta t \ ,\end{aligned} \tag{A.2}$$

where we transformed eq. (A.1) back to the original frame ($v \to v_{\text{rel.}}$).

In the limit of large N, the total number of annihilations $\delta\mathscr{N}$ in time interval δt within a volume δV is given by

$$\delta\mathscr{N} = \frac{1}{2} n_\chi^2 \langle\sigma_{\text{ann.}} v\rangle \delta V \delta t \ , \tag{A.3}$$

where $n_\chi = N/\delta V$ is the number density of DM particles in the volume element.

A.1 Møller velocity

In deriving eq. (A.3) we made two simplifying assumptions that we can now examine. First, we assumed that the system is non-relativistic so that we could use the simple Galilean transformation rule $v \to v_{\text{rel.}}$. We can relax this assumption by noticing that the annihilation rate density

$$\Gamma \equiv \frac{\mathrm{d}^2\mathscr{N}}{\mathrm{d}V\,\mathrm{d}t} = \frac{1}{2} n_\chi^2 \langle\sigma_{\text{ann.}} v\rangle \tag{A.4}$$

transforms as a Lorentz scalar ($\mathrm{d}t\,\mathrm{d}V$ is a Lorentz pseudo-scalar). Next, we know that n_χ transforms as the zeroth component of a 4-vector and $\sigma_{\text{ann.}}$ can be defined to transform as a scalar[1]. Under these conditions the covariant realization of the relative speed is the Møller velocity [39]

$$v_{\text{Møll}} = \frac{\sqrt{(p_1 \cdot p_2)^2 - m_\chi^4}}{E_1 E_2} = [\|\boldsymbol{v}_1 - \boldsymbol{v}_2\|^2 - \|\boldsymbol{v}_1 \times \boldsymbol{v}_2\|^2]^{1/2} \ , \tag{A.5}$$

as already introduced in eq. (1.4) of chapter 1.

A.2 DM particle-antiparticle annihilations

The second assumption was that the DM "self"-annihilates, i.e. the DM antiparticle is the DM particle itself. By relaxing this condition and introducing N and $\bar{N}$ as the number of DM particles and antiparticles in our equations, the prefecture $N-1$ in formula (A.1) is changed to $\bar{N}$ and (A.2) becomes

$$\delta\bar{\mathscr{N}} = \frac{N}{\delta V}\frac{\bar{N}}{\delta V}\langle\sigma_{\text{ann.}} v_{\text{rel.}}\rangle \delta t \delta V \simeq \frac{1}{4} n_{\chi+\bar{\chi}}^2 \langle\sigma_{\text{ann.}} v_{\text{rel.}}\rangle \delta t \delta V \ , \tag{A.6}$$

where in the last step we assumed that there are as much DM antiparticles as DM particles. In practice, this means that we consider when DM models where the DM antiparticle is **not** the DM particle itself, we have to include an extra factor of $1/2$ in eq. (A.4).

A.3 Particle yields

Since we will mostly be interested in the production rate of photons and electrons per unit particle energy, we introduce the particle yield function

$$Y(E) = \frac{1}{\sigma_{\text{ann.}}^{\text{TOT}}}\frac{\mathrm{d}\sigma_{\text{ann.}}}{\mathrm{d}E} = \sum_c \text{BR}_c \left(\frac{\mathrm{d}N}{\mathrm{d}E}\right)_c \ ,$$

where E is the energy of the messenger of interest (gamma ray, electron/positron, etc.) and the index c counts all possible annihilation channels of the DM. The injection (source) function Q is obtained by simply multiplying the yield with the rate density (A.4):

$$Q = \frac{1}{2m_\chi^2}\rho_\chi^2 \langle\sigma_{\text{ann.}} v\rangle \sum_c \text{BR}_c \left(\frac{\mathrm{d}N}{\mathrm{d}E}\right)_c \ . \tag{A.7}$$

As a final comment, notice that in arriving to the previous formula, we assumed that the mass density is related to the number density by $\rho_\chi = m_\chi n_\chi$. In a relativistic treatment this assumption is no longer appropriate. As mentioned before, under Lorentz transformations, number densities n_χ transform as zeroth components of 4-vectors while ρ_χ transforms an energy density: first diagonal component of a rank-two Lorentz tensor.

[1]The cross section can also be defined in such a way that it transforms as an area. See textbook [40] for such an alternative definition.

Appendix B

Radio flux technicalities

B.1 Emitted vs. "Observed" power

Eq. 4.12 very accurately determines the emitted **energy** $\mathrm{d}W$ of waves with frequencies in the range ω and $\omega + \mathrm{d}\omega$ **in one cycle** from synchrotron radiation of an electron in an uniform magnetic field. In order to transform this into a power, we naïvely divide $\mathrm{d}W$ by one period T:

$$\mathrm{d}P_e = \frac{1}{T}\,\mathrm{d}W = \frac{\omega_B}{2\pi}\,\mathrm{d}W \ ,$$

such that

$$\frac{\mathrm{d}P_e}{\mathrm{d}\omega} = \frac{\sqrt{3}e^3 B\sin\alpha}{2\pi mc^2} F\left(\frac{\omega}{\omega_c \sin\alpha}\right) \ . \tag{B.1}$$

This formula however overlooks the fact that the source of the radiation pulses is in average traveling in a well defined direction (along the magnetic field lines). The time of arrival of the pulses at an observation point at infinity is thus Doppler shifted. Figure B.1 captures this phenomenon in a graphic way. The observed period T_A thus satisfies

$$cT_A = cT(1 - \beta_\parallel \cos\alpha) \simeq cT(1 - \cos^2\alpha) = cT\sin^2\alpha$$

while the actual observed power is [19]

$$\frac{\mathrm{d}P_o}{\mathrm{d}\omega} = \frac{\sqrt{3}e^3 B}{2\pi mc^2 \sin\alpha} F\left(\frac{\omega}{\omega_c \sin\alpha}\right) \ . \tag{B.2}$$

We notice in passing that by construction the total observed power $P = \int \mathrm{d}\omega \frac{\mathrm{d}P}{\mathrm{d}\omega}$ is independent of the pitch angle.

Along this work we however used our naïve formula (B.1) for the power rather than the "correct" one (B.2). This is because when we make predictions of the synchrotron radiation emitted by a large ensamble of cosmic-ray electrons in an astrophysical set up, we need to take into account statistical effects. Typical synchrotron-radiation-emitting regions in astrophyics are localized and move with only moderate velocities. This in turn means that in stationary conditions there are on average as many radiating particles moving towards the observer –emitting pulses with contracted period $(1 - \cos^2\alpha)T$– as "invisible" particles moving away. The latter emit pulses with dilated period $(1 + \cos^2\alpha)T$. Since their emission region (half cone) is directed opposite to the observer, he will not be able to track them. We conclude that for an average particle only a fraction (see problem 6.3 in the classical textbook [21])

$$f = \frac{1 - \cos^2\alpha}{1 - \cos^2\alpha + 1 + \cos^2\alpha} = \frac{1}{2}\sin^2\alpha$$

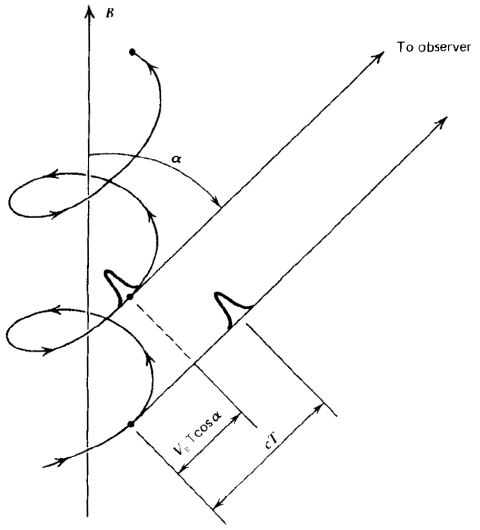

Figure B.1: Illustration of how the Doppler effect affects the amount of "observed" power respect to the "emitted". Image from [21].

of the time will emit observable synchrotron radiation in such a way that the average power per unit frequency is indeed given by (B.1) and (4.13).

B.2 Cone Integration

Let us consider a half-cone with an aperture angle γ_0 which axis is defined by the line that joins the GC and the Solar System as depicted in the picture below. We consider spherical coordinates around the GC and divide the integration volume into three regions. Since we are assuming spherical symmetry, the angular variables can be integrated out: let $f(r)$ be an arbitrary function and let us compute its integral in this volume; then, for regions (I) and (III) we have

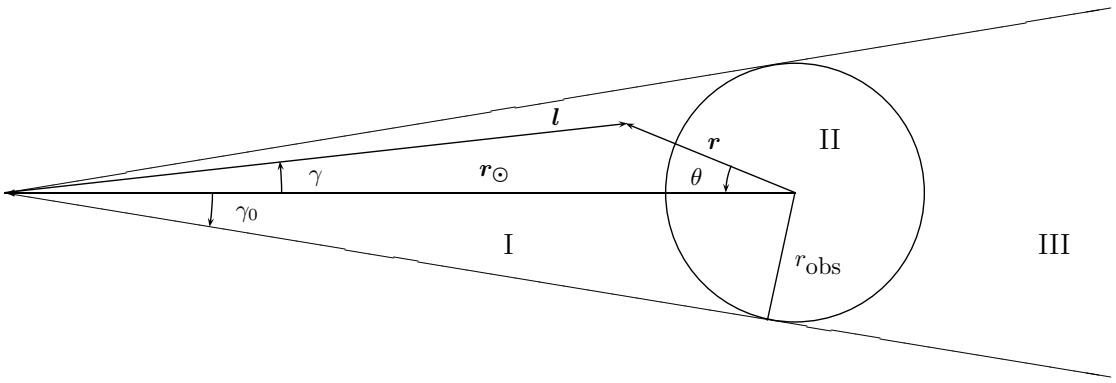

Figure B.2: Integration regions

$$J_{\rm I} = \int_{\rm I} f(r)dV = 2\pi \int_{r_{\rm obs}}^{r_\odot} r^2 f(r) \int_0^{\arcsin\frac{r_{\rm obs}}{r}-\gamma_0} \sin\theta \,{\rm d}\theta \,{\rm d}r \ , \tag{B.3}$$

$$J_{\rm III} = \int_{\rm III} f(r)dV = 2\pi \int_{r_{\rm obs}}^{\infty} r^2 f(r) \int_{\pi-\arcsin\frac{r_{\rm obs}}{r}-\gamma_0}^{\pi} \sin\theta \,{\rm d}\theta \,{\rm d}r \ , \tag{B.4}$$

where $r_{\rm obs} \equiv r_\odot \sin\gamma_0 \approx r_\odot \gamma_0 \approx 0.14\,{\rm pc}$. Integration over θ for $J_{\rm I}$ (eq. B.3) yields

$$\begin{aligned}\int_0^{\arcsin\frac{r_{\rm obs}}{r}-\gamma_0} \sin\theta\,{\rm d}\theta &= 1-\cos\left(\arcsin\frac{r_{\rm obs}}{r}-\gamma_0\right)\\ &= 1-\sqrt{1-\left(\frac{r_{\rm obs}}{r}\right)^2}\cos\gamma_0-\frac{r_{\rm obs}}{r}\sin\gamma_0\\ &\approx 1-\sqrt{1-\left(\frac{r_{\rm obs}}{r}\right)^2}\,.\end{aligned}$$

Similarly, for $J_{\rm III}$

$$\begin{aligned}\int_{\pi-\arcsin\frac{r_{\rm obs}}{r}-\gamma_0}^{\pi} \sin\theta\,{\rm d}\theta &= 1-\cos\gamma_0\sqrt{1-\left(\frac{r_{\rm obs}}{r}\right)^2}+\frac{r_{\rm obs}}{r}\sin\gamma_0\\ &\approx \int_0^{\arcsin\frac{r_{\rm obs}}{r}-\gamma_0}\sin\theta\,{\rm d}\theta\,.\end{aligned}$$

Therefore, assuming $f(r\gtrsim r_\odot)\to 0$, $\gamma_0 \ll 1$, etc.

$$J_{\rm I}\approx J_{\rm III} = 2\pi\int_{r_{\rm obs}}^\infty r^2\left(1-\sqrt{1-\left(\frac{r_{\rm obs}}{r}\right)^2}\right)f(r)\,{\rm d}r\,.$$

Finally, angular integration on region (II) is straightforward:

$$J_{\rm II} = 4\pi\int_0^{r_{\rm obs}} r^2 f(r)\,{\rm d}r\,. \tag{B.5}$$

The final expression for $J = J_{\rm I}+J_{\rm II}+J_{\rm III}$ is hence

$$J = 4\pi\int_0^\infty r^2\underbrace{\left(1-\Theta(r-r_{\rm obs})\sqrt{1-\frac{r_{\rm obs}^2}{r^2}}\right)}_{1-\lambda(r)}f(r)\,{\rm d}r+O(\gamma_0)\,, \tag{B.6}$$

and eq. (4.50) becomes

$$\nu F_\nu = \frac{\langle\sigma v\rangle}{2M_\chi^2}\int_0^\infty {\rm d}r r^2(1-\lambda(r))E_\nu(r)\rho_\chi^2(r)N_e[E_\nu(r)]\,. \tag{B.7}$$

Appendix C

The optical theorem

C.1 Optical theorem for angular momentum states

In this section we shall prove that if CP symmetry (or equivalently time reversal symmetry owing to the CPT theorem) is not violated in a process described by the matrix T, then its matrix elements in helicity and in the partial wave basis are symmetric.

First note that the defining property of the time-reversal symmetry is

$$\langle cd|\mathcal{T}T\mathcal{T}|ab\rangle = \langle ab|T|cd\rangle \ , \tag{C.1}$$

where we denoted the time-reversal operator as $\mathcal{T}$.

Second, decomposition of two-particle states with definite angular momentum (both helicity states and partial waves) in states with definite linear momentum in terms of the Wigner functions allows one to show that for such states [120]

$$\mathcal{T}|J,M\rangle = (-1)^{J-M}|J,-M\rangle \ , \tag{C.2}$$

where we omitted helicity or spin and orbital angular momenta labels.

The final argument uses the fact that conservation of angular momentum (Lorentz symmetry) implies

$$\langle J',-M'|\mathcal{T}|J,-M\rangle = \langle J',M'|R_z(-\pi)\mathcal{T}R_z(\pi)|J,M\rangle = \langle J',M'|\mathcal{T}|J,M\rangle \ , \tag{C.3}$$

where we implicitely used conservation of angular momentum ($M'=M$, $J'=J$) in the last step.

From eq. (C.3) follows

$$\langle cd|\mathcal{T}T\mathcal{T}|ab\rangle = \langle cd|T|ab\rangle \ , \tag{C.4}$$

which combined with eq. (C.1) results in the claimed statement. Namely,

$$\langle cd|T|ab\rangle = \langle ab|T|cd\rangle \ . \tag{C.5}$$

C.2 Computation of amplitudes

Using the selection rules that the Lorentz and CP symmetries set on our states of interest, we can now write formulas for the tree-level $|f\rangle \to |X\rangle$ amplitudes in terms of corresponding helicity amplitudes which, in turn, will be derived in terms of plane wave amplitudes. These are calculated by means of the Feynman rules.

The rest of this section concerns the calculation of amplitudes $\langle X|T|f\rangle$ in a case-to-case basis, where the set of initial ($|f\rangle$) and final ($|X\rangle$) states are the ones derived in the previous section. We denote the helicity amplitudes as $\mathcal{M}^h_{\lambda_\gamma;\lambda_X}$, where it is understood that

$$\mathcal{M}^h_{\lambda_f;\lambda_X} = \langle J=0,\ M=0,\ \lambda_1=\lambda_X,\ \lambda_2=\lambda_X|T|J=0,\ M=0,\ \lambda_1=\lambda_f,\ \lambda_2=\lambda_f\rangle\ .$$

Having clarified the notation, we show below expressions for the amplitudes of interest in terms of their helicity counterparts:

- CP-even photon annihilation into fermions (Scalar DM)

$$\langle X_S^{1/2}|T|f_S\rangle = -\frac{1}{2}(\mathcal{M}^h_{1;1/2} + \mathcal{M}^h_{-1;1/2} + \mathcal{M}^h_{1;-1/2} + \mathcal{M}^h_{-1;-1/2})\ . \tag{C.6}$$

- Partial wave components of CP-even photon annihilation into W bosons (Scalar DM)

$$\langle L=0,\ S=0|T|f_S\rangle = \tfrac{1}{\sqrt{6}}(\mathcal{M}^h_{1;1}+\mathcal{M}^h_{-1;1}-\mathcal{M}^h_{1;0}-\mathcal{M}^h_{-1;0}+\mathcal{M}^h_{1;-1}+\mathcal{M}^h_{-1;-1})\ ; \tag{C.7}$$

$$\langle L=2,\ S=2|T|f_S\rangle = \tfrac{1}{\sqrt{12}}(\mathcal{M}^h_{1;1}+\mathcal{M}^h_{-1;1}+2\mathcal{M}^h_{1;0}+2\mathcal{M}^h_{-1;0}+\mathcal{M}^h_{1;-1}+\mathcal{M}^h_{-1;-1})\ . \tag{C.8}$$

- Transverse and longitudinal components of CP-even photon annihilation into W bosons (Scalar DM)

$$\langle t|T|f_S\rangle = \frac{1}{2}(\mathcal{M}^h_{1;1}+\mathcal{M}^h_{-1;1}+\mathcal{M}^h_{1;-1}+\mathcal{M}^h_{-1;-1})\ ; \tag{C.9}$$

$$\langle X|T|f_S\rangle = \frac{1}{\sqrt{2}}(\mathcal{M}^h_{1;0}+\mathcal{M}^h_{-1;0})\ . \tag{C.10}$$

- CP-odd photon annihilation into fermions (Majorana DM)

$$\langle X_M^{1/2}|T|f_M\rangle = -\frac{1}{2}(\mathcal{M}^h_{1;1/2} - \mathcal{M}^h_{-1;1/2} - \mathcal{M}^h_{1;-1/2} + \mathcal{M}^h_{-1;-1/2})\ . \tag{C.11}$$

- CP-odd photon annihilation into W bosons (Majorana DM)

$$\langle X_M^{1}|T|f_M\rangle = \frac{1}{2}(\mathcal{M}^h_{1;1} - \mathcal{M}^h_{-1;1} - \mathcal{M}^h_{1;-1} + \mathcal{M}^h_{-1;-1})\ . \tag{C.12}$$

C.3 Calculation of helicity amplitudes

Our next task consists in writing the helicity amplitudes in terms of plane waves with spins pointing in the direction of motion. We begin by performing such decomposition on the states, i.e.

$$|J,M,\lambda_1,\lambda_2\rangle = \sqrt{\frac{2J+1}{4\pi}}\int \mathrm{d}^2\hat{\boldsymbol{k}}' d^J_{M,\lambda}(\theta')\,\mathrm{e}^{-i(M-\lambda)\varphi'}\,|\hat{\boldsymbol{k}}';\lambda_1,\lambda_2\rangle\ ,$$

where $\lambda \equiv \lambda_1 - \lambda_2$ and (θ',φ') are the angles defining $\hat{\boldsymbol{k}}'$ respect to some arbitrary cartesian system of coordinates. The functions $d^J_{M,\lambda}(\theta')$ are defined in Ref. [120].

The fact that $J=0$ and, consequently $\lambda=0$, implies that

$$|J=0,M=0,\lambda_1=\lambda_0,\lambda_2=\lambda_0\rangle = \int \frac{\mathrm{d}^2\hat{\boldsymbol{k}}'}{\sqrt{4\pi}}|\hat{\boldsymbol{k}}';\lambda_0,\lambda_0\rangle\ , \tag{C.13}$$

Notice that we are using a convention such that $d^0_{0,0} = 1$. Therefore, we may write

$$\mathcal{M}^h_{\lambda_f;\lambda_I} = \int \frac{\mathrm{d}^2\hat{\boldsymbol{k}}'}{\sqrt{4\pi}} \langle J=0, M=0, \lambda_I, \lambda_I | T | \hat{\boldsymbol{k}}'; \lambda_f, \lambda_f \rangle \ .$$

Owing to spherical symmetry of the state $|J=0, M=0, \lambda_X, \lambda_X\rangle$ and rotational invariance of the interaction, we see that if $U_{\hat{\boldsymbol{k}}'}$ is some unitary rotation that transforms the state $|\hat{\boldsymbol{z}}; \lambda_f, \lambda_f\rangle$ into $|\hat{\boldsymbol{k}}'; \lambda_f, \lambda_f\rangle$, then

$$\begin{aligned}\langle J=0, M=0, \lambda_X, \lambda_X | T | \hat{\boldsymbol{k}}'; \lambda_f, \lambda_f \rangle &= \langle \lambda_X, \lambda_I | T U_{\hat{\boldsymbol{k}}'} | \hat{\boldsymbol{z}}; \lambda_f, \lambda_f \rangle \\ &= \langle \lambda_X, \lambda_X | U_{\hat{\boldsymbol{k}}'} T | \hat{\boldsymbol{z}}; \lambda_f, \lambda_f \rangle = \langle \lambda_X, \lambda_X | T | \hat{\boldsymbol{z}}; \lambda_f, \lambda_f \rangle \ .\end{aligned}$$

Therefore,

$$\mathcal{M}^h_{\lambda_\gamma;\lambda_X} = \sqrt{4\pi} \langle J=0, M=0, \lambda_X, \lambda_X | T | \hat{\boldsymbol{z}}; \lambda_f, \lambda_f \rangle = \int \mathrm{d}^2\hat{\boldsymbol{p}} \langle \hat{\boldsymbol{p}}; \lambda_X, \lambda_X | T | \hat{\boldsymbol{z}}; \lambda_f, \lambda_f \rangle \ .$$

In the last step we used the dual form of eq. (C.13). We can make one further simplification by using the fact that the projection of the total angular momentum in the z direction of the state $|\hat{\boldsymbol{z}}; \lambda_\gamma, \lambda_\gamma\rangle$ is zero and convincing ourselves that the integrand does not depend on the azimuthal angle. Integrating out this angle we obtain

$$\mathcal{M}^h_{\lambda_f;\lambda_X} = 2\pi \int_0^\pi \mathcal{M}_{\lambda_f;\lambda_X}(\theta) \sin\theta \, \mathrm{d}\theta \ . \tag{C.14}$$

$\mathcal{M}_{\lambda_f;\lambda_X}(\theta)$ is the Feynman amplitude for two photons with equal helicities and opposite momenta that annihilate into some pair of charged particles with opposite spins parallel to their linear momenta, θ being the angle between the different momenta/helicities.

C.4 Final expressions

With the machinery just discussed, we will be able to derive in a fairly simple way the set of amplitude that interests us. Notice that up to this point, apart from the symmetry considerations, we have not specified details about any interaction whatsoever. This means that our analysis can be applied generally.

In order to obtain kinematical expressions, we need of course to know the details of the interactions and compute, by means of the Feynman rules, amplitudes $\mathcal{M}_{\lambda_f;\lambda_I}(\theta)$. Since in eqs. (C.6-C.12) it is the bare helicity amplitudes the ones at play, extra caution must be paid when using the Feynman rules and choosing polarization vectors, spinors, etc as overall signs, phases in the amplitudes *do* matter.

Taking all the aforementioned subtleties into account, the Feynman amplitudes for $\gamma\gamma$ and γZ annihilation into fermions and W bosons are:

$$\mathcal{M}^{\gamma\gamma\to\bar{f}f}_{\lambda_f;\lambda_{1/2}}(\theta) = \frac{2(eQ)^2(\beta + 2\lambda_{1/2}\lambda_f)}{\gamma(1-\beta^2\cos^2\theta)} \ ,$$

$$\begin{aligned}\mathcal{M}^{\gamma Z\to\bar{f}f}_{\lambda_f;\lambda_{1/2}}(\theta) = \tfrac{geQ}{\gamma[1-(m_Z/2\gamma m_f)^2]\cos\theta_W} \frac{1}{1-\beta^2\cos^2\theta} \Big(C_V^f \Big[(1-(m_Z/2\gamma m_f)^2\cos^2\theta)\beta + \\ + [1-(m_Z/2\gamma m_f)^2] 2\lambda_{1/2}\lambda_f \Big] + \lambda_f C_A^f (\beta + 2\lambda_{1/2}\lambda_f)[1-(m_Z/2\gamma m_f)^2]\cos\theta \Big) \ ,\end{aligned}$$

$$\mathcal{M}^{\gamma\gamma\to W^+W^-}_{\lambda_f;\lambda_W}(\theta) = \frac{2e^2(2\lambda_W^2 + 2\lambda_W\lambda_f\beta - \gamma^{-2})}{(1-\beta^2\cos^2\theta)} \ ,$$

$$\mathcal{M}^{\gamma Z\to W^+W^-}_{\lambda_f;\lambda_W}(\theta) = \frac{2eg\cos\theta_W(2\lambda_W^2+2\lambda_W\lambda_f\beta-\gamma^{-2})}{(1-\beta^2\cos^2\theta)} \ ;$$

where β is the velocity in natural units of the outgoing particles as measured in the center of mass frame, and $\gamma=(1-\beta^2)^{-1/2}$.

Integration over θ is straightforward:

$$\int_0^\pi \frac{\sin\theta\,\mathrm{d}\theta}{1-\beta^2\cos^2\theta} = \frac{1}{\beta}\int_{-\beta}^{\beta}\frac{\mathrm{d}x}{1-x^2} = \frac{1}{\beta}\ln\left(\frac{1+\beta}{1-\beta}\right) = \frac{2}{\beta}\tanh^{-1}\beta \ ,$$
$$\int_0^\pi \frac{\sin\theta\cos\theta\,\mathrm{d}\theta}{1-\beta^2\cos^2\theta} = 0 \ , \ \int_0^\pi \frac{\sin\theta\cos\theta\,\mathrm{d}\theta}{1-\beta^2\cos^2\theta} = \frac{2}{\beta^2}\left(\frac{\tanh^{-1}\beta}{\beta}-1\right) \ ,$$

leading to

$$\mathcal{M}^h_{\gamma\gamma\to\bar{f}f} = 8\pi(eQ)^2(\beta+2\lambda_{1/2}\lambda_\gamma)\frac{\tanh^{-1}\beta}{\gamma\beta} \ , \tag{C.15}$$

$$\mathcal{M}^h_{\gamma Z\to\bar{f}f} = \frac{4\pi geQ((T_3)_L-2\sin\theta_W Q)}{\gamma\beta\cos\theta_W}\left[\left(\frac{\beta}{1-(m_Z/2\gamma m_f)^2}+2\lambda_{1/2}\lambda_\gamma\right)\tanh^{-1}\beta- \right.$$
$$\left. -\frac{(m_Z/2\gamma m_f)^2}{1-(m_Z/2\gamma m_f)^2}\left(\frac{\tanh^{-1}\beta}{\beta}-1\right)\right] \ , \tag{C.16}$$

$$\mathcal{M}^h_{\gamma\gamma\to W^+W^-} = 8\pi e^2(2\lambda_W^2+2\lambda_W\lambda_f\beta-\gamma^{-2})\frac{\tanh^{-1}\beta}{\beta} \ , \tag{C.17}$$

$$\mathcal{M}^h_{\gamma Z\to W^+W^-} = 8\pi ge\cos\theta_W(2\lambda_W^2+2\lambda_W\lambda_f\beta-\gamma^{-2})\frac{\tanh^{-1}\beta}{\beta} \ . \tag{C.18}$$

The last step consists of just plugging the amplitudes (C.15) and (C.18) into eqs. (C.6-C.12). The final expressions for the amplitudes are sorted according to the type of DM particle and the different f annihilation channels.

Scalar DM

- $\gamma\gamma$ annihilation into fermions

$$\langle X_S^{1/2}|T|f_S\rangle = -\tfrac{1}{2}\left(8\pi(eQ)^2\tfrac{\tanh^{-1}\beta}{\gamma\beta}\right)[(1+\beta)+(-1+\beta)+(-1+\beta)+(1+\beta)] =$$
$$= -\frac{16\pi(eQ)^2}{\gamma}\tanh^{-1}\beta \ . \tag{C.19}$$

- γZ annihilation into fermions

$$\langle X_S^{1/2}|T|f_S\rangle = -\frac{4\pi geQ((T_3)_L-2\sin\theta_W Q)}{\gamma\beta\cos\theta_W}\Big[(\beta/\beta_f+1+\beta/\beta_f-1)\tanh^{-1}\beta- \Big.$$
$$\Big. -\frac{2(m_Z/2\gamma m_f)^2}{\beta_f}\left(\frac{\tanh^{-1}\beta}{\beta}-1\right)\Big] = \tag{C.20}$$
$$= -\tfrac{8\pi geQ((T_3)_L-2\sin\theta_W Q)}{\gamma\beta\beta_f\cos\theta_W}\left[\beta\tanh^{-1}\beta-\left(\frac{m_Z}{2m_\chi}\right)^2\left(\frac{\tanh^{-1}\beta}{\beta}-1\right)\right] \ .$$

- Annihilation into W bosons (partial waves)

$$\begin{aligned}\langle L=0,S=0|T|f_S\rangle &= \frac{1}{\sqrt{6}}\left(8\pi e^2\frac{\tanh^{-1}\beta}{\beta}\right)2[(2+2\beta-\gamma^{-2})+ \\ &\quad +\gamma^{-2}+(2-2\beta-\gamma^{-2})] \\ &= \frac{16\pi}{\sqrt{6}}(4-\gamma^{-2})e^2\frac{\tanh^{-1}\beta}{\beta}=\sqrt{\frac{2}{3}}(3+\beta^2)8\pi e^2\frac{\tanh^{-1}\beta}{\beta}\ ,\end{aligned} \tag{C.21}$$

$$\begin{aligned}\langle L=2,S=2|T|f_S\rangle &= \frac{1}{\sqrt{12}}\left(8\pi e^2\frac{\tanh^{-1}\beta}{\beta}\right)2[(2+2\beta-\gamma^{-2})- \\ &\quad -2\gamma^{-2}+(2-2\beta-\gamma^{-2})] \\ &= \frac{32\pi}{\sqrt{3}}(1-\gamma^{-2})e^2\frac{\tanh^{-1}\beta}{\beta}=\frac{32\pi}{\sqrt{3}}e^2\beta\tanh^{-1}\beta\ .\end{aligned} \tag{C.22}$$

- Annihilation into W bosons (transverse and longitudinal components)

$$\begin{aligned}\langle t|T|f_S\rangle &= \frac{1}{2}\left(8\pi e^2\frac{\tanh^{-1}\beta}{\beta}\right)2[(2+2\beta-\gamma^{-2})+(2-2\beta-\gamma^{-2})= \\ &= 16\pi(2-\gamma^{-2})e^2\frac{\tanh^{-1}\beta}{\beta}=16\pi(1+\beta^2)e^2\frac{\tanh^{-1}\beta}{\beta}\ ,\end{aligned} \tag{C.23}$$

$$\langle l|T|f_S\rangle = \frac{1}{\sqrt{2}}\left(8\pi e^2\frac{\tanh^{-1}\beta}{\beta}\right)2(-\gamma^{-2})=-8\sqrt{2}\pi e^2\frac{\tanh^{-1}\beta}{\gamma^2\beta}\ . \tag{C.24}$$

Majorana DM

- $\gamma\gamma$ annihilation into fermions

$$\begin{aligned}\langle I_M^{1/2}|T|f_M\rangle &= -\frac{1}{2}\left(8\pi(eQ)^2\frac{\tanh^{-1}\beta}{\gamma\beta}\right)2[(1+\beta)-(-1+\beta)]= \\ &= -16\pi(eQ)^2\frac{\tanh^{-1}\beta}{\gamma\beta}\ .\end{aligned} \tag{C.25}$$

- γZ annihilation into fermions

$$\begin{aligned}\langle I_S^{1/2}|T|f_S\rangle &= -\frac{4\pi geQ((T_3)_L-2\sin\theta_W Q)}{\gamma\beta\cos\theta_W}(\beta/\beta_f+1-\beta/\beta_f+1)\tanh^{-1}\beta \\ &= -\frac{8\pi geQ((T_3)_L-2\sin\theta_W Q)}{\cos\theta_W}\frac{\tanh^{-1}\beta}{\gamma\beta}\ .\end{aligned} \tag{C.26}$$

- Annihilation into W bosons

$$\begin{aligned}\langle I_M^1|T|f_M\rangle &= \frac{1}{2}\left(8\pi e^2\frac{\tanh^{-1}\beta}{\beta}\right)2[(2+2\beta-\gamma^{-2})-(2-2\beta-\gamma^{-2})]= \\ &= 32\pi e^2\tanh^{-1}\beta\ .\end{aligned} \tag{C.27}$$

Appendix D

Effective vertices in the UED model

D.1 Annihilation amplitudes

In this Appendix, we compute of the relevant amplitudes describing the resonant annihilation of LKP pairs discussed in chapter 6. The diagrams in fig. 6.6 can compactly be written as

$$i\mathcal{A}_{\rm V} = \epsilon_1^\mu \epsilon_2^\nu L_{{\rm V}\mu\nu}^\rho \frac{-\eta_{\rho\sigma} + \frac{P_\rho P_\sigma}{M_{\rm V}^2}}{s - M_{\rm V}^2 + iM_{\rm V}\Gamma_{\rm V}} R_{{\rm V}\alpha}^\sigma \epsilon_\gamma^\alpha \ , \tag{D.1}$$

$$i\mathcal{A}_{\rm S} = \epsilon_1^\mu \epsilon_2^\nu L_{{\rm S}\mu\nu} \frac{1}{s - M_{\rm S}^2 + iM_{\rm S}\Gamma_{\rm S}} R_{{\rm S}\alpha\beta} \epsilon_\gamma^\alpha \epsilon_Z^\beta \ , \tag{D.2}$$

where V and S stand for vector ($B^{(2)}$, $A_3^{(2)}$) and scalar ($H^{(2)}$, $a_0^{(2)}$) resonances respectively. The tensors $L_{V,S}$, $R_{V,S}$ encode the physical information of the left and right blobs of the diagrams. In the following, we will focus our discussion on these tensors in a final-state-to-final-state basis.

D.1.1 $B^{(1)}B^{(1)} \to \gamma\gamma$

The Feynman diagram for this process is

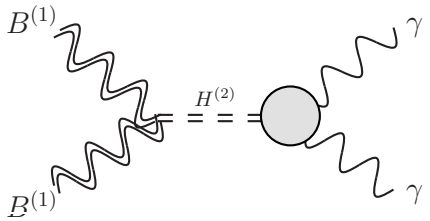

where in this case $L_{\mu\nu} = ig_{B^{(1)}B^{(1)}H^{(2)}}\eta_{\mu\nu} = i(g'^2 v/2)\eta_{\mu\nu}$, v is the vacuum expectation value of the Higgs field (do not confuse with the LKPs' relative speed) and the blob on the right-hand-side is the superposition of several triangle Feynman diagrams:

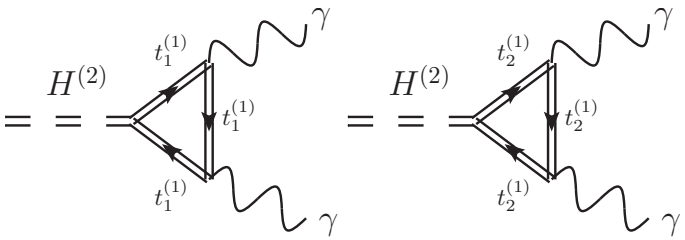

We then decompose the corresponding loop-integrals in terms of Passarino-Veltman functions [154] finding (assuming that $t_1^{(1)}$ and $t_2^{(1)}$ have the same mass)

$$R^{\gamma\gamma}_{H^{(2)}\alpha\beta} = -\frac{\alpha_{\rm em} Q_t^2}{\pi}\frac{4igm_t \sin 2\alpha_t^{(1)}}{m_W}\frac{m_{t^{(1)}}}{s}\times \tag{D.3}$$

$$\times\Big([2-(s-4m^2_{t^{(1)}})\mathrm{C}_0(0,0,s,m^2_{t^{(1)}},m^2_{t^{(1)}},m^2_{t^{(1)}})][s\eta_{\alpha\beta}-2k_{1\alpha}k_{2\beta}-2k_{1\beta}k_{2\alpha}]-$$

$$-4\Big[2\mathrm{B}_0(s,m^2_{t^{(1)}},m^2_{t^{(1)}})-2\mathrm{B}_0(0,m^2_{t^{(1)}},m^2_{t^{(1)}})+s\mathrm{C}_0(0,0,s,m^2_{t^{(1)}},m^2_{t^{(1)}},m^2_{t^{(1)}})\Big]k_{1\alpha}k_{2\beta}\Big)\,.$$

where k_1 and k_2 are the outgoing momenta, $s=(k_1+k_2)^2$, $\alpha_e m \approx 1/128$ is the fine-structure constant at the TeV scale and $Q_t = 2/3$ is the charge of the top-quark. The angle $\alpha^{(1)}$ quantifies the mixing between first KK-level flavour and mass eigenstates; in the mUED case this angle is only non negligible for the KK excitations of the top quark (with $\alpha_t^{(1)} \approx 0.071$). Notice that $R_{H^{(2)}\alpha\beta}$ manifestly satisfies the Ward identities both, namely $k_1^\alpha R_{H^{(2)}\alpha\beta} = k_2^\beta R_{H^{(2)}\alpha\beta} = 0$.

D.1.2 $B^{(1)}B^{(1)} \to Z\gamma$

This process is analog to the one just discussed. Besides a change in the coupling constants we need to take into account that the Z boson is massive and that it has axial-vector couplings. As a consequence, two more diagrams have to be added in the computation:

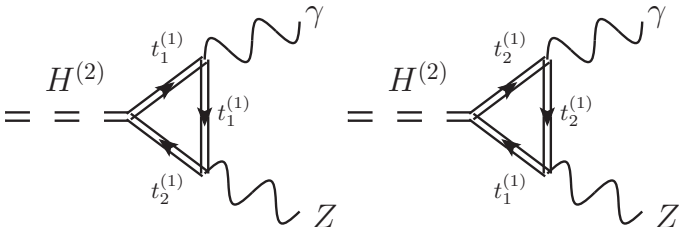

These however cancel out if we assume $m_{t_1^{(1)}} = m_{t_2^{(1)}}$. In total, we find

$$R^{\gamma Z}_{H^{(2)}\alpha\beta} = -\frac{egQ_t}{\pi^2\cos\theta_W}\frac{igm_t}{m_W}\frac{m_{t^{(1)}}\sin 2\alpha_t^{(1)}}{s-m_Z^2}\Big(B\,[(s-m_Z^2)\eta_{\alpha\beta}-2k_{1\beta}k_{2\alpha}]+ \tag{D.4}$$

$$C\,[k_{2\beta}-\frac{2m_Z^2}{s-m_Z^2}k_{1\beta}]k_{1\alpha}\Big)\,, \tag{D.5}$$

where

$$B = \big(Y_{t_L}\sin^2\theta_W - \tfrac{1}{4}\cos 2\theta_W\big)\,[2-(s-m_Z^2-4m^2_{t^{(1)}})\mathrm{C}_0(0,m_Z^2,s,m^2_{t^{(1)}},m^2_{t^{(1)}},m^2_{t^{(1)}})-$$
$$-\tfrac{2m_Z^2}{s-m_Z^2}[\mathrm{B}_0(s,m^2_{t^{(1)}},m^2_{t^{(1)}})-\mathrm{B}_0(m_Z^2,m^2_{t^{(1)}},m^2_{t^{(1)}})]]$$

$$
\begin{aligned}
C =& 2\big(Y_{t_L}\sin^2\theta_W - \tfrac{1}{4}\cos 2\theta_W\big)\,[2 + (s + m_Z^2 + 4m_{t^{(1)}}^2)\mathrm{C}_0(0, m_Z^2, s, m_{t^{(1)}}, m_{t^{(1)}}, m_{t^{(1)}}) \\
&+ 2\tfrac{2s+m_Z^2}{s-m_Z^2}\mathrm{B}_0(s, m_{t^{(1)}}^2, m_{t^{(1)}}^2) - 2\tfrac{s+2m_Z^2}{s-m_Z^2}\mathrm{B}_0(m_Z^2, m_{t^{(1)}}^2, m_{t^{(1)}}^2) - 2\mathrm{B}_0(0, m_{t^{(1)}}^2, m_{t^{(1)}}^2)]\ .
\end{aligned}
$$

D.1.3 $B^{(1)}B^{(1)} \to H\gamma$

This process is dominated by Feynman diagrams of the form

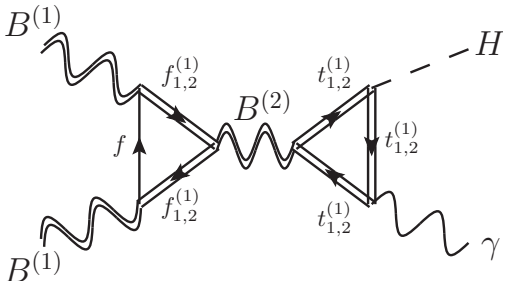

The $A_3^{(2)}$ resonance may contribute as well but in the minimal UED model its contribution is severely suppressed. Top quark contributions dominate the computation of tensor R_V due to their large Yukawa couplings. For the calculation of L_V we apply a simplifying "trick" that follows from the anomaly cancellation in the SM: $\sum_f L^\rho_{f\mu\nu}|_{m_f\to 0} \propto \sum_f (Y_R^3 + Y_L^3) = 0$ implies that $L^\rho_{\mu\nu} = \sum_f L^\rho_{f\mu\nu} \simeq L^\rho_{\mathrm{top}\,\mu\nu} - L^\rho_{\mathrm{top}\,\mu\nu}|_{m_t\to 0}$. The resulting expression for $L^\rho_{\mu\nu}$ is much too lengthy to be displayed here, though. However, the tensor $R^{\gamma H}_{B^{(2)}\alpha\beta}$ is a bit less intricate:

$$
\begin{aligned}
R^{\gamma H}_{B^{(2)}\alpha\beta} \;=\; & -\frac{eg'Q_t(Y_{t_L}+Y_{t_R})}{2\pi^2}\frac{igm_t}{m_W}\frac{m_{t^{(1)}}\sin 2\alpha_t^{(1)}}{(s-m_H^2)^3}\Big(B[(s-m_H^2)\eta_{\alpha\beta} - 2k_{1\beta}k_{2\alpha}] + \\
& + [C_2 k_{2\beta} - C_1 k_{1\beta}]k_{1\alpha}\Big)\ , \qquad \text{(D.6)}
\end{aligned}
$$

where

$$
\begin{aligned}
B =& (s-m_H^2)([2 + (s - m_H^2 + 4m_{t^{(1)}}^2)\mathrm{C}_0(0, m_H^2, s, m_{t^{(1)}}^2, m_{t^{(1)}}^2, m_{t^{(1)}}^2)](s-m_H^2) \\
& -2s[\mathrm{B}_0(s, m_{t^{(1)}}^2, m_{t^{(1)}}^2) - \mathrm{B}_0(m_H^2, m_{t^{(1)}}^2, m_{t^{(1)}}^2)]) \\
C_2 =& -2(s-m_H^2)[(s-m_H^2)[2 + (s + m_H^2 + 4m_{t^{(1)}}^2)\mathrm{C}_0(0, m_H^2, s, m_{t^{(1)}}, m_{t^{(1)}}, m_{t^{(1)}})] \\
& +2(s+2m_H^2)[\mathrm{B}_0(s, m_{t^{(1)}}^2, m_{t^{(1)}}^2) \\
& -\mathrm{B}_0(m_H^2, m_{t^{(1)}}^2, m_{t^{(1)}}^2)] + 2(s-m_H^2)[\mathrm{B}_0(s, m_{t^{(1)}}^2, m_{t^{(1)}}^2) - \mathrm{B}_0(, m_{t^{(1)}}^2, m_{t^{(1)}}^2)] \\
C_1 =& 4[m_H^2(s-m_H^2)[2 + (s+2m_{t^{(1)}}^2)\mathrm{C}_0(0, m_H^2, s, m_{t^{(1)}}, m_{t^{(1)}}, m_{t^{(1)}})] + \\
& +2m_H^2(2s+m_H^2)[\mathrm{B}_0(s, m_{t^{(1)}}^2, m_{t^{(1)}}^2) \\
& -\mathrm{B}_0(m_H^2, m_{t^{(1)}}^2, m_{t^{(1)}}^2)] + (s^2 - m_H^4)[\mathrm{B}_0(s, m_{t^{(1)}}^2, m_{t^{(1)}}^2) - \mathrm{B}_0(, m_{t^{(1)}}^2, m_{t^{(1)}}^2)]\ .
\end{aligned}
$$

In order to obtain $R^{\gamma H}_{A_3^{(2)}\alpha\beta}$, one simply needs to replace $\sin 2\alpha_t^{(1)}(Y_{t_L} + Y_{t_R})$ in eq. (D.6) with $(1/4)\sin 4\alpha_t^{(1)}$.

D.2 $H^{(2k)}$ resonances

Analogous to $H^{(2)}$, higher excitations of the Higgs boson will decay via KK-number violating processes. These decays have however larger widths as more and more kinematically allowed decay states become available. In order to derive these rates we shall

consider the effective vertices and kinetic terms in the fixed points of the orbifold.

$$\delta\mathcal{L}_{\rm eff} = L^{3/2}\left(\frac{\delta(x_5)+\delta(x_5-L)}{2}\right)\frac{y_t}{\sqrt{2}}\frac{1}{64\pi^2}\log\frac{\Lambda^2}{\mu^2}\times$$
$$\times\left[fH\bar{t}_d\frac{1+\gamma_5}{2}t_s + f_aH\bar{t}_d\frac{1-\gamma_5}{2}t_s + \text{h.c.}\right], \tag{D.7}$$

where x_5 is just the fifth space coordinate, $L=\pi R$ is the length separating the orbifold fixed points and $f_{L,R}$ are given by

$$\begin{aligned} f &= 8g_s^2 - \frac{3}{2}g^2 - \frac{1}{6}g'^2\,, \\ f_a &= -2y_t(y_t+y_b) \approx -2y_t^2\,. \end{aligned}$$

The kinetic and mass radiative mixing terms read [4]

$$\delta\mathcal{L} \supset L\left(\frac{\delta(x_5)+\delta(x_5-L)}{2}\right)\frac{1}{64\pi^2}\log\frac{\Lambda^2}{\mu^2}\times$$
$$\times[b_1^{s,d}\bar{t}_{s,d}i\not{\partial}t_{s,d;+,-} + b_2^{s,d}(\bar{t}_{s,d}\overleftarrow{\partial}_5 t_{s,d;+,-} + \tag{D.8}$$
$$+\bar{t}_{s,d;+,-}\partial_5 t_{s,d}) + c_1\frac{1}{2}(\partial_\mu H)^2 + c_2\frac{1}{2}H\partial_5^2 H]\,,$$

where $b_{1,2}^{s,d}$ and $c_{1,2}$ (shown below) were computed in the aforementioned reference. We adopt the notation $t_\pm$ for right and left handed top quark fields.

$$b_1^s = \frac{4}{3}g_s^2 + Y_{t_R}^2 g'^2 + 2y_t^2\,, \tag{D.9}$$
$$b_1^d = \frac{4}{3}g_s^2 + \frac{3}{4}g^2 + Y_{t_L}^2 g'^2 + y_t^2\,, \tag{D.10}$$
$$b_2^s = 5\left(\frac{4}{3}g_s^2 + Y_{t_R}^2 g'^2\right) - 2y_t^2\,, \tag{D.11}$$
$$b_2^d = 5\left(\frac{4}{3}g_s^2 + \frac{3}{4}g^2 + Y_{t_L}^2 g'^2\right) - y_t^2\,, \tag{D.12}$$
$$c_1 = -g'^2 - 2g^2\,, \tag{D.13}$$
$$c_2 = \frac{1}{2}g'^2 + g^2 - 2\lambda_h\,. \tag{D.14}$$

D.2.1 $H^{(4)}$ decay

Let us now illustrate the general method that is used to compute the decay rates of $H^{(2k)}$ in the minimal scenario by explicitly calculating the decay rate of $H^{(4)}$. The main difference $H^{(2)}$ and $H^{(4)}$ is that whereas the former decays with branching ratio ~ 1 into top quark-antiquark pairs, the latter has the following decay modes $H^{(4)} \to \bar{t}_s^{(1)}t_d^{(1)}(\bar{t}_d^{(1)}t_s^{(1)})$, $\bar{t}_{s,d}^{(2)}t^{(0)}$ $(\bar{t}^{(0)}t_{s,d}^{(2)})$ and $\bar{t}t$. The decay $H^{(4)} \to \bar{t}_{s,d}^{(1)}t_{d,s}^{(1)}$ is induced by the effective vertex

$$\delta\mathcal{L} \supset \tfrac{y_t}{64\pi^2}\log\tfrac{\Lambda^2}{\mu^2}H^{(4)}\left[\left(\tfrac{154}{9}g_s^2 + \tfrac{41}{16}g^2 + \tfrac{697}{432}g'^2 - \tfrac{23}{4}y_t^2 + \tfrac{8}{3}\lambda_h\right)\bar{t}_s^{(1)}t_d^{(1)} + \right.$$
$$\left. + \left(\tfrac{69}{9}g_s^2 - \tfrac{29}{16}g^2 - \tfrac{157}{432}g'^2 + \tfrac{3}{4}y_t^2\right)\bar{t}_s^{(1)}\gamma_5 t_d^{(1)} + \text{h.c.}\right],$$

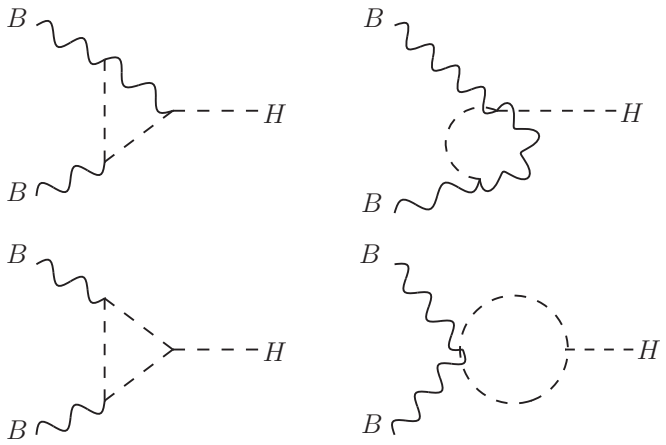

Figure D.1: Relevant Feynman diagrams for eq. (D.15). Contributions from fermion loops vanish provided that H couples to mixed doublet and singlets.

which was obtained by decomposing (D.7) in terms of the KK modes and by including the kinetic and mass mixing terms with $t^{(3)}_{s,d}$, $t^{(5)}_{s,d}$, $H^{(0)}$ and $H^{(2)}$. For $\Lambda = 5/R$ the decay rate of $H^{(4)}$ is $\Gamma_{H^{(4)}} = 3.1\text{GeV}$.

D.2.2 $B^{(1)}B^{(1)}H^{(2k)}$ effective vertices

The same arguments from the previous section apply in this case. We need thus to obtain the relevant vertices in the fixed points of the orbifold. Namely

$$\delta\mathcal{L} \supset L\left(\frac{\delta(x_5)+\delta(x_5-L)}{2}\right)\frac{g'^2 v}{2}\frac{f_S}{64\pi^2}\log\frac{\Lambda^2}{\mu^2}HB_\mu B^\mu \tag{D.15}$$

The kinetic and mass mixing terms read

$$\begin{aligned}\delta\mathcal{L} \supset L\left(\frac{\delta(x_5)+\delta(x_5-L)}{2}\right)\frac{1}{64\pi^2}\log\frac{\Lambda^2}{\mu^2}[&-a_1^B\frac{1}{4}B_{\mu\nu}B^{\mu\nu}\\ &-a_2^B\frac{1}{2}(B_\mu\partial_5^2 B^\mu)+c_1\frac{1}{2}(\partial_\mu H)^2+c_2\frac{1}{2}H\partial_5^2 H]\,.\end{aligned} \tag{D.16}$$

The coefficients in the previous expression were computed in [4], while the coefficient f_S in (D.15) can easily be computed by isolating the divergent contributions of the Feynman diagrams D.1 and adding them. In the Feynman gauge we obtain

$$f_S = \frac{3}{4}g'^2 + \frac{9}{4}g^2 + 12\lambda_h\ . \tag{D.17}$$

To check the correctness of this result, one can obtain the corresponding effective vertices and mixing terms for the A_3 field –this must be done with care, since additional types of Feynman diagrams (ghosts, W loops, etc) need to be considered– and then verify that couplings for vertices such as $A^{(0)}_\mu Z^{(0)\mu}H^{(2k)}$ or $A^{(0)}_\mu A^{(0)\mu}H^{(2k)}$ vanish as required by gauge invariance (A_μ represents the photon field).

Bibliography

[1] T. S. van Albada, J. N. Bahcall, K. Begeman, and R. Sancisi, ApJ**295**, 305 (1985).

[2] M. Markevitch, ESA Spec.Publ. **604**, 723 (2006), astro-ph/0511345.

[3] E. K. Park, Contribution to dmsag report, `http://science.energy.gov/hep/hepap/reports/`, 2007.

[4] H.-C. Cheng, K. T. Matchev, and M. Schmaltz, Phys.Rev. **D66**, 036005 (2002), hep-ph/0204342.

[5] CMS, S. Chatrchyan *et al.*, JHEP **1209**, 094 (2012), 1206.5663.

[6] ATLAS, G. Aad *et al.*, JHEP **1304**, 075 (2013), 1210.4491.

[7] J. Billard, L. Strigari, and E. Figueroa-Feliciano, Phys.Rev. **D89**, 023524 (2014), 1307.5458.

[8] M. Regis and P. Ullio, Phys.Rev. **D78**, 043505 (2008), 0802.0234.

[9] AMS Collaboration, M. Aguilar *et al.*, Phys.Rev.Lett. **110**, 141102 (2013).

[10] L. Bergstrom, T. Bringmann, I. Cholis, D. Hooper, and C. Weniger, Phys.Rev.Lett. **111**, 171101 (2013), 1306.3983.

[11] W. B. Atwood *et al.*, ApJ**697**, 1071 (2009), 0902.1089.

[12] L. Bergstrom, T. Bringmann, M. Eriksson, and M. Gustafsson, JCAP **0504**, 004 (2005), hep-ph/0412001.

[13] T. Bringmann, L. Bergstrom, and J. Edsjo, JHEP **0801**, 049 (2008), 0710.3169.

[14] L. Pieri, J. Lavalle, G. Bertone, and E. Branchini, Phys.Rev.D**83**, 023518 (2011), 0908.0195.

[15] C. Weniger, JCAP **1208**, 007 (2012), 1204.2797.

[16] T. Bringmann, X. Huang, A. Ibarra, S. Vogl, and C. Weniger, JCAP **1207**, 054 (2012), 1203.1312.

[17] C. Weniger, (2013), 1303.1798.

[18] C. G. T. Haslam, C. J. Salter, H. Stoffel, and W. E. Wilson, A&AS**47**, 1 (1982).

[19] J. D. Jackson, *Classical Electrodynamics*, 3 ed. (John Wiley & Sons, Inc., New Jersey, USA, 1991).

[20] M. S. Longair, *High Energy Astrophysics* (Cambridge University Press, 1992).

[21] G. B. Rybicki and A. P. Lightman, *Radiative Processes in Astrophysics* (Wiley, 1979).

[22] L. Bergstrom and P. Ullio, Nucl.Phys. **B504**, 27 (1997), hep-ph/9706232.

[23] O. Adriani *et al.*, JETP Lett. **96**, 621 (2013).

[24] T. Daylan *et al.*, (2014), 1402.6703.

[25] R. Eatough *et al.*, nature **501**, 391 (2013), 1308.3147.

[26] L. Bergstrom, (2012), 1202.1170.

[27] L. van den Aarsen, PhD thesis, University of Hamburg (2013), ISBN 1453-8085.

[28] M. Banados, J. Silk, and S. M. West, Phys.Rev.Lett. **103**, 111102 (2009), 0909.0169.

[29] C. Evoli, I. Cholis, D. Grasso, L. Maccione, and P. Ullio, Phys.Rev. **D85**, 123511 (2012), 1108.0664.

[30] T. Bringmann and P. Salati, Phys.Rev. **D75**, 083006 (2007), astro-ph/0612514.

[31] J. H. Oort, Bull. Astron. Inst. Netherlands **6**, 249 (1932).

[32] F. Zwicky, Helvetica Physica Acta **6**, 110 (1933).

[33] V. C. Rubin, W. K. J. Ford, and N. . Thonnard, ApJ**238**, 471 (1980).

[34] Planck, P. Ade *et al.*, Astron.Astrophys. **571**, A16 (2014), 1303.5076.

[35] Planck, P. Ade *et al.*, (2015), 1502.01589.

[36] A. G. Riess *et al.*, AJ**116**, 1009 (1998), astro-ph/9805201.

[37] Supernova Cosmology Project, S. Perlmutter *et al.*, Astrophys.J. **517**, 565 (1999), astro-ph/9812133.

[38] S. Carroll, *Spacetime and geometry: an introduction to general relativity; International ed* (Pearson Education Limited, Essex, 2013).

[39] P. Gondolo and G. Gelmini, Nuclear Physics B **360**, 145 (1991).

[40] M. E. Peskin and D. V. Schroeder, (1995).

[41] T. Kaluza, Sitzungsber.Preuss.Akad.Wiss.Berlin (Math.Phys.) **1921**, 966 (1921).

[42] O. Klein, Z.Phys. **37**, 895 (1926).

[43] T. Bringmann, PhD thesis, Stockholm University (2005), ISBN 91-7155-117-4.

[44] J. M. Cornell, S. Profumo, and W. Shepherd, Phys.Rev. **D89**, 056005 (2014), 1401.7050.

[45] M. Blennow, H. Melbeus, T. Ohlsson, and H. Zhang, Phys.Lett. **B712**, 419 (2012), 1112.5339.

[46] G. Servant, (2014), 1401.4176.

[47] L. Edelhauser, T. Flacke, and M. Kramer, JHEP **1308**, 091 (2013), 1302.6076.

[48] T. Kakuda, K. Nishiwaki, K.-y. Oda, N. Okuda, and R. Watanabe, (2013), 1304.6362.

[49] G. Cacciapaglia, A. Deandrea, J. Ellis, J. Marrouche, and L. Panizzi, Phys.Rev. **D87**, 075006 (2013), 1302.4750.

[50] G. Servant and T. M. Tait, Nucl.Phys. **B650**, 391 (2003), hep-ph/0206071.

[51] O. S. Bruening *et al.*, *LHC Design Report* (CERN, Geneva, 2004).

[52] ATLAS, G. Aad *et al.*, JINST **3**, S08003 (2008).

[53] CMS, S. Chatrchyan *et al.*, JINST **3**, S08004 (2008).

[54] CMS Collaboration, S. Chatrchyan *et al.*, Phys.Lett. **B716**, 30 (2012), 1207.7235.

[55] ATLAS Collaboration, G. Aad *et al.*, Phys.Lett. **B716**, 1 (2012), 1207.7214.

[56] Q.-H. Cao, C.-R. Chen, C. S. Li, and H. Zhang, JHEP **1108**, 018 (2011), 0912.4511.

[57] A. Birkedal, K. Matchev, and M. Perelstein, Phys.Rev. **D70**, 077701 (2004), hep-ph/0403004.

[58] E. Aprile *et al.*, Physical Review Letters **105**, 131302 (2010), 1005.0380.

[59] XENON1T, `http://http://www.xenon1t.org/`.

[60] D. S. Akerib *et al.*, Nuclear Instruments and Methods in Physics Research A **704**, 111 (2013), 1211.3788.

[61] DAMA, R. Bernabei *et al.*, Eur.Phys.J. **C56**, 333 (2008), 0804.2741.

[62] Z. Ahmed *et al.*, Phys. Rev. Lett. **102**, 011301 (2009).

[63] CRESST Collaboration *et al.*, ArXiv e-prints (2015), 1503.07806.

[64] EDELWEISS Collaboration *et al.*, Physics Letters B **702**, 329 (2011), 1103.4070.

[65] G. Angloher *et al.*, European Physical Journal C **72**, 1971 (2012), 1109.0702.

[66] L. Zhang *et al.*, ApJ**772**, 108 (2013), 1209.0256.

[67] R. Catena and P. Ullio, JCAP **8**, 4 (2010), 0907.0018.

[68] P. Gondolo *et al.*, JCAP **0407**, 008 (2004), astro-ph/0406204.

[69] F. Donato *et al.*, Astrophys.J. **563**, 172 (2001), astro-ph/0103150.

[70] G. Sigl, *Astroparticle Physics: Theory and Phenomenology* (Springer Verlag, 2015).

[71] D. Maurin, F. Donato, R. Taillet, and P. Salati, Astrophys.J. **555**, 585 (2001), astro-ph/0101231.

[72] G. Di Bernardo, C. Evoli, D. Gaggero, D. Grasso, and L. Maccione, Astroparticle Physics **34**, 274 (2010), 0909.4548.

[73] PAMELA Collaboration, O. Adriani *et al.*, Phys.Rev.Lett. **105**, 121101 (2010), 1007.0821.

[74] L. Maccione, Phys.Rev.Lett. **110**, 081101 (2013), 1211.6905.

[75] L. J. Gleeson and W. I. Axford, ApJ**149**, L115 (1967).

[76] L. J. Gleeson and W. I. Axford, ApJ**154**, 1011 (1968).

[77] A. Ibarra, A. S. Lamperstorfer, and J. Silk, Phys.Rev. **D89**, 063539 (2014), 1309.2570.

[78] M. Su, T. R. Slatyer, and D. P. Finkbeiner, ApJ**724**, 1044 (2010), 1005.5480.

[79] S. Snowden *et al.*, Astrophys.J. **485**, 125 (1997).

[80] D. P. Finkbeiner, Astrophys.J. **614**, 186 (2004), astro-ph/0311547.

[81] G. Belanger, F. Boudjema, A. Pukhov, and A. Semenov, Comput.Phys.Commun. **192**, 322 (2015), 1407.6129.

[82] A. Birkedal, K. T. Matchev, M. Perelstein, and A. Spray, eprint (2005), hep-ph/0507194.

[83] L. Bergstrom, T. Bringmann, M. Eriksson, and M. Gustafsson, Phys.Rev.Lett. **94**, 131301 (2005), astro-ph/0410359.

[84] J. Diemand *et al.*, Nature **454**, 735 (2008), 0805.1244.

[85] V. Springel *et al.*, Mon.Not.Roy.Astron.Soc. **391**, 1685 (2008), 0809.0898.

[86] J. F. Navarro, C. S. Frenk, and S. D. White, Astrophys.J. **462**, 563 (1996), astro-ph/9508025.

[87] A. Burkert, IAU Symp. **171**, 175 (1996), astro-ph/9504041.

[88] F.-S. Ling, E. Nezri, E. Athanassoula, and R. Teyssier, JCAP **1002**, 012 (2010), 0909.2028.

[89] G. Bryan and M. Norman, Astrophys.J. **495**, 80 (1998), astro-ph/9710107.

[90] M. Su and D. P. Finkbeiner, (2012), 1206.1616.

[91] C. Weniger, M. Su, D. P. Finkbeiner, T. Bringmann, and N. Mirabal, (2013), 1305.4710.

[92] Fermi-LAT, M. Ackermann *et al.*, Phys.Rev. **D88**, 082002 (2013), 1305.5597.

[93] L. Goodenough and D. Hooper, (2009), 0910.2998.

[94] D. Hooper and L. Goodenough, Phys.Lett. **B697**, 412 (2011), 1010.2752.

[95] T. Bringmann, M. Vollmann, and C. Weniger, Phys.Rev. **D90**, 123001 (2014), 1406.6027.

[96] F. Calore, I. Cholis, and C. Weniger, JCAP **1503**, 038 (2015), 1409.0042.

[97] M. P. van Haarlem *et al.*, A&A**556**, A2 (2013), 1305.3550.

[98] M. A. Garrett *et al.*, ArXiv e-prints (2010), 1008.2871.

[99] J. Bank, `http://www.jodrellbank.net/`.

[100] M. P. I. for Radioastronomy, `http://www.mpifr-bonn.mpg.de/2169/en`.

[101] P. Observatory, `http://www.parkes.atnf.csiro.au/`.

[102] N. Fornengo, R. A. Lineros, M. Regis, and M. Taoso, JCAP **1404**, 008 (2014), 1402.2218.

[103] D. Hooper *et al.*, Phys.Rev.D**86**, 103003 (2012), 1203.3547.

[104] F. R. Elder, R. V. Langmuir, and H. C. Pollock, Phys. Rev. **74**, 52 (1948).

[105] G. Ghisellini, P. W. Guilbert, and R. Svensson, ApJ**334**, L5 (1988).

[106] H. Goldstein, *Classical mechanics*World student series (Addison-Wesley, Reading (Mass.), Menlo Park (Calif.), Amsterdam, 1980).

[107] D. Code, `http://www.dragonproject.org/Home.html`.

[108] I. Moskalenko, Modeling cosmic ray propagation and associated interstellar emissions, in *39th COSPAR Scientific Assembly*, , COSPAR Meeting Vol. 39, p. 1281, 2012, 1105.4921.

[109] S. I. Syrovatskii, Soviet Ast.**3**, 22 (1959).

[110] E. A. Baltz and J. Edsjo, Phys.Rev. **D59**, 023511 (1998), astro-ph/9808243.

[111] V. F. Shvartsman, Soviet Ast.**15**, 377 (1971).

[112] S. L. Shapiro, ApJ**180**, 531 (1973).

[113] F. Melia, ApJ**387**, L25 (1992).

[114] G. Bertone, M. Cirelli, A. Strumia, and M. Taoso, JCAP **0903**, 009 (2009), 0811.3744.

[115] R. D. Davies, D. Walsh, and R. S. Booth, MNRAS**177**, 319 (1976).

[116] M. E. Nord, T. J. W. Lazio, N. E. Kassim, W. M. Goss, and N. Duric, Astrophys.J. **601**, L51 (2004), astro-ph/0312219.

[117] T. N. LaRosa *et al.*, The Astrophysical Journal Letters **626**, L23 (2005).

[118] R. M. Crocker, D. Jones, F. Melia, J. Ott, and R. J. Protheroe, Nature **468**, 65 (2010), 1001.1275.

[119] R. Laha, K. C. Y. Ng, B. Dasgupta, and S. Horiuchi, Phys.Rev. **D87**, 043516 (2013), 1208.5488.

[120] M. Jacob and G. Wick, Annals Phys. **7**, 404 (1959).

[121] K. N. Abazajian, P. Agrawal, Z. Chacko, and C. Kilic, Phys.Rev. **D85**, 123543 (2012), 1111.2835.

[122] Fermi-LAT collaboration, M. Ackermann *et al.*, Phys.Rev.Lett. **107**, 241302 (2011), 1108.3546.

[123] I. Cholis, M. Tavakoli, and P. Ullio, Phys.Rev. **D86**, 083525 (2012), 1207.1468.

[124] J. Edsjo and P. Gondolo, Phys.Rev. **D56**, 1879 (1997), hep-ph/9704361.

[125] `http://fermi.gsfc.nasa.gov/ssc/`.

[126] F. Donato, N. Fornengo, D. Maurin, and P. Salati, Phys.Rev. **D69**, 063501 (2004), astro-ph/0306207.

[127] T. Lacroix, C. Boehm, and J. Silk, Phys.Rev. **D90**, 043508 (2014), 1403.1987.

[128] V. Berezinsky, A. Gurevich, and K. Zybin, Phys.Lett. **B294**, 221 (1992).

[129] P. Ullio, H. Zhao, and M. Kamionkowski, Phys.Rev. **D64**, 043504 (2001), astro-ph/0101481.

[130] D. Merritt, M. Milosavljevic, L. Verde, and R. Jimenez, Phys.Rev.Lett. **88**, 191301 (2002), astro-ph/0201376.

[131] S. Profumo and P. Ullio, ArXiv e-prints (2010), 1001.4086.

[132] R. Aloisio, P. Blasi, and A. V. Olinto, JCAP **0405**, 007 (2004), astro-ph/0402588.

[133] I. Cholis, D. Hooper, and T. Linden, Phys.Rev. **D91**, 083507 (2015), 1408.6224.

[134] N. Arkani-Hamed, D. P. Finkbeiner, T. R. Slatyer, and N. Weiner, Phys.Rev. **D79**, 015014 (2009), 0810.0713.

[135] A. Sommerfeld, Ann. Phys. **403**, 257 (1931).

[136] G. Breit and E. Wigner, Phys. Rev. **49**, 519 (1936).

[137] L. Landau, Dokl.Akad.Nauk Ser.Fiz. **60**, 207 (1948).

[138] C.-N. Yang, Phys.Rev. **77**, 242 (1950).

[139] M. Gustafsson, PhD thesis, Stockholm University (2008), ISBN 978-91-7155-548-9.

[140] G. Belanger, M. Kakizaki, and A. Pukhov, JCAP **1102**, 009 (2011), 1012.2577.

[141] R. Mertig, M. Bohm, and A. Denner, Comput.Phys.Commun. **64**, 345 (1991).

[142] C. Arina, T. Bringmann, J. Silk, and M. Vollmann, Phys.Rev. **D90**, 083506 (2014), 1409.0007.

[143] T. Hahn and M. Perez-Victoria, Comput. Phys. Commun. **118**, 153 (1999), hep-ph/9807565.

[144] M. Kuhlen *et al.*, JCAP **1002**, 030 (2010), 0912.2358.

[145] Y.-Y. Mao, L. E. Strigari, R. H. Wechsler, H.-Y. Wu, and O. Hahn, Astrophys.J. **764**, 35 (2013), 1210.2721.

[146] S. Chaudhury, P. Bhattacharjee, and R. Cowsik, JCAP **1009**, 020 (2010), 1006.5588.

[147] H.-Y. Wu, O. Hahn, R. H. Wechsler, Y.-Y. Mao, and P. S. Behroozi, Astrophys.J. **763**, 70 (2013), 1209.3309.

[148] H.-Y. Wu, O. Hahn, R. H. Wechsler, P. S. Behroozi, and Y.-Y. Mao, Astrophys. J. **767**, 23 (2013), 1210.6358.

[149] A. Klypin, S. Trujillo-Gomez, and J. Primack, Astrophys.J. **740**, 102 (2011), 1002.3660.

[150] F. Ferrer and D. R. Hunter, JCAP **1309**, 005 (2013), 1306.6586.

[151] H.E.S.S. Collaboration, A. Abramowski *et al.*, Phys.Rev.Lett. **110**, 041301 (2013), 1301.1173.

[152] G. Pedaletti, Presentation at the Workshop on the Future of Dark Matter Astro-Particle Physics in Trieste, `http://cdsagenda5.ictp.trieste.it/askArchive.php?base=agenda&categ=a12213&id=a12213s82t70/slides`, 2013.

[153] A. Pinzke, C. Pfrommer, and L. Bergstrom, Phys.Rev. **D84**, 123509 (2011), 1105.3240.

[154] G. Passarino and M. Veltman, Nucl.Phys. **B160**, 151 (1979).

Acknowledgments

The successful completion of this manuscript would not have been possible without the dedicated guidance of my PhD supervisor and co-supervisor Profs. Torsten Bringmann and Günter Sigl. Both of them provided me with very valuable advices that go beyond the topical contents included in this thesis.

Besides all the high level physics discussions that I had with him, I am particularly grateful of Torsten's secret sharing on how to make a successful career in science. I will never forget the several "check lists of a successful theorist" that he would share with me usually over coffee, like some years ago at the Madrid airport or more recently at some café in Altona, Hamburg and in Oslo. I acknowledge the financial support of the *Deutsche Forschungs Gemeinschaft* (DFG) through the Emmy Noether Program BR 3954/1-1 "From Dark Matter Properties to the Fundamental Theory" in the last few months of my PhD program. I would also like to thank the staff members of the theory group at the University of Oslo for their tremendous hospitality.

I am also very grateful for the Günter's reliance towards my skills as a scientist and as a teacher. It was a great pleasure for me to contribute in some of his lectures and to co-supervise the Bachelor's thesis of Robin Reuben, whom I also would like to acknowledge and congratulate hereby. Our discussions enabled me to further enrich the scientific contents of this manuscript. The research summarized in this manuscript was almost fully covered by the *Forschungsstiftung Hamburg* through the exchange program "Astroparticle Physics with Multiple Messengers". I thank Julien Devriendt and Dimitri Semikoz who hosted several of the meetings of this program at Oxford University and Astroparticule et Cosmologie, Paris respectively.

My scientific collaborators Chiara Arina, Masaki Asano, Christoph Weninger and Joe Silk have been a great influence for me as a researcher and for this thesis. I am therefore very happy that I had the opportunity to interact with everyone of them as I currently do with Ma. Vittoria Garzelli, Carmelo Evoli and Natacha Leite. I am also indebted to several colleagues at my home University (Simón Bolívar), in particular to Prof. Jorge Stephany who is the one responsible of most of the foundations necessary for this thesis to be completed. I am also grateful to Paolo Creminelli, Goran Senjanović in Trieste and Klaus Mølmer and Steen Hannestad in Aarhus for their recommendations.

I would like to thank my closest astro-fellows Laura, Andrey, Rafael, Ninetta, Alessandro, Francesca, Arjen and the *condensed matter physics expert* Michelle for being so faithful and giving me your honest opinions every single time that I had to face some new challenge as a PhD student. Your friendship is priceless.

I thank the city of Hamburg and their lovely people. Many of them became good friends and continue to inspire me every day to keep seeking a scientific breakthrough. I acknowledge their help in reading and correcting –albeit not understanding the technical details– essential parts of this manuscript.

Last but not least, I am thankful to my incredible family and my friends from back home, particularly Lilia for her support at the first stages of my PhD. While completing this thesis my family and I were saddened by the physical departure of close relatives, while on the other hand we have been blessed with the birth of several new family members including my lovely niece Sophie. I would like to dedicate this work to her and to her guardian angel Luis Antonio as well as to my deceased godparents Lady, Vladimir and Allis.

Eidesstattliche Versicherung

Hiermit erkläre ich an Eides statt, dass ich die vorliegende Dissertationsschrift selbst verfasst und keine anderen als die angegebenen Quellen und Hilfsmittel benutzt habe.

Hamburg, den 15.7.2015

Martin Vollmann